UNIVERSITY OF OKLAHOMA

GRADUATE COLLEGE

STUDIES OF MOLECULAR ARCHITECTURE WITHIN SOLID POLYMER ELECTROLYTES AND TEICHOIC ACID BIOPOLYMERS FROM SOLID-STATE NUCLEAR MAGNETIC RESONANCE SPECTROSCOPY

A DISSERTATION

SUBMITTED TO THE GRADUATE FACULTY

in partial fulfillment of the requirements for the

Degree of

DOCTOR OF PHILOSOPHY

By
JASON R. WICKHAM
Norman, Oklahoma
2007

UMI Number: 3273884

ProQuest Information and Learning Company
300 North Zeeb Road
P.O. Box 1346
Ann Arbor, MI 48106-1346

STUDIES OF MOLECULAR ARCHITECTURE WITHIN SOLID POLYMER ELECTROLYTES AND TEICHOIC ACID BIOPOLYMERS FROM SOLID-STATE NUCLEAR MAGNETIC RESONANCE SPECTROSCOPY

A DISSERTATION APPROVED FOR THE
DEPARTMENT OF CHEMISTRY AND BIOCHEMISTRY

BY

Charles V. Rice

George B. Richter-Addo

Robert P. Houser

Roger Frech

Peter S. McFetridge

Acknowledgements

When I set out on my collegiate journey I never imagined that I would have the passion for learning and love of science that I have today. The path that I have taken to get to this point has not always been the straightest, but thankfully there have been many people around me whom guided my travels.

The earliest navigators of my voyages were my parents (Robert and Mary Wickham). Whether it was household chores, schoolwork, or work they taught me to think about how to overcome the challenges before me rather than rushing in blindly. These lessons I still carry with me today and have become very useful tools in my life as a researcher. Besides their teachings they have shown me an unwavering love that supports me though any situation. For all of their contributions to my life past, present, and future I am eternally grateful and am indebted to them always.

I am eternally grateful to my wife Lisa for her love and support, as she was the pivotal turning point in my life that inspired me to do something meaningful with my life. Not only has she been my inspiration and pillar of support, but she has also endured all of the late hours and stress with never-ending understanding, which has made it possible for us to start our family with the addition of our son Dylan two years ago. She is truly one of a kind. If it were not for her I would not be at this point in my career; thank you and I love you.

I am also indebted to my little sister, whom initially was more disciplined than myself and had a much clear view of her goals than I did.

She began her collegiate endeavors shortly after I met Lisa and has also played a large role in keeping me on the right path.

My research career started under the guidance of Dr. William Kelly. Somehow he was able to see something in me that I did not know existed, which ignited my passion for science. For this I am truly grateful.

When I began my life here at OU I was fortunate enough to fall under the expert guidance of Dr. Charles V. Rice. Dr. Rice has done more for me than I have the words for. He constantly believed and mentored me, but at the same time he allowed me the freedom I needed to grow. I would not be the scientist I am today without him and in many ways he has taken on the role of a father. I am deeply indebt and grateful for everything he has done.

I am very grateful to Dr. Frech for his tremendous contributions in my studies of solid polymer electrolytes. Our numerous conversations have provided a wealth of knowledge that has assisted me in many ways with my research.

I am also grateful to my advisory committee (Drs. Rice, Frech, Richter-Addo, Houser, and McFetridge). They have always had my best interest in mind they have kept me focused and guided me through my years here at OU.

I am grateful for the fiends and coworkers that I have had the pleasure of knowing and working with over the years. In particular I have work very closely with Dr. Shawna York and Rachael Mason. They were both extremely helpful and working with them has been a pleasure.

I am grateful to the funding agencies that have funded our lab over the years (NSF, OCAST, and PRF) and to the Graduate Assistance in Areas of National Need (GAANN) fellowship that I am currently on for the funding of my research and this dissertation.

Table of Contents

List of Figures

List of Tables

Abbreviations

γ	magnetogyric ratio
σ^{iso}	isotropy chemical shift value
Δ_{CSA}	chemical shift anisotropy tensor
ΔS	difference spectrum
η	asymmetrical parameter
AFGPs	antifreeze glycoproteins
AFPs	antifreeze proteins
CPMAS	cross polarization magic angle spinning
CSA	chemical shift anisotropy
CW	continuous wave
D	dipolar-coupling constant
DSC	differential scanning calorimetry
EC	ethylene carbonate
FID	free-induction decay
GlcNAc	N-acetylglucosamine
LiTf	lithium triflate ($LiSO_3CF_3$)
LPEI-G2	linear poly(N-(2-(2-methoxyethoxyethyl) ethylenimine)
LPU-PEO	linear polyurethane - polyoxyethylene
LTA	lipoteichoic acid
LTA/Mg^{2+}	lipoteichoic acid bound to magnesium
LTA – PGN	lipoteichoic acid adhered to peptidoglycan
MAS	magic angle spinning
MEEP	methoxy ethoxy ethoxy polyphosphazene
MurNAc	N-acetylmuramic acid
NiMH	nickel metal hydride
NMR	Nuclear Magnetic Resonance
PC	propylene carbonate
PEG	poly ethylene glycol
PEH-PEO	polyepichlorohydrin - polyoxyethylene
PEO	poly(ethylene oxide)
PEO-PEI	polyoxyethylene - polyethylenimine
PGN	peptidoglycan
PMMA-PEO	poly(methylmethacrylate) funtionalized with PEO
PPO	polypropylene oxide
REDOR	rotational echo double resonance
RF	radio frequency
S_0	full echo spectrum
SPE	solid polymer electrolyte
S_r	dephased echo spectrum
SSNMR	solid-state nuclear magnetic resonance
T_1	spin-lattice (longitudinal) relaxation
T_2	spin-spin (transverse) relaxation

$T_{1\rho}$	rotating frame spin-lattice relaxation
T_g	glass transition
TEG	tetra ethylene glycol
TEGDME	tetra ethylene glycol dimethyl ether
TLR	toll-like receptor
T_m	melting point
UDP-GlcNAc	uridine 5’-diphospho-N-acetylglucosamine
VT	variable temperature
WTA	wall teichoic acid

Abstract:

Part I

Understanding and assigning the ^{13}C NMR signals are vital to interpreting the NMR data collected for each phase. Previously for pure PEO, the narrow component has been assigned to the amorphous region and the broad component to the crystalline region. Using a crystalline 3:1 PEO:LiTf sample, we assign the narrow component to the crystalline PEO:LiTf region, which is reversed from the previous pure PEO assignment. Thus, we reexamine the NMR assignments for pure PEO using samples of pure powdered PEO, thermally treated pure powdered PEO, and a thin film PEO cast from an acetonitrile solution. We observed the growth of the narrow peak under conditions that favor crystallization; therefore, we reassigned the narrow peak to the crystalline region and the broad peak to the amorphous region.

There is little structural information for dilute salt systems, thus we have characterize the crystalline microdomains of a 20:1 PEO:LiTf sample using the REDOR SSNMR experiment. Our data clearly demonstrates that the lithium crystalline microdomains are nearly identical to that of the crystalline 3:1 sample.

Part II

Teichoic acids important to bacteria since they participate in surface adhesion, metal ion coordination, and survival at subzero temperatures. However, there is very little molecular level information available for the initial

adhesion of bacteria to solid surfaces. ^{31}P CP-MAS spectra and $T_{1\rho}$ data demonstrate that the structure of LTA changes when adhered to cellulose, PGN, or TiO_2 (the structure of LTA on TiO_2 is heterogeneous). However, when LTA is simultaneously adhered to PGN and TiO_2 the observed structure is dependent on the amount of retained water. Our proposed structure for LTA on TiO_2 has the alanine adhered to the surface with the glucosamine groups rotated toward the surface. However, simultaneous adhesion uses the glucosamine groups to adhere to PGN allowing water absorption between the LTA backbone and the TiO_2 surface. Our NMR studies also demonstrate that WTA properties are very similar to LTA.

The proposed Mg^{2+} binding structure to teichoic acids are monodentate fashion to either one phosphate or bridging between two phosphates. However, we show that Mg^{2+} binds in a bidentate fashion through compassion of experimental collected ^{31}P CP-MAS spectra to a simulated ^{31}P CPMAS spectra form an energy-minimized model compound.

The unsuccessful collection of a ^{31}P CP-MAS spectrum in frozen D_2O suggests the presence of liquid water around LTA. ^{2}H SSNMR were used to study the phase of the water environments for LTA dissolved in D_2O at -25 and –40 $^{\circ}C$. This resulted in the presence of a narrow (liquid) and broad (solid) signal at both temperatures, demonstrating that LTA is an anti-freeze agent.

Part I

Solid-State NMR Investigations of Solid Polymer Electrolytes

Chapter 1:

Rechargeable Lithium Ion Batteries and Solid Polymer Electrolytes

Battery Background:

Rechargeable batteries are referred to as secondary batteries. Secondary batteries are desirable due to the fact that they are a renewable source of energy. The three main types of secondary batteries are lead-acid, nickel metal hydride (NiMH), and lithium ion. Of these, lithium has the highest energy density followed by nickel and then lead-acid. Energy density is essentially the amount of energy obtained from a certain volume or amount of the material, and is usually referred to as either volumetric (Wh/L) or gravimetric (Wh/Kg). The volumetric energy densities of these three materials are ~ 70 Wh/L for lead-acid, ~ 100-245 Wh/L for nickel, and ~ 400 Wh/L for lithium, thus lithium batteries are more desirable. There are two reasons that lithium has the highest energy density; the first being that it is the most electropositive metal (reduction potential of –3.04 V), and the second because lithium is the lightest metal. Due to lithium's high energy density, lithium batteries can be made small but still maintain good operating voltages (e.g. coin cell batteries).(*1, 2*) However, energy density is not the sole reason that lithium secondary batteries are desirable. Lithium ion batteries are also desirable because they are not as toxic as lead-acid or nickel cadmium

batteries, and they have longer service life (number of charging cycles before failure) than nickel metal hydride batteries.(*3*)

Secondary batteries are made up of three basic parts: the anode, the cathode, and the electrolyte with separator. The separator, which separates the anode from the cathode (preventing direct shorting), is composed of an inert porous polymer separator, usually poly(propylene), impregnated with low molecular weight organic liquids containing a dissolved salt (electrolyte). However, these organic liquids present a potential fire, environmental, and health hazards, and may react with the electrode materials. Also, the mechanical properties of liquids pose serious problems in terms of limited battery designs and hazardous leakage. Because of these issues, rechargeable liquid batteries suffer in terms of application and durability problems. However, solid polymer electrolytes are a possible answer to these problems.(*1-3*)

Secondary batteries are considered to be more environmentally friendly because they have longer service lives than primary batteries, which reduces the amount of battery waste produced.(*3*) In secondary batteries with liquid electrolytes, battery failure is normally caused by dendrite formation, which creates a direct short between the electrodes. Dendrite formation is facilitated by the presence of the separator, which causes uneven plating of lithium onto the electrodes. Solid polymer electrolytes reduce dendrite formation by evenly plating lithium onto the electrodes, thus increasing the service life of the battery. Long service lives of secondary batteries are vital

for the mobile lifestyle of the modern world. Thus, prolonging their service life is important to the performance of these mobile devices.(*1, 2*)

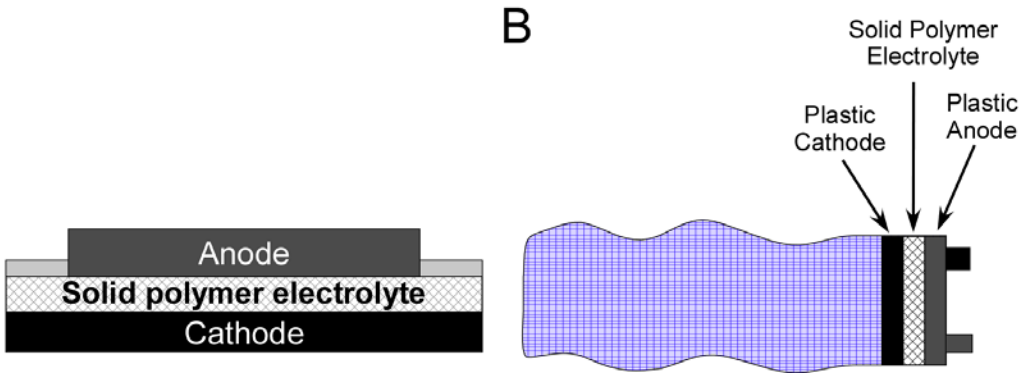

Figure 1.1. Demonstrates the versatility of solid polymer electrolytes as they can be uses in current battery designs (A) or can be used in designs unsuitable for liquid electrolytes such as ribbon batteries (B).

As previously mentioned, liquid electrolytes have limited battery designs and uses due to durability problems (leakage) and the need for a separator. However, solid polymer electrolytes are very pliable and act like a separator themselves, creating an almost limitless number of possible designs and uses. This becomes important in applications that are space limited. Figure 1.1 shows two different possible designs A) the traditional coin cell (liquid and solid polymer electrolyte compatible), and B) the ribbon design (only solid polymer electrolyte compatible). Although solid polymer electrolytes are superior, in some ways they have either low room temperature ionic conductivities or poor mechanical properties, which have hampered the ability for these materials to replace liquid electrolytes. Thus, for the past 30 years there has been a tremendous amount research done on solid polymer electrolytes. However, there has yet to be a suitable solid polymer electrolyte developed.(*1, 4-9*) Critical to these efforts is the need to

identify the chemical interactions that hinder or facilitate the desired properties.

Solid Polymer Electrolyte Background:

Poly(ethylene oxide) (PEO) is the most widely studied solid polymer electrolyte material. PEO is a linear polyether chain that is able to form complexes with group 1 and 2 salts as well some transition metal salts. PEO [$(CH_2CH_2O)_n$] is capable of coordinating with metal salts because of the presence of a donor oxygen atom in the polymer backbone. PEO is a heterogeneous material composed of a crystalline and an amorphous region with a melting point (T_m) of 65 $^{\circ}$C and a glass transition (T_g) of –60 $^{\circ}$C.(*10*) Wright first investigated the ionic conductivity of PEO in 1973,(*9, 11*) but Armand was the first to realize its potential use as a solid polymer electrolyte material.(*12*) Many laboratories have investigated solid-polymer electrolytes based on PEO, due to its low glass transition temperature (T_g) and the ability to dissolve metal salts.(*13-16*) Nonetheless, there is still a great deal of chemical understanding to be gained with the expectation of improving PEO's ionic conductivity and mechanical properties.

Lithium provides high energy density, yet the room temperature conductivities of PEO:Li salt systems are too low to replace current liquid or hybrid batteries. There are two properties that must be simultaneously improved in order to develop a solid polymer electrolyte capable of replacing

current electrolytes: 1) improvement of lithium transport between the electrodes (better ionic conductivity), and 2) maintaining good mechanical properties. It has been established that the bulk ionic conductivity for dilute PEO:salt complexes occur in the amorphous region.(*16*) The theory is that ionic conductivity is facilitated by segmental motion. Lithium cations coordinate to the polymer electrolyte through weak chemical interactions that are periodically broken and reformed. The driving force for transport through the amorphous region is the segmental motion that is present at room temperature, which is well above the T_g of PEO. It has been established through X-ray crystallography that lithium dissolved in the PEO matrix prefers a 5-coordinate environment.(*17, 18*) Thus, the mechanism for ion transport is thought to begin with a lithium cation that is in a 5-coordinate conformation eventually transformed into a 4-coordinate conformation due to the segmental motion of the polymer electrolyte. This new conformation is less stable than the 5-coordinate conformation, which causes the lithium cation to move to a neighboring binding site facilitating lithium transport (Figure 1.2).(*18*) The cation migration occurs in directional unison with the applied electrical potential.

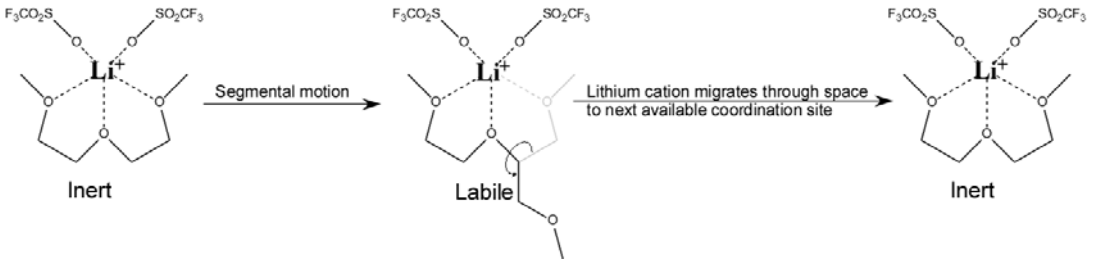

Figure 1.2. Shows a proposed mechanism for ionic conductivity in PEO:LiTf materials. For this mechanism the lithium cation begins in a 5-coordinate environment, which is inert. However, the amorphous region is in continuous flux referred to as segmental motion. Segmental motion forces the PEO backbone to change conformation, resulting in the lithium environment changing to 4-coordinate. The lithium cation is labile in this coordination environment, which facilitates the through migration of lithium cations to the next available 5-coordenate site.

It is important to note that although the ionic conductivity of these materials is related to the number of charge carriers, it does not necessarily mean that increasing the number of charge carriers will increase the ionic conductivity. This is true up to a point, but then the ionic conductivity decreases, which is attributed to the increase of the crystalline region (traps the lithium ions and prevents diffusion), and a decrease of the amorphous region. For example, the maximum coordination number for lithium triflate with PEO is 3:1 (O:Li). Although this material has the highest concentration of charge carriers, it also has the lowest ionic conductivity. It has been found that each system has to be optimized so that it contains the maximum number of charge carriers, while maintaining sufficient segmental motion necessary for ion transport (Figure 1.3).(*19*)

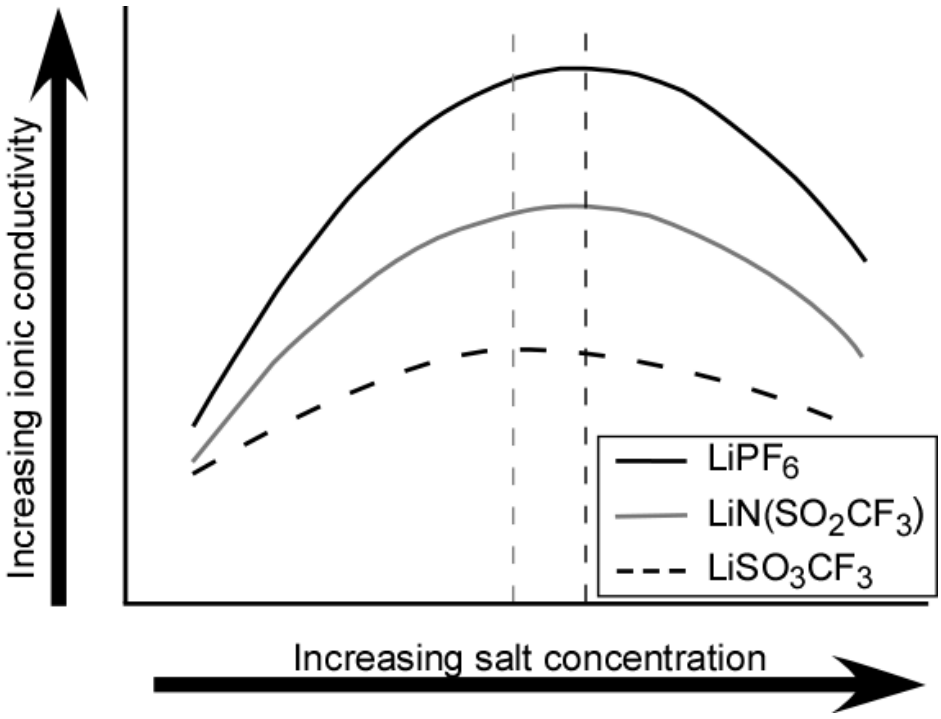

Figure 1.3. Graph shows the dependence of ionic conductivity on Li salt concentration at ambient temperature. It is also demonstrates that ionic conductivity changes are unique for different Li salts. $LiPF_6$ and $LiN(SO_2CF_3)$ experience optimal ionic conductivity at higher salt concentrations (black horizontal dash line), while $LiSO_3CF_3$ experience optimal ionic conductivity at lower salt concentrations (gray horizontal dash line). This graph is modified from reference 19.

For PEO:Li salt systems, impedance measurements can be used to evaluate ion transport(*20*) while DSC measurements are used to measure the T_g of the system. By combining impendence measurements with DSC data, the relationship between polymer backbone mobility and ionic conductivity becomes apparent. The trend generally seen is that materials with lower T_g values have higher ionic conductivities.

Dilute PEO electrolytes are heterogeneous at room temperature, consisting of a pure PEO phase, a crystalline PEO-salt phase, and an amorphous phase containing some dissolved salt.(*7, 16, 21-23*) For

unmodified PEO the ionic conductivity is generally 10^{-6} – 10^{-8} S/cm at room temperature, which is still orders of magnitude below the ionic conductivity (10^{-3} – 10^{-4} S/cm) needed for battery use.(*10*) As previously mentioned, it has been observed in numerous PEO:salt systems that ionic conductivity occurs mainly in the amorphous phase.(*16*) Thus, heating the polymer near 100 ºC significantly increases conductivity (10^{-3} – 10^{-4} S/cm), which is attributed to a melting of the crystalline phase making a completely amorphous material.(*15*) The affect temperature has on ionic conductivity is shown in Figure 1.4. This Figure shows the ionic conductivity plots for the 8:1 and 4:1 PEO:LiTf electrolytes. Both of these electrolytes exhibit an increase in ionic conductivity as the materials are heated to 100 ºC, but there is a dramatic jump in ionic conductivity for the 8:1 PEO:LiTf electrolyte attributed to the melting of the pure PEO crystalline region. This is not observed to the 4:1 PEO:LiTf due to the higher amount of the crystalline PEO:LiTf complex present, thus there is either very little pure PEO crystalline region present and limited coordination sites.

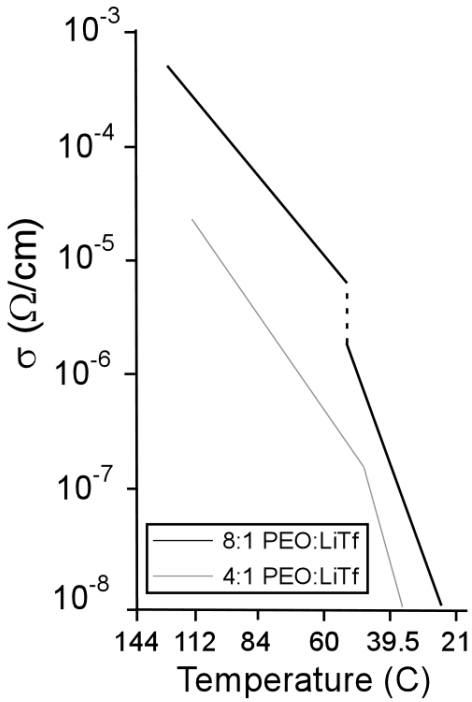

Figure 1.4. Shows conductivity for the 8:1 PEO:LiTf (black line) and the 4:1 PEO:LiTf (gray line) electrolytes as the temperature is varied. This graph is modified from reference 10.

It has been well established that all crystalline regions are detrimental to the ionic conductivity of solid polymer electrolytes. Thus, there have been various efforts made to reduce the amount of the crystalline phase at room temperature by using plasticizers and copolymers, thereby increasing conductivity.(*10, 24-45*)

Several different plasticizers have been used that increased ionic conductivity by decreasing the crystalline region. Generally speaking, these can be put into three classes: organic, inorganic, and mixed organic/inorganic plasticizers. Organic plasticizers such as, ethylene carbonate (EC), propylene carbonate (PC), poly ethylene glycol (PEG), tetra ethylene glycol (TEG), and tetra ethylene glycol dimethyl ether (TEGDME) have been used.

These plasticizers effectively decrease the crystalline region and increased the ionic conductivity to 10^{-4} – 10^{-5} S/cm at room temperature.(*10, 25, 28-30, 33, 39, 42*) However, these all suffer from evaporation of the plasticizer, poor mechanical properties, and in some cases, were reactive towards the lithium cathode. Inorganic plasticizers such as titanium dioxide, silicates, and aluminum silicates have been used as plasticizers.(*10, 25, 28, 33, 39, 42*) These have also been able to raise the ionic conductivity to 10^{-5} S/cm, but are prone to phase separating of the inorganic nanoparticles from the PEO, resulting in materials with poor mechanical properties.(*10, 25, 28, 33, 39, 42*) The goal behind hybrid organic/inorganic plasticizers is to express the benefits seen with organic and inorganic plasticizers, but prevent the phase separations that occur with other plasticizers. These plasticizers are often nanoparticles of silica with short polyethylene glycol (PEG) units covalently attached. This PEG unit makes the silica nanoparticles soluble in PEO and prevents the phase separation problem that is seen with inorganic plasticizers. In addition, having the organic molecule anchored to the silica prevents the evaporation seen with other organic plasticizers. Thus, these organic/inorganic plasticizers have been able to increase ionic conductivity to 10^{-5} S/cm without experiencing the phase separation problems.(*28, 29, 42*)

Various PEO copolymers have experienced an increase in ionic conductivity to 10^{-4} – 10^{-5} S/cm at room temperature. These copolymers can be placed in two classes: polymers with PEO type functional side chains or

block copolymers. Both of these classes of copolymers strive to increase ionic conductivity through increasing segmental motion.

One such PEO copolymer is methoxy ethoxy ethoxy polyphosphazene (MEEP). This copolymer consists of a polyphosphazene backbone with a short PEO chain hanging off (Figure 1.5A). This copolymer is completely amorphous with a T_g of –83 ºC and an optimal ionic conductivity of 10^{-5} S/cm at ambient temperature with lithium triflate (LiTf).(*10, 24, 26, 40*) Another copolymer is poly(methylmethacrylate) funtionalized with PEO (PMMA-PEO). This copolymer consists of a poly(methylmethacrylate) backbone with a short PEO chain hanging off (Figure 1.5B), and has an optimal ionic conductivity of 10^{-5} S/cm at ambient temperature with lithium triflate (LiTf).(*10, 27, 34, 35, 38, 45*) Poly(itaconate) has also been functionalized with PEO (Figure 1.5C) and has an optimal ionic conductivity of 10^{-6} S/cm at ambient temperature with lithium perchlorate ($LiClO_4$).(*31*) Recently, Snow et. al. developed a system using linear poly(ethyleneimine) as the backbone with PEO side chains (Figure 1.5D). This polymer system is named linear poly(N-(2-(2-methoxyethoxyethyl) ethylenimine) (LPEI-G2) and demonstrates an optimal ionic conductivity of 10^{-6} S/cm at ambient temperature with lithium triflate (LiTf).(*41*) Although these systems have good ionic conductivity they have poor mechanical properties, which has prevented their use as solid polymer electrolytes.(*10*) Thus, the mechanical properties for MEEP and PMMA-PEO systems have been improved by cross-linking, but this has resulted in an order of magnitude drop in ionic conductivity.(*10*)

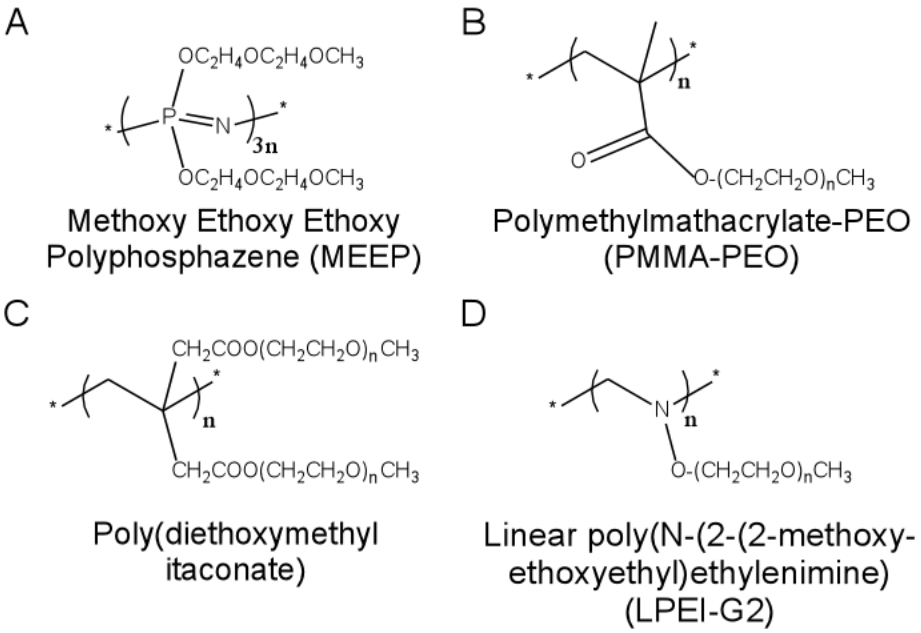

Figure 1.5. Chemical structures of various copolymers with PEO functional side groups.

Another way to improve ionic conductivity is by disrupting the crystalline domains with block copolymers. Ionic conductivity raises have been seen for polyoxyethylene - polyethylenimine (PEO-PEI) (Figure 1.6A), polyurethane - polyoxyethylene (LPU-PEO) (Figure 1.6B), polyoxyethylene - polysiloxane (Figure 1.6C), and polyepichlorohydrin - polyoxyethylene (PEH-PEO) (Figure 1.6D).(*10, 32, 36, 37, 43, 44*) Of these copolymers the highest ionic conductivity (10^{-4} S/cm) was achieved with the PEO-PEI copolymer. The rest of these copolymers achieved ionic conductivity between 10^{-5} – 10^{-6} S/cm.

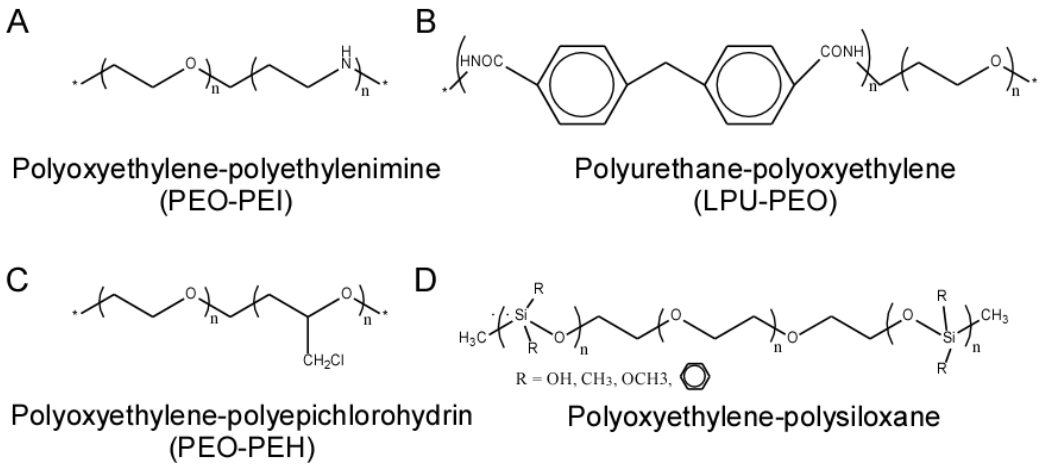

Figure 1.6. Chemical structures of various PEO block copolymers.

Several research groups have cross-linked PEO containing block copolymers in order to improve the mechanical properties. One such method has involved using polysiloxanes. In this case researchers used a diamine polypropylene oxide (PPO) with either a polysiloxane containing an epoxide or a polysiloxane/PEO copolymer containing an epoxide.(*36, 37*) Others have used polyurethane/PEO copolymers that have isocyanate and hydroxyl groups. These copolymers are cross-linked using the isocyanate and hydroxyl groups.(*32*) Cross-linked polymer electrolytes have also been made using PEO/PPO copolymers.(*32, 44*) Although all of these polymer electrolytes have improved mechanical properties, but their ionic conductivity lower by an order of magnitude (10^{-6} – 10^{-7} S/cm at room temperature).(*32, 36, 37, 44*)

It is evident that a solid polymer electrolyte must possess high ionic conductivity (10^{-3} – 10^{-4} S/cm at ambient temperature) and good mechanical properties in order to be successful. Currently there is no solid polymer electrolyte that possesses both properties, and there is very little structure information available to aid in the pursuit of a new candidate. This greatly hampers the ability for engineers to understand and improve the system. X-ray crystallography cannot be employed to study dilute polymer electrolytes because the reduction in crystallinity destroys the long-range structural order necessary for diffraction.(*18*)

Solid-state NMR is ideally suited to provide essential data for the heterogeneous domains within dilute polymer electrolytes. Previous solid-state NMR studies of PEO or PEO-based polymer electrolytes have examined the connection between ion diffusion and polymer segmental motion. Spin-lattice relaxation and pulse field gradient measurements of ^{7}Li and ^{19}F yield ion diffusion rates, which are used to gauge the success of polymer electrolyte modifications.(*24, 25, 32, 39, 42, 46-49*) The ^{7}Li NMR spectrum can also be used to identify the number of lithium binding sites.(*37, 50*) Carbon-13 MAS NMR experiments have been used to detect the amorphous and crystalline regions of PEO electrolytes,(*36, 51-53*) study polymer dynamics with T_1 experiments,(*42, 51, 54, 55*) detect backbone inorganic filler interactions,(*56*) and measure the distance between the backbone CH_2's and the triflate CF_3's.(*52*) Static ^{13}C solid-state NMR experiments have been used to study polymer-cation interactions.(*52, 57*)

Nonetheless, these experiments cannot provide the detailed structural information available from Rotational Echo DOuble Resonance (REDOR) data. This has been demonstrated by the recent REDOR study of a crystalline 6:1 PEO:$LiPF_6$ sample,(*58*) which agreed with the previously published X-ray structure.

A pivotal point in the understanding of lithium containing PEO solid polymer electrolytes happened in 1993 when the Bruce group solved the crystal structure for PEO_3:LiTf.(*17*) Knowing this crystal structure greatly advanced the understanding of ionic conductivity, DSC, and phase diagrams of these completely crystalline PEO electrolytes. However, there is still little to no structural information available for the more dilute PEO:salt complexes, which leaves a void in the understanding of these systems and greatly hampers the advancement of this field. Recently, it has demonstrated that the crystalline PEO_6:XF_6 (X = P, As, Sb) have significant ionic conductivities.(*7, 59, 60*) Through the aid of X-ray crystal structures, the mechanism for ion transport is thought to be ion hopping.(*7, 59-62*) The ionic conductivity of these polymer electrolytes has been increased through anion substitution and divalent doping, which causes small defects in the PEO helix.(*61, 63, 64*) These improvements in concentrated electrolytes are directly related to the understanding gained from the crystal structures. Similar improvements can be realized from understanding the structures of dilute PEO:salt electrolytes.

Reference:

1. D. R. Sadoway, A. M. Mayes, *MRS Bulletin*, 590 (2002).
2. J. M. Tarascon, M. Armand, *Nature (London)* **414**, 359 (2001).
3. W. Lu, D. D. L. Chung, *Energeia* **14**, 1 (2003).
4. Y. G. Andreev, P. G. Bruce, *J. Phys.: Condens. Matter* **13**, 8245 (2001).
5. M. Armand, *Solid State Ionics* **9 & 10**, 745 (1983).
6. F. Croce, G. B. Appetecchi, L. Persi, B. Scrosati, *Nature (London)* **394**, 456 (1998).
7. Z. Gadjourova, Y. G. Andreev, D. P. Tunstall, P. G. Bruce, *Nature (London)* **412**, 520 (2001).
8. M. Gauthier, A. Bélanger, B. Kapfer, G. Vassort, M. Armand, *Solid Polymer Electrolyte Lithium Batteries. In Polymer Electrolyte Reviews*. C. A. Vincent, Ed. (Ed. Elsevier, London, 1989), pp. 285-332.
9. P. V. Wright, *Br. Polym. J.* **7**, 319 (1975).
10. V. Chandrasekhar, *Adv. Polym. Sci.* **135**, 139 (1998).
11. D. E. Fenton, J. M. Parker, P. V. Wright, *Polymer* **14**, 589 (1973).
12. M. B. Armand, M. J. Duclot, P. Rigaud, *Solid State Ionics* **3-4**, 429 (1981).
13. B. L. Papke, M. A. Ratner, D. F. Shriver, *J. Electrochem. Soc.* **129**, 1434 (1982).
14. R. Frech, S. Chintapalli, P. G. Bruce, C. A. Vincent, *Chem. Commun.*, 157 (1997).
15. R. Frech, S. Chintapalli, P. G. Bruce, C. A. Vincent, *Macromolecules* **32**, 808 (1999).
16. C. Berthier *et al.*, *Solid State Ionics* **11**, 91 (1983).
17. P. Lightfoot, M. A. Mehta, P. G. Bruce, *Science* **262**, 883 (1993).
18. C. P. Rhodes, R. Frech, *Macromolecules* **34**, 2660 (2001).

19. D. Linden, T. B. Reddy, *Handbook of Batteries* (McGraw-Hill, New York ed. 3rd 2002), pp. 35.26.

20. P. G. C. Bruce, Stephen A.; Lightfoot, Philip; Mehta, Mary Anne, *Solid State Ionics*, 191 (1995).

21. D. Fauteux, P. McCabe, *Polym. Adv. Techn.* **6**, 83 (1995).

22. S. Lascaud *et al.*, *Macromolecules* **27**, 7469 (1994).

23. A. Vallee, S. Besner, J. Prud'homme, *Electrochim. Acta* **37**, 1579 (1992).

24. K. J. Adamic *et al.*, *Chem. Mater.* **3**, 534 (1991).

25. J. Adebahr *et al.*, *Phys. Chem. Chem. Phys.* **5**, 720 (2003).

26. H. R. Allcock, S. E. Kuharcil, C. S. Reed, M. E. Napierala, *Macromolecules* **29**, 3384 (1996).

27. D. J. Bannister, G. R. Davies, I. M. Ward, J. E. McIntyre, *Polymer* **25**, 1600 (1984).

28. L. M. Bronstein *et al.*, *J. Mater. Chem.* **14**, 1812 (2004).

29. L. M. Bronstein, R. L. Karlinsey, B. Stein, J. W. Zwanziger, *Solid State Ionics* **176**, 559 (2005).

30. S. Chintapalli, R. Frech, *Macromolecules* **29**, 3499 (1996).

31. J. Cowie, A. Martin, *Polymer Commun.* **25**, 298 (1985).

32. L. Hong, L. Shi, X. Tang, *Macromolecules* **36**, 4989 (2003).

33. P. Johansson, M. A. Ratner, D. F. Shriver, *J. Phys. Chem. B* **105**, 9016 (2001).

34. N. Kobayashi, M. Uchiyama, K. Shigehara, E. Tsuchida, *J. Phys. Chem.* **89**, 987 (1985).

35. N. Kobayashi, M. Uchiyama, E. Tsuchida, *Solid State Ionics* **17**, 307 (1985).

36. P. L. Kuo, S. S. Hou, C. Y. Lin, C. C. Chen, T. C. Wen, *J. Polym. Sci., Part A: Polym. Chem.*, 2051 (2004).

37. W.-J. Liang, C.-L. Kuo, C.-L. Lin, P.-L. Kuo, *J. Polym. Sci., Part A: Polym. Chem.,* **40**, 1226 (2002).

38. M. Morita *et al.*, *J. Electrochem. Soc.* **137**, 3401 (1990).

39. P. Mustarelli *et al.*, *Phys. Rev. B* **60**, 7228 (1999).

40. G. Nazri, D. M. MacArthur, J. F. Ogara, *Chem. Mater.* **1**, 370 (1989).

41. A. G. Snow, R. A. Sanders, R. Frech, D. T. Glatzhofer, *Electrochim. Acta* **48**, 2065 (2003).

42. P. H. d. Souza *et al.*, *Chem. Mater.* **13**, 3685 (2001).

43. R. Tanaka *et al.*, *Electrochim. Acta* **46**, 1709 (2001).

44. Z. Wena *et al.*, *Solid State Ionics* **175**, 739 (2004).

45. D. W. Xia, D. Soltz, J. Smid, *Solid State Ionics* **14**, 221 (1984).

46. D. Golodnitshy *et al.*, *J. Phys. Chem. A* **105**, 10098 (2001).

47. C. Roux, W. Gorecki, J.-Y. Sanchez, M. Jeannine, E. Belorizky, *J. Phys. Condens. Matter* **7**, 6823 (1995).

48. C. Roux, W. Gorecki, J.-Y. Sanchez, M. Jeannine, E. Belorizky, *J. Phys. Condens. Matter* **8**, 7005 (1996).

49. S. Wong, S. Vasudevan, R. A. Vaia, E. P. Giannelis, D. B. Zax, *J. Am. Chem. Soc.* **117**, 7568 (1995).

50. W.-J. Liang, P.-L. Kuo, *Macromolecules* **37**, 840 (2004).

51. A. F. Bartolotta, Claudia; Geppi, Marco; Minniti, Domenico; Visalli, Giuseppe, *Solid State Nucl. Magn. Reson.*, 231 (1997).

52. J. Spevacek, J. Brus, *Macromol. Symp.*, 111 (2003).

53. J. Spevacek, J. Brus, J. Dybal, *Solid State Ionics* **176**, 163 (2005).

54. N. C. B. Mello, Tito J.; Panepucci, Horacio; Dahmouche, Karim; Judeinstein, Patrick; Aegerter, Michel A, *Macromolecules*, 1280 (2000).

55. R. S. Spindler, D. F, *J. Am. Chem. Soc.*, 3036 (1988).

56. P. M. E. Quartarone, C. Tomasi, A. Magistris, *J. Phys. Chem. B*, 9610 (1998).

57. M. V. Giotto *et al.*, *Macromolecules*, 3576 (2002).

58. D. Reichert, O. Pascui, P. Judeinstein, T. Gullion, *Chem. Phys. Lett.* **402**, 43 (2005).

59. G. S. MacGlashan, Y. G. Andreev, P. G. Bruce, *Nature (London)* **398**, 792 (1999).

60. Z. Stoeva, I. Martin-Litas, E. Staunton, Y. G. Andreev, P. G. Bruce, *J. Am. Chem. Soc.* **125**, 4619 (2003).

61. A. M. Christie, S. J. Lilley, E. Staunton, Y. G. Andreev, P. G. Bruce, *Nature (London)* **433** 50 (2005).

62. C. Zhang, E. Staunton, Y. G. Andreev, P. G. Bruce, *J. Am. Chem. Soc.* **127** 18305 (2005).

63. S. J. Lilley, Y. G. Andreev, P. G. Bruce, *J. Am. Chem. Soc.* **128**, 12036 (2006).

64. E. Staunton, Y. G. Andreev, P. G. Bruce, *J. Am. Chem. Soc.* **127**, 12176 (2005).

Chapter 2:

Nuclear Magnetic Resonance

Basic NMR Theory

Each atom is made up of electrons, protons, and neutrons (except ^{1}H, which does not have a neutron) that are responsible for the atom's mass, electric charge, magnetism and spin. The nuclei's spin and magnetism are the properties that enable the use of Nuclear Magnetic Resonance (NMR) techniques. The nuclear magnetism is responsible for the magnetic moment (μ) of the atom and the nuclear spin is responsible for the spin of the nucleus. The net nuclear spin of the nucleus is determined by the net proton and neutron spins. Each proton and neutron has a spin of ½, thus an even number of either protons or neutrons results in their net spin equaling 0 due to spin pairing. Thus, nuclei with an even number of both protons and neutrons are NMR inactive (spin = 0). The most commonly used nuclei for NMR are spin = ½ nuclei (^{1}H, ^{19}F, ^{31}P, ^{13}C, ^{15}N), but the majority of NMR active nuclei are spin > ½ and are known as quadrupolar nuclei (^{2}H, ^{14}N, etc). The spinning of the nucleus generates a quantity called angular momentum (S). The ratio between the nuclear magnetic moment and nuclear spin (called the magnetogyric ratio (γ)) relates to various properties of the nuclei (eq. 2.1).

$$\gamma = \mu/S \qquad (2.1)$$

The magnetogyric ratio (rad s^{-1} T^{-1}) helps describe the direction of the magnetic moment (either with or against the magnetic field depending on the sign of the magnetogyric ratio) and the precession rate of the nucleus, called the Larmor frequency (ω^o), with respect to the external magnetic field (B_o).

$$\omega^o = B_o\gamma/2\pi \quad (2.2)$$

Outside the magnetic field, the directions of the magnetic moments (spins) are randomly dispersed. When the nucleus is placed within a magnetic field, the directions of the nuclear magnetic moments align with the external magnetic field B_o (spin up) or the against B_o (spin down). The number of spin up vs. spin down magnetic moment is maintained as an equilibrium that generates the net magnetic moment of the sample. The spin up magnetic moment is the lower energy state, referred to as α, while the spin down magnetic moment is the higher energy state, referred to as β. The larger the gap between the α and β energy states is, the stronger the observed NMR signal. The energy gap between the α and β energy states is directly related to the γ and β^o values for the nucleus as shown in equation 2.3

$$\Delta E=h\gamma B_o /2\pi \quad (2.3)$$

When the sample is placed within the B_o field, the nuclear magnetic moments equilibrate and precess about the B_o field. A Cartesian coordinate system is arranged so that the Z-axis is parallel with B_o. The sample now has an RF coil placed around it that receives applied RF pulses and detects RF frequencies. In a typical 1-D NMR experiment, an RF pulse is applied for a selected duration and power that will rotate the net magnetization from the Z-axis 90^o into the X-axis (referred to as pw90). This aligns all nuclear magnet moments, causing them to precess at the same frequency with the same number of spin up (α) and spin down (β). Since the direction of the net magnetic moment has been aligned with the X-axis, there is no net magnetic moment in the direction of the Z-axis. However, when the RF pulse has subsided, the spins return to equilibrium through two mechanisms: being T_1 spin-lattice (longitudinal) and T_2 spin-spin (transverse) relaxation. These two mechanisms occur simultaneously but are shown independently in Figure 2.1 for clarity. The T_1 process is simply the amount of time it takes for the net magnetization to return to the Z-axis. The T_2 process is sometimes referred to as the “fanning out” of the nuclear spins. This is because the RF pulse aligns all of the nuclear spins causing them to precess at the same frequency, but as time progresses each nuclear spin’s precession frequency slightly fluctuates causing each nuclear spin to have a different precession frequency. As time progresses further, the effect continues to worsen until the nuclear spins have completely fanned out. The T_2 process is responsible for the NMR signal or free-induction decay (FID), and as such it also dictates the width of

the NMR signal. T_2 is inversely proportional (eq. 2.4) to the linewidth; being the faster the T_2 relaxation the wider the NMR signal.

$$\lambda=1/T_2 \qquad (2.4)$$

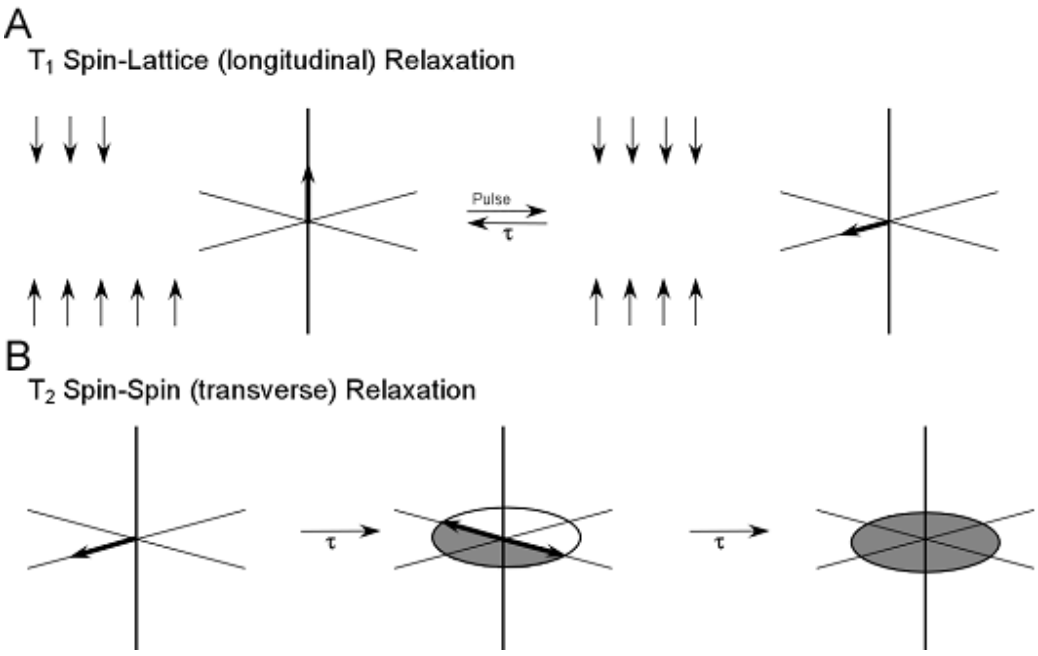

Figure 2.1. Demonstrates the T_1 and T_2 processes. A) shows that the net magnetization along the z-axis goes to 0 when an RF pulse is applied that drives the system to equilibrium. The T_1 relaxation is the return of the net magnetization to the z-axis. B) shows that the T_2 relaxation is the smearing out of the net magnetization in the x-y plane. τ represents a period of time.

Although all of the protons of a particular molecule are precessing, they are not precessing at exactly the Larmor frequency nor are they all precessing at the same rate. This is due to the neighboring atoms and functional groups, which change the shape and density of the electron cloud resulting in the nucleus either being shielded or deshielded. For example, the electron density is decreased when in the presence of an electronegative

element, resulting in the nucleus being deshielded. The shielding effect is a result of the external magnetic field (B_o) causing the electrons to precess, which in turn, causes them to generate their own local magnetic field (B^{loc}). This in turn generates an induced magnetic field ($B^{induced}$), which when summed with B_o either raises or lowers the bulk magnetic field and gives rise to the chemical shift of the nucleus (eq. 2.5). The dependence of chemical shift of an atom to its surroundings allows for a great deal of structural information to be derived from NMR spectroscopy.

$$B^{loc} = B_o + B^{induced} \quad (2.5)$$

NMR of Solids

Line Broadening

The average of all possible molecular orientations with respect to the external magnetic field is termed the isotropy chemical shift value (σ^{iso}). This is typically observed in liquid NMR due to rapid molecular tumbling, causing each molecule to experience all possible orientations with respect to the external magnetic field. However, this is not the case for immobile materials, i.e. solid materials. Solid materials can exhibit isotropy chemical shift values (σ^{iso}) only if they are completely spherically symmetrical, but this is very rare. Thus, most solid materials are asymmetrical and the chemical shift value for

each molecule is dependant upon their orientation to the external magnetic field. Since most solid NMR samples are microcrystalline materials, each crystallite can be oriented differently with respect to the external magnetic field, giving rise to a distribution of chemical shift values. Figure 2.2 shows the spectrum that is obtained form a random distribution of orientations, referred to as the “powder spectrum”. There is a higher probability for the orientations to be perpendicular (higher chemical shift value or more deshielded) than parallel (lower chemical shift value or more shielded) as shown in Figure 2.3.

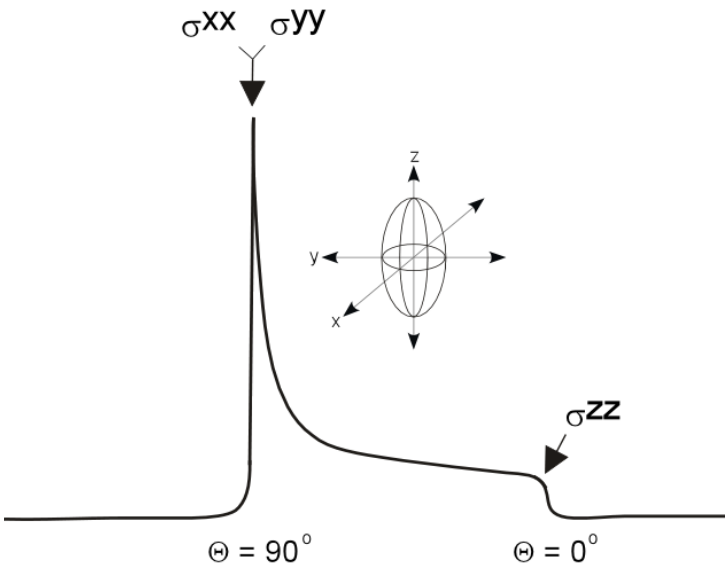

Figure 2.2. Shows the NMR spectrum for a solid with a random distribution of orientations with respect to the external magnetic field. $\Theta=90^{o}$ has a larger intensity due to the higher number of molecules oriented perpendicular to the external magnetic field. The Cartesian coordinate system is superimposed with an ellipsoid that is symmetrical about the z-axis. This gives rise to the spectrum shown and has the σ^{xx}, σ^{yy}, and σ^{zz} values indicated (these tensors will be used in the following discussions).

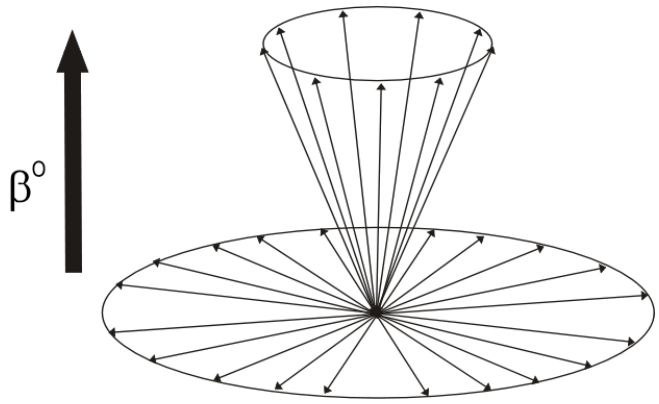

Figure 2.3. Shows the larger number of molecules perpendicular to the external magnetic field when compared to the number or molecules parallel to the external magnetic field.

Although the powder spectrum is very broad, there is some structural information that can be obtained from it. The information that can be collected from the powder spectrum is the isotropic chemical shift (σ^{iso}), the chemical shift anisotropy tensor (Δ_{CSA}), and the asymmetrical parameter (η). The values of these parameters are dependent upon the symmetry of the electron cloud about the nucleus in question. In particular, the asymmetrical parameter (η) describes the axial shape of the electron cloud about the nucleus. The equations for isotropic chemical shift (σ^{iso}), the chemical shift anisotropy tensor (Δ_{CSA}), and the asymmetrical parameter (η) are shown below in equations 2.6 - 2.8.

$$\sigma^{iso} = (\sigma^{xx} + \sigma^{yy} + \sigma^{zz})/3 \qquad (2.6)$$

$$\Delta_{CSA} = \sigma^{zz} - \sigma^{iso} \qquad (2.7)$$

$$\eta = (\sigma^{xx} + \sigma^{yy})/(\sigma^{zz} - \sigma^{iso}) \qquad (2.8)$$

The σ^{xx}, σ^{yy}, and σ^{zz} terms are generated from solving the linear algebra equation for all the different possible vectors, which results in all vectors, except for the diagonal vectors (σ^{xx}, σ^{yy}, and σ^{zz}), canceling out as shown below (eq. 2.9).

$$\sigma = \begin{Bmatrix} \sigma^{xx} & \sigma^{yx} & \sigma^{zx} \\ \sigma^{xy} & \sigma^{yy} & \sigma^{zy} \\ \sigma^{xz} & \sigma^{yz} & \sigma^{zz} \end{Bmatrix} \qquad \sigma = \begin{Bmatrix} \sigma^{xx} & 0 & 0 \\ 0 & \sigma^{yy} & 0 \\ 0 & 0 & \sigma^{zz} \end{Bmatrix} \qquad (2.9)$$

In equations 2.6 – 9 the identity of the σ terms are defined as $|\sigma^{zz} - \sigma^{iso}| \geq |\sigma^{xx} - \sigma^{iso}| \geq |\sigma^{yy} - \sigma^{iso}|$. The powder spectrum shown in Figure 2.1 represents a case were there is axial symmetry, i.e. $\sigma^{xx} = \sigma^{yy}$. However, many solid samples have no axial symmetry, which results in the powder spectrum shown in Figure 2.4. η values measures the degree that the samples deviates from axial symmetry; with an axially symmetric sample having an η value of 0 and a completely asymmetrical sample having an η value of 1. Thus, the larger the η value the higher degree of axial asymmetry present in the sample. Although there is useful information that can be gained from the powder spectrum, the typical sample has several signals that overlap resulting in very poor resolution, which greatly hinders the interpretation of solid-state NMR spectra (SSNMR).

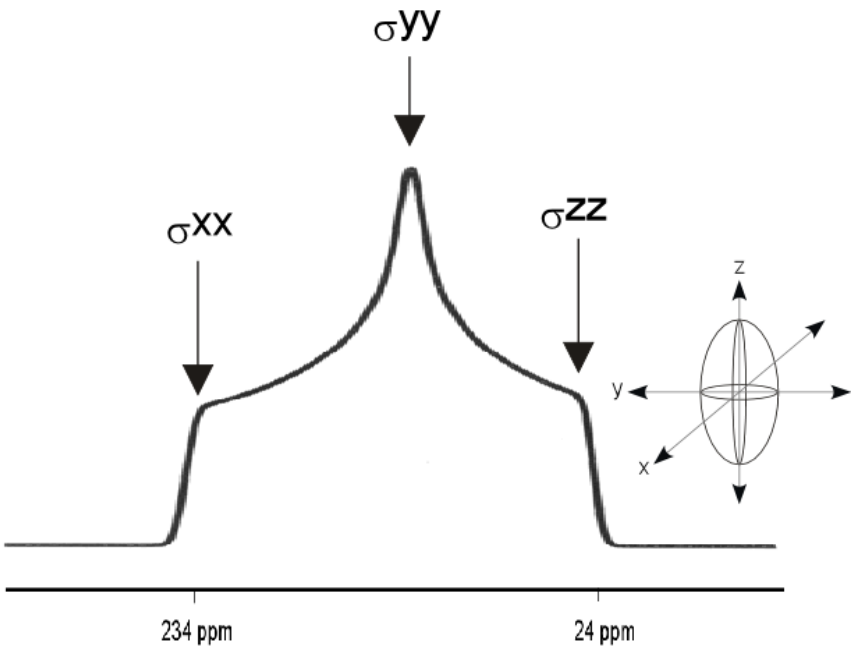

Figure 2.4. Shows the powder spectrum of an asymmetrical solid sample with a random distribution of orientations with respect to the external magnetic field. The Cartesian coordinate system is superimposed with an ellipsoid that is asymmetrical the x, y, and z-axis. This gives rise to the spectrum shown above with the σ^{xx}, σ^{yy}, and σ^{zz} values indicated (these tensors will be used in the following discussions). The larger intensity at σ^{yy} is due to the higher number of molecules oriented perpendicular to the external magnetic field.

The main cause for the line broadening seen in powder spectra are chemical shift anisotropy (CSA) and dipolar interactions. First, the line broadening caused by CSA is addressed. The Hamiltonian for the chemical shift interaction is given below in equation 2.9.

$$H_{cs} = \sigma^{iso} \gamma B_o \hat{I}_z + 0.5\, \delta_{cs}(3\cos^2 \Theta - 1)\hat{I}_z \quad (2.9)$$

This equation posses two parts, the isotropic chemical shift value (first term) and the molecular orientation dependence of the chemical shift value (second term). The molecular orientation is represented by Θ, which is the

angle between nuclei with respect to the external magnetic field as shown in Figure 2.5. There are various possible orientations for the molecule, with respect to the magnetic field, that results in the nucleus experiencing various shielding effects. Since, the observed chemical shift is dependent on the shielding effects, the NMR signals are very broad (shown in Figure 2.6)

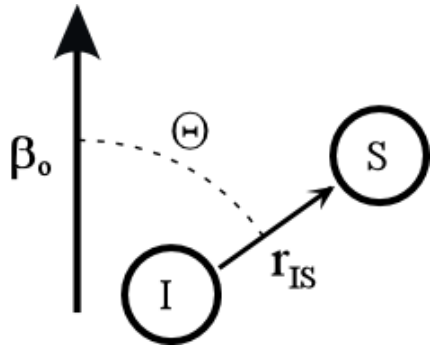

Figure 2.5. Shows that the angle Θ, is defined as the angle between the molecule and the external magnetic field.

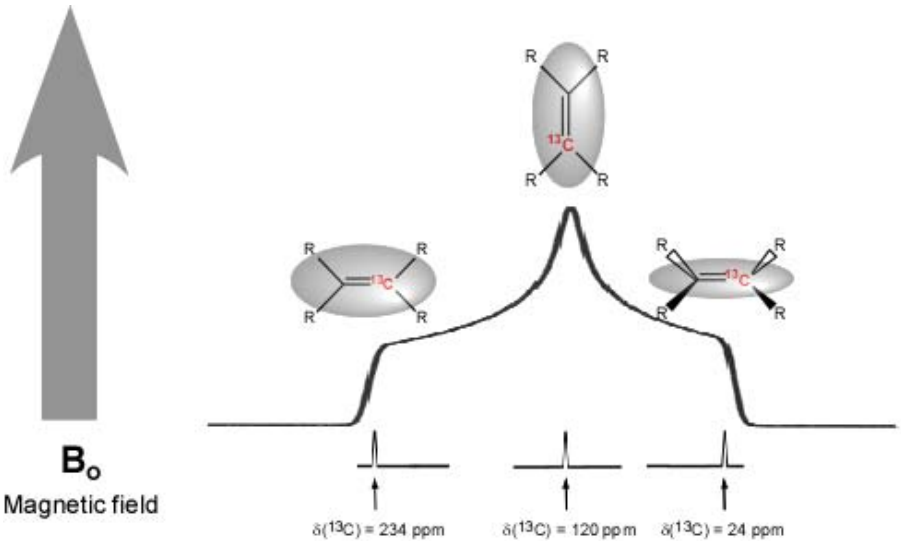

Figure 2.6. Displays the large linewidth caused by the CSA of an asymmetrical compound. Above the spectrum is a representation of the compounds electron cloud orientation with respect to the external magnetic field for σ^{xx}, σ^{yy}, and σ^{zz}. Below the spectrum are the corresponding NMR signals the σ^{xx}, σ^{yy}, and σ^{zz}. These large differences in chemical shifts are due to the difference in shielding effects caused by the asymmetry of the electron cloud.

The rest of the line broadening is due to the nuclear spin interaction between neighboring nuclei called dipole-dipole interactions or dipolar coupling. This is a through-space interaction whose dipolar coupling strength varies depending on the internuclear distance ($1/r^3$) and angle Θ between the neighboring nuclei. The amount that one nuclear spin (S) interacts with another nuclear spin (I) is depicted by the dipolar coupling constant (eq. 2.10).

$$D=(h/2\pi)(\mu_o/4\pi)(\gamma^I\gamma^S/r^3) \qquad (2.10)$$

The dipolar-coupling constant is primarily governed by the distance between the S and I spins ($\gamma^I\gamma^S/r^3$) and eventually goes to zero as the spins are moved apart. There are two types of dipole-dipole interactions being homonuclear (eq. 2.11) and heteronuclear (eq. 2.12). The Hamiltonians for each are shown below.

$$H^{homo} = -D(0.5)(3\cos^2\Theta-1)[3I_zS_z-I*S] \qquad (2.11)$$

$$H^{hetero} = -D(3\cos^2\Theta-1)I_zS_z \qquad (2.12)$$

The orientational dependence of each is represented by the $(3\cos^2\Theta-1)$ term. The result of homonuclear dipolar coupling is a homogeneous broadening of the NMR spectrum as shown in Figure 2.7.

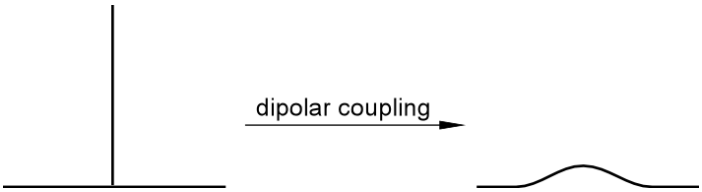

Figure 2.7. Demonstrates the broadening result of dipolar interactions on the NMR signal.

Isolated heteronuclear spin pairs that are randomly oriented in a solid, result in two superimposed powder spectra (one for each nucleus) referred to as a "Pake pattern" shown in Figure 2.8.

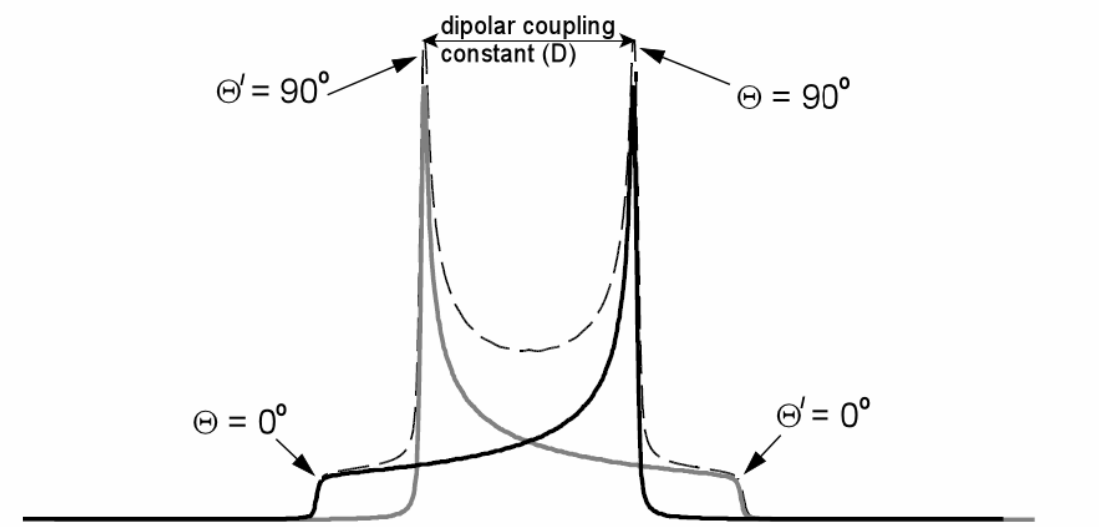

Figure 2.8. Demonstrates the Pake pattern (collected under non-spinning conditions) that is observed for an isolated heteronuclear spin pair randomly oriented within the external magnetic field. The Pake pattern consists of two powder spectra, one for each nucleus. When combining these two powder spectra, a Pake pattern is generated with a higher intensity between the "horns" due to the higher probability of the orientations being perpendicular.

The two sharp peaks are referred to as "horns" and the distance between the horns is dependent on the dipolar-coupling constant (D) of the isolation spin pair. The different frequencies between the two powder spectra are dependent on their orientation ($3\cos^2\Theta$-1), and the large intensity in the

middle is due to the number of orientations that are perpendicular to the external magnetic field.

Magic Angle Spinning (MAS)

The line broadening mentioned above is detrimental to the analysis of complex solid samples. Equation 2.9, 2.11, and 2.12 describe the effects of anisotropy and dipole coupling interactions on line broadening. All of these equations have the term $(3\cos^2\Theta-1)$, which is a description of their orientation dependence with respect to the external magnetic field. This term goes to zero when $\Theta = 54.73^\circ$, which is known as the "magic angle". Thus, placing a sample in the external magnetic field at the magic angle averages away the anisotropy and dipolar coupling effects for the molecules that are oriented along the magic angle. This works well with single crystals, but most solid samples consist of a microcrystalline powder that will only have a small fraction of the crystallites oriented correctly. However, by spinning the independent orientations of the crystallites along the magic angle, the average of the crystallites will be 54.73°, and is shown in Figure 2.9.

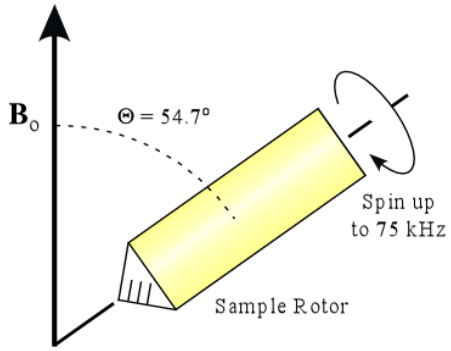

Figure 2.9. Demonstrates that the sample is orientated at the magic angle with respect to the external magnetic field and spun at speeds up to 75 kHz hence the term magic angle spinning (MAS).

The strength of the anisotropy effect is a few kHz, but the heteronuclear dipolar coupling strength between ^{1}H and ^{13}C are 10-30 kHz, while the homonuclear dipolar coupling strength between protons is as strong as 100 kHz, and the dipolar coupling strength between ^{13}C's are as strong as 3 kHz. Currently, the fastest spinning rate is 75 kHz, but our experiments used spinning rates $\leq$ 9 kHz. Thus, the spinning rate is not fast enough to overcome these large dipolar interactions with MAS. These interactions are overcome through high power RF irradiation decoupling of the proton, which removes the heteronuclear dipolar interaction between ^{1}H and ^{13}C. With the proton dipolar interactions destroyed by proton decoupling we are left with the effect from the chemical shift anisotropy (CSA).

Another way to describe the effect of dipolar coupling interaction is with respect to the T_2 process. The T_2 relaxation is enhanced through dipole interactions of the neighboring nuclei causing the spin intensities to fan out. This is detrimental for the resolution of NMR signal since the linewidth is proportional to the reciprocal of the T_2 rate. Thus, a fast T_2 results in a very

broad NMR signal. MAS averages away the T_2 relaxation by changing the sample orientation to the external magnetic field resulting in the direction of the fanning out process being changed (Figure 2.10).

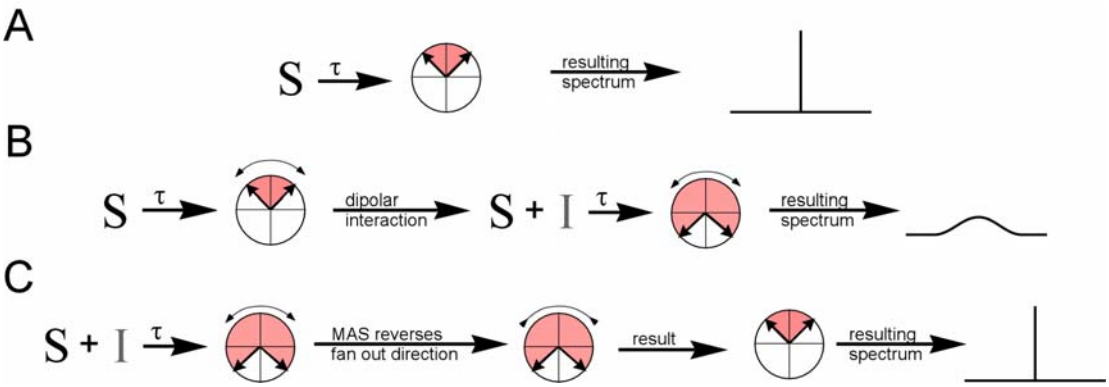

Figure 2.10. Demonstrates the effects of dipolar interaction and MAS effect on dipolar interactions. A) Demonstrates the normal T_2 relaxation exhibited by a nucleus (S) absent from dipolar interaction of other nuclei, resulting in a narrow NMR signal. B) Demonstrates that dipolar interaction from other nuclei (I) significantly increases T_2 relaxation, resulting in broad NMR signals. C) Demonstrates that through spinning of the sample at the magic angle the direction of the fanning out of the spins from T_2 relaxation is reversed, resulting in the observed NMR signal (narrow) of a nucleus absent from dipolar interactions of other nuclei.

The solid-state NMR spectrum is composed of isotropic peaks and a series of peaks that are equally spaced from the isotropic peaks. These peaks are called “spinning sidebands” and their distance from the isotropic peak is equal to the spinning speed of the sample as shown in Figure 2.11.

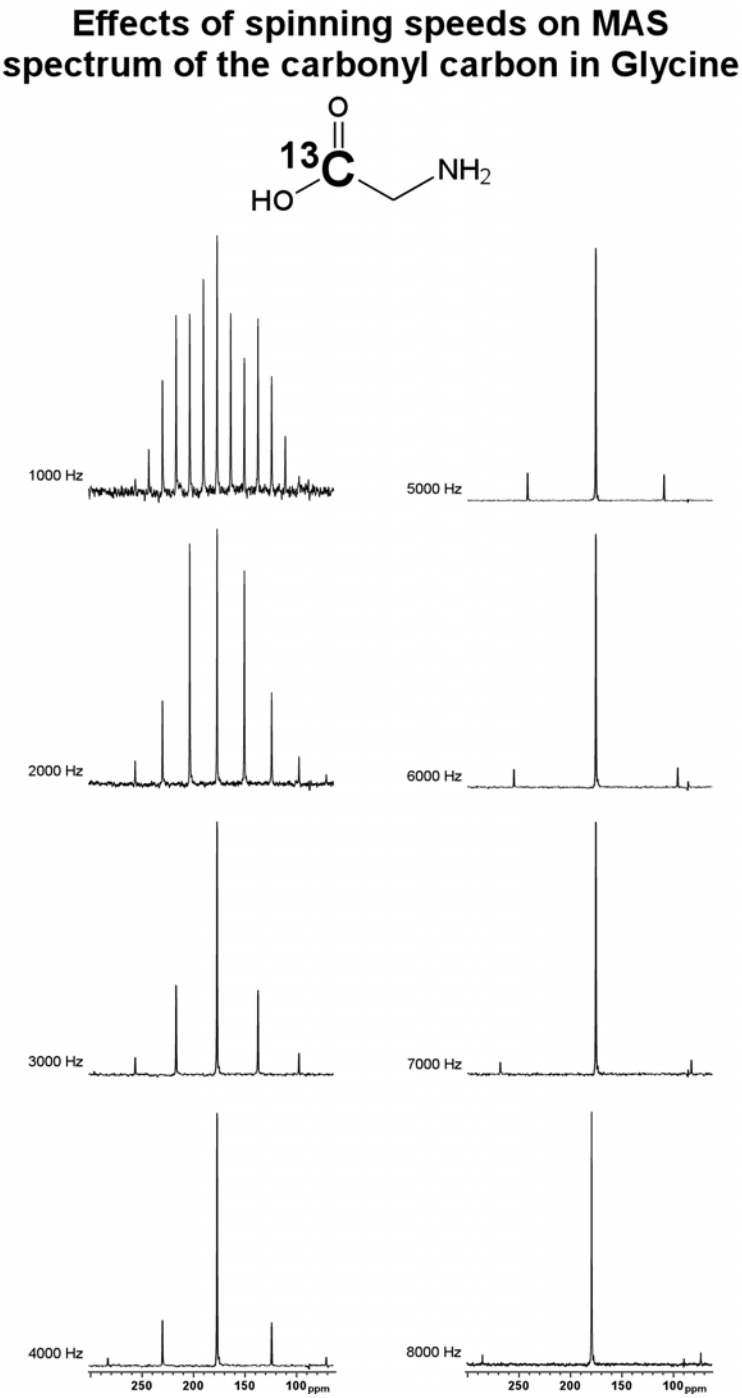

Figure 2.11. Demonstrates the effect of the spinning speed on the carbonyl isotopic peak of glycine. The series of peaks surrounding the isotropic peak (the center peak in the series of peak located at 176ppm) are called “spinning sidebands”. These are a product of incomplete averaging from MAS and appear at intervals that correspond to the spinning speed. As shown above the faster the spinning speed, the further apart the spinning side bands. Also the faster the spinning speed, the more efficient the MAS averaging, resulting in an increase in signal to noise and a decrease in the intensity of the spinning sidebands.

The spinning sidebands are present due to incomplete averaging, and they roughly map out the powder spectrum at slow spinning speeds (< 5 kHz). Thus, the intensity and distribution of the spinning side bands are dependant upon the shape and density of the electron cloud allowing the Δ_{CSA} and η values to be solved in the same fashion as previously mention with powder spectra. For these reasons our phosphorus spectra, seen in chapter 5 and 6, were collected at a spinning speed of 3 kHz. This results in a series of spinning sidebands that are unique for each phosphorus environment. Mapping of these unique spinning sidebands allows the Δ_{CSA} and η values for each unique phosphate environment to be solved, with the aid of the STARS simulation program supplied by Varian.Inc. Since slow spinning speeds result in these spinning sidebands due to incomplete averaging of the CSA and dipolar interactions, better resolution can be obtained with higher spinning speeds. Thus, currently small ceramic sample rotors can be spun at speeds as high as 75 kHz, but this results in the loss of the spinning sidebands and the information gained from them.

Cross Polarization Magic Angle Spinning (CPMAS)

Cross Polarization Magic Angle Spinning (CPMAS) forms the backbone of a large portion of typical SSNMR experiments. CPMAS increases the resolution and sensitivity for either low abundance or low γ nuclei (^{15}N, ^{13}C, etc.) by transferring polarization from high γ nuclei (^{1}H and

^{19}F). As previously mentioned, the energy level splitting between the α and β energy states is primarily determined by their γ and the external magnetic field strength. Thus, nuclei with large γ are more sensitive, while nuclei with small γ are less sensitive. CPMAS increases the sensitivity of the small γ nuclei (nuclei X) by transferring proton polarization to nuclei X. Cross polarization is possible because of the dipolar interaction between the protons and nuclei X, thus the samples must be solid (non-mobile) and protons must be close.

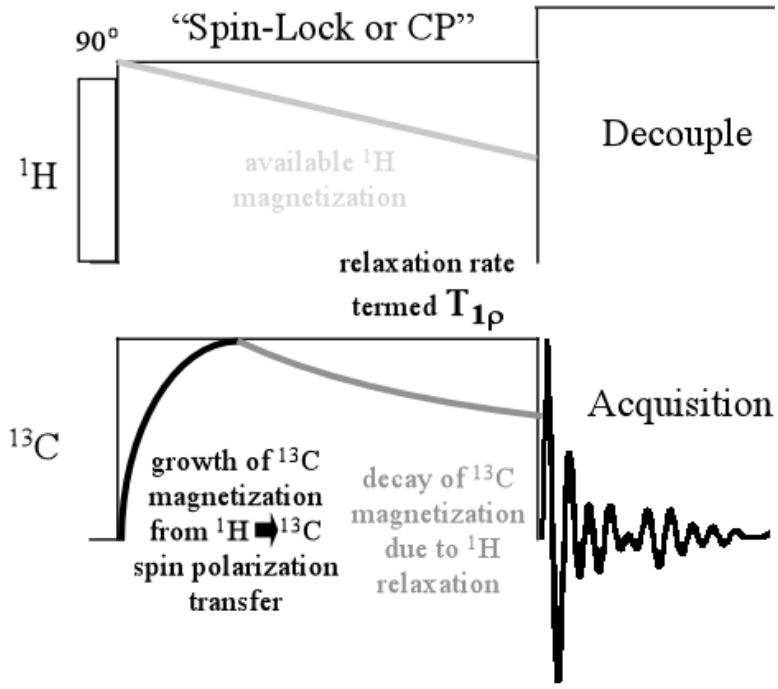

Figure 2.12. Shows the CPMAS pulse sequence.

Figure 2.12 shows the pulse sequence for a CPMAS experiment. First, proton net magnetization is flipped to the x-y plane with a 90-degree pulse followed by a "spin-lock" pulse, which maintains the proton magnetization along the x-axis, preventing relaxation back to the z-axis.

Simultaneously the net magnetization for nuclei X is also pulsed into the x-axis. Although the proton and nuclei X spins are now precessing about the x-axis, cross polarization cannot be achieved due to their different Larmor frequency (precession rates). In order for polarization transfer to occur between the two nuclei, they have to be precessing around the x-axis at the same rate or be "spin-locked". The precession rate of nuclei X is artificially increased with a strong RF field until proton and nuclei X are precessing at the same rate. This process is referred to as "Hartmann-Hahn matching" and is shown in Figure 2.13. After spin-locking is achieved, the FID is acquired while the undesirable proton effects are simultaneously decoupled away. The period of time it takes for the spin-locking to occur is referred to as the contact time.

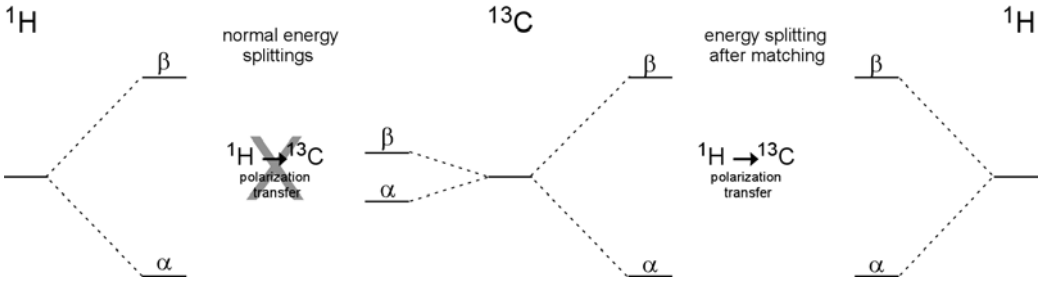

Figure 2.13. Shows a schematic representation for Hartmann-Hahn matching. The left side of the figure shows the normal energy splitting between ^{1}H and ^{13}C. Here, polarization transfer is not possible due to the difference in precession rates, resulting in the Hartmann-Hahn matching conditions not being met. The right side of the figure shows the energy splitting between the ^{1}H and ^{13}C after strong decoupling power is applied to the ^{13}C nucleus, resulting in the precession rate and energy splitting between ^{1}H and ^{13}C being equal. This satisfies the Hartmann-Hahn matching condition and polarization is transfer from ^{1}H to ^{13}C.

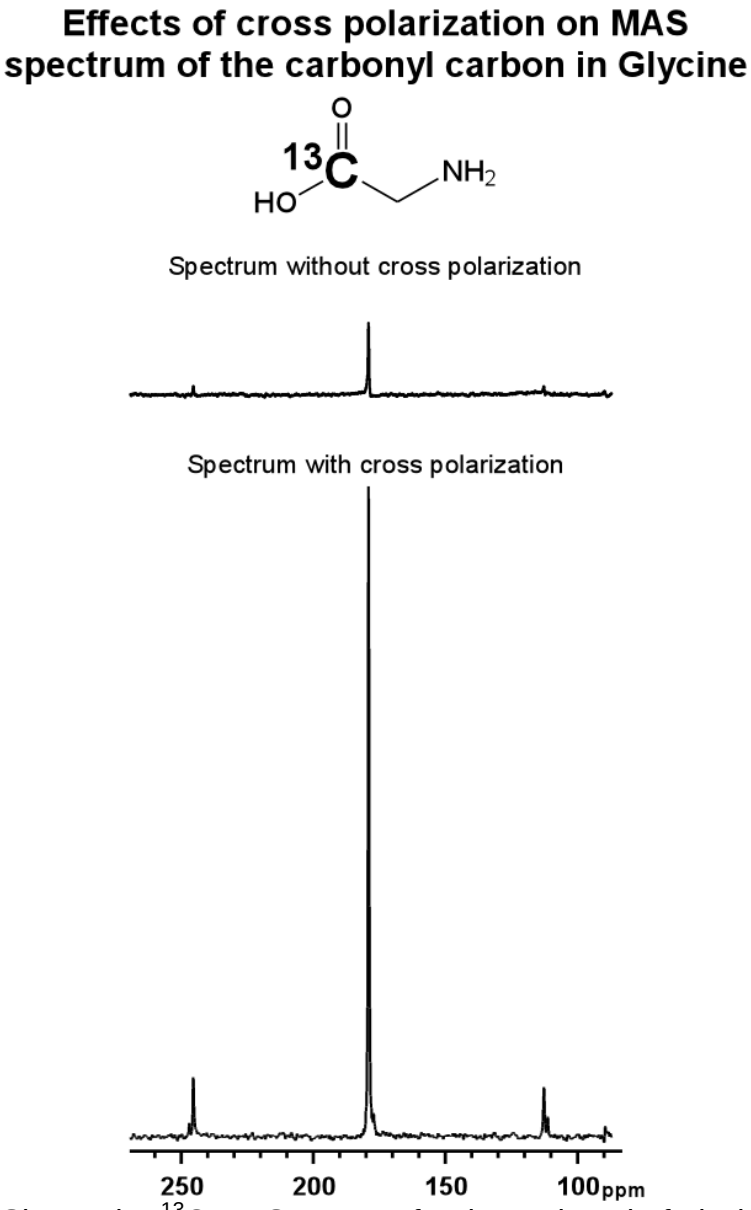

Figure 2.14. Shows the ^{13}C MAS spectra for the carbonyl of glycine collected at a spinning speed of 5 kHz without (top) and with (bottom) cross polarization. The spectrum collected with cross polarization shows drastic increase in signal intensity.

CPMAS is highly desirable for the added signal sensitivity (maximum increase of γ^H/γ^X) as shown in Figure 2.14. Another added bonus is that the mobility of samples can be measured with the efficiency of polarization transfer. The period of time that the two nuclei are spin-locked (transfer of

proton polarization) is called contact time. Every sample has a different optimum contact time that is dependant upon the rate that the proton magnetization is lost. The lost of proton magnetization is governed by the proton's T_1 and T_2 relaxation rates. Thus, collecting spectra at various contact times allows for the observation of the magnetization build up and decay (T_{IS} curve). The decay of signal intensity in the T_{IS} curve is directly related to proton's T_1 and T_2 and is called $T_{1\rho}$. This decay in signal intensity is due to the loss of proton polarization. The rate of this decay is often times used to describe the molecular motion of the sample. However, since there is more than one mechanism for relaxation to occur, interpretation of $T_{1\rho}$ can vary. In order to correctly interpret $T_{1\rho}$ data, it is imperative to identify and understand the different pathways that are responsible for relaxation.

The two different mechanisms responsible for relaxation are dipole – dipole interactions and chemical shift anisotropy. Dipole – dipole interactions cause relaxation due to the transfer of magnetization between two nuclei through spin interactions. Thus, the relaxation rate through dipole – dipole interactions depends on the distance between the interacting nuclei and relaxation rates are independent of the external magnetic field. However, relaxation due to chemical shift anisotropy is highly dependent on the external magnetic field. As previously discussed the chemical shift is a product of the precession of the surrounding electrons generating an induced magnetic field. Relaxation caused by chemical shift anisotropy occurs due to transfer of magnetization from the nuclei into the surrounding electronic magnetic field.

As the external magnetic field strength is increased the precession of the electron increases, thereby increasing the strength of the induced magnetic field from the electrons. This increase in the induced magnetic field allows for faster and more efficient transfer of magnetization, resulting in a faster relaxation rate.

Since the $T_{1\rho}$ rate is generally governed by molecular interactions and mobility, it is often used to help describe structure and dynamics of the sample. An example of T_{IS} and $T_{1\rho}$ rates is shown in Figure 2.15, here the fast signal decay of pure LTA indicates more molecular motion than absorbed species on TiO_2. It is important to note that cross polarization can only occur in systems that exhibit dipolar coupling between the nuclei being observed and protons; thus, for highly mobile systems (such as liquids) all dipolar coupling are destroyed resulting in the inability to perform CPMAS.

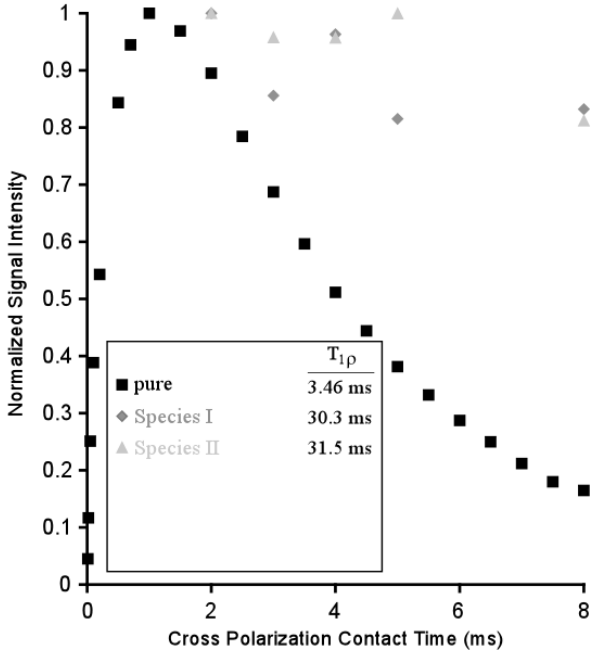

Figure 2.15. Shows the T_{IS} curves and $T_{1\rho}$ rates for pure LTA (pure) and LTA absorbed onto TiO_2 (species I and II). Here, the relaxation rates for species I and II are significantly slowed by the diminished motion due to the adhesion of LTA onto TiO_2. This is observed by the strong signal intensity at long contact times. However, the signal intensity of pure LTA continuously decreases at longer contact times due to the higher degree of molecular motion.

Rotational Echo DOuble Resonance (REDOR)

REDOR is used in solid-state NMR to measure the distance between two different nuclei through dipole-dipole coupling.(*3-6*) This experiment is based on CPMAS and uses a third channel to selectively reintroduce the dipole interaction, normally averaged away with MAS, of a particular nucleus. The REDOR experiment requires the acquisition of 2 NMR spectra collected under magic angle spinning (MAS) conditions. The first spectrum, labeled $S_{0,}$ is collected using decoupling (^{1}H) and observe spin (denoted S-

spin, ^{13}C) RF pulses only. This spectrum is a typical CPMAS experiment that results in the averaging away of dipolar coupling effects by the use of MAS, thus the NMR signal(s) have full intensity. A second spectrum, labeled S_r, is collected using identical ^{1}H and ^{13}C pulses, with RF pulses applied to third channel nucleus (denoted the I-spin, ^{7}Li for these experiments) at selected intervals. The I-spin pulses reintroduce the dipolar interaction that otherwise would be averaged away by MAS, causing a decrease in NMR signal intensity (shown in Figure 2.16).

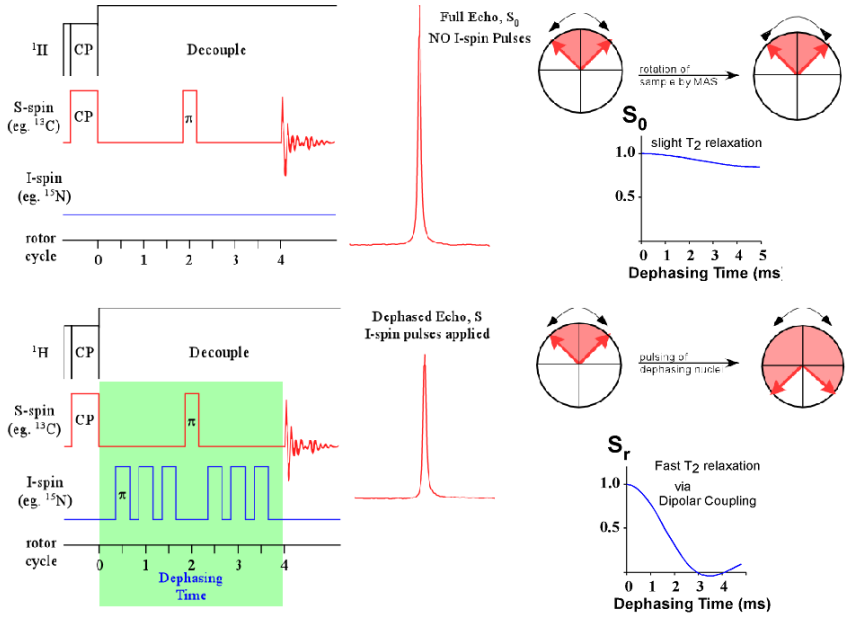

Figure 2.16. Shows the pulse sequence for REDOR and its effects on the observed spectra. A) shows the S_0 spectrum obtained with a typical CPMAS pulse sequence. This results in a "full echo" spectrum, which has had the dipolar interactions removed with MAS. However there are slight T_2 relaxation effects that cannot be fully averaged away. B) shows the S_r spectrum obtained by using two π pulses per rotor cycle to reintroduce the dipole-interactions. This results in a "dephased echo" spectrum that has enhanced T_2 relaxation due to dipolar coupling, which increases as dephasing period is increased.

The reduced signal intensity is caused by transverse dephasing (T_2 relaxation) of the magnetization due to reintroduced dipole-dipole interaction

of the selected spin pair. Subtracting the "dephased echo (S_r)" spectrum from the "full echo (S_0)" spectrum provides a difference spectrum (ΔS). Although the I-spin RF pulses that cause dephasing each have a fixed duration, using more pulses can increase the amount of transverse dephasing. Longer dephasing times decrease S_r, which increases ΔS. The distance between ^{13}C and ^{7}Li can be found by relating the intensity of ΔS to the dephasing time. However, other T_2 processes may cause additional signal loss, affecting both S_0 and S_r, so their effect is corrected for by dividing ΔS by S_0. Thus, by collecting a series of S_0 and S_r, with different durations of dephasing times, a sinusoidal plot is generated called the "REDOR dephasing curve". Plotting $\Delta S/So$ vs. dephasing time generates the REDOR dephasing curve shown in Figure 2.17. The initial rise of this curve is used to determine the primary dipolar coupling constant (solved with the aid of the SIMPSON simulation program discussed below), resulting in the ability to solve for the internuclear distance with equation 2.13.

$$D = (\mu_o \hbar/4\pi)(\gamma^I \gamma^S/r^3) \qquad (2.13)$$

D from the equation above is the dipolar-coupling constant, μ_o is the permittivity of free space, γ^I is the magnetogyric ratio of the dephasing nuclei (^{7}Li), γ^S is the magnetogyric ratio of the observe nuclei (^{13}C), and r is the internuclear distance. The dipolar coupling constant is determined through the aid of the SIMPSON program. The SIMPSON program simulates

REDOR dephasing curves for specific dipolar coupling constants, which are fitted with the experimentally obtained REDOR dephasing curve until good agreement is reached. This results in the dipolar coupling constant being solved, which allows for the distance between the nuclei to be solved with eq. 2.13. Figure 2.17 also demonstrates that the shorter the distance is between nuclei, the steeper the initial rise of the REDOR dephasing curve (due to a larger dipolar coupling constant).

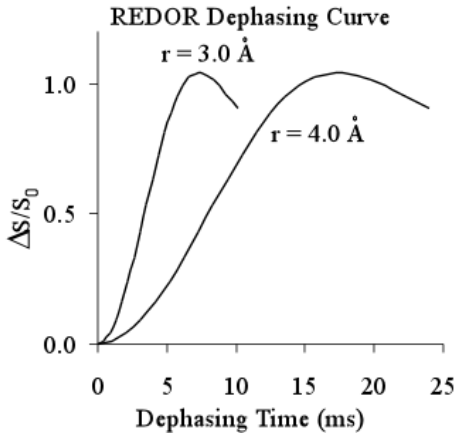

Figure 2.17. Shows the universal REDOR curves for nuclei that are 3 and 4 Å apart. The initial rise of the universal REDOR curve is unique to the distance between nuclei and a small change in these distances generates large changes in the observed rise of the universal REDOR.

Deuterium Wideline

^{2}H Wideline solid-state NMR (SSNMR) experiments are useful in detecting the mobility of the molecules in question. When a static (non-spinning) SSNMR spectrum of a quadrupole nuclei sample (nuclei with nuclear spin > ½) is collected, such as deuterium, the pake pattern is observed with the distance between the horns being a measurement of the quadrupole-coupling constant of the nuclei. The quadrupole-coupling

strength is directly affected by motion, which averages away the quadrupole-coupling constant. Thus, the change in distance between the horns enables us to observe changes in molecular motion. Figure 2.18 shows how the deuterium spectra changes as mobility are increase.

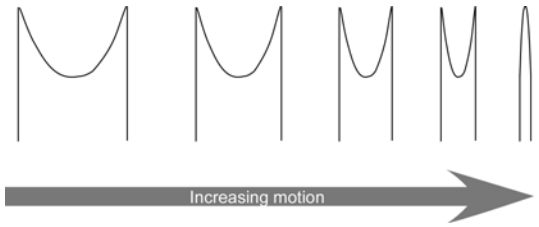

Figure 2.18. Demonstrates that the distance between the horns of the Pake pattern decreases as molecular motion increases. This makes static deuterium NMR experiments a powerful tool for detecting changes in molecular motion.

Deuterium NMR is collected under non-spinning (static) conditions with a horizontal NMR probe. The spectra are obtained using the quadrupolar echo pulse sequence shown in Figure 2.19. This pulse sequence consists of a delay period, followed by a pw90 ($\pi/2$) and a short delay (τ), then another pw90 ($\pi/2$) and a short delay period and then data acquisition. Generally the τ periods are equal to each other and range from 20-50 μs with the pw90 being in the 1.5 μs time range.

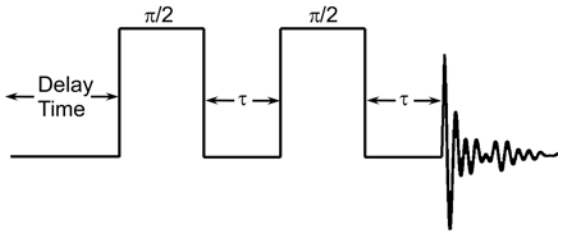

Figure 2.19. Shows the quadrupolar echo pulse sequence.

Reference:

1. M. J. Duer, *Introduction to Solid-State NMR Spectroscopy* (Blackwell publishing, Malden, MA, 2004), pp.

2. M. H. Levitt, *Spin Dynamics: Basics of Nuclear Magnetic Resonance* (John Wiley & Sons Inc., Hoboken, NJ, 2001), pp.

3. L. M. McDowell, J. Schaefer, *Current Opinion in Structural Biology* **6**, 624 (1996).

4. J. Schaefer, *Encyclopedia of Nuclear Magnetic Resonance* R. K. Harris, Ed. (John Wiley, New York, 1996) pp. 3983-3984.

5. T. Gullion, J. Schaefer, *J. Magn. Reson.* **81**, 196 (1989).

6. T. Gullion, *Concepts Magn. Reson.* **10**, 277 (1998).

Chapter 3:

Systematic Solid-State NMR Study of PEO and PEO Lithium Electrolytes

Chapter 3 consists of 3 sections.

Section 1: NMR Signal Assignments for the Amorphous and Crystalline Domains of PEO and PEO Electrolytes

Introduction:

Poly(ethylene oxide) (PEO), [$(CH_2CH_2O)_n$], is the most widely studied material for use as a solid polymer electrolyte (SPE) host. The presence of a donor oxygen atom allows complexation with group 1 and 2 salts as well as some transition metal salts.(*1, 2*) The ability to dissolve metal salts, combined with a low glass transition temperature (T_g = -60 ºC), has led many laboratories to investigate PEO-based SPE's.(*1-9*) However, more information is needed to improve PEO's ionic conductivity and mechanical properties.

Dilute PEO electrolytes consist of a crystalline pure PEO phase, a crystalline PEO-salt phase, and an amorphous phase containing some dissolved salt.(*3, 9-11*) It is believed that ionic conductivity is facilitated by polymer segmental motion in the amorphous region.(*3*) Reducing the

crystallinity at room temperature increases the amount of amorphous phase, thereby enhancing conductivity; thus, efforts have focused on reducing crystallinity with various plasticizers and copolymers.(*1, 12-14*) Characterizing subsequent changes to the lithium environment and phase distributions would be beneficial, enabling researchers to identify the interactions that impede lithium mobility, and also to identify the best method to encourage lithium transport.

As the formation of the crystalline region is detrimental to the performance of solid polymer electrolytes, there have been numerous investigations of the conditions that favor crystalline formation.(*15-19*) AC impedance studies of ionic conductivity have shown that over time the conductivity decreases due to the growth of the crystalline region.(*17, 18*) IR/RAMAN studies have also shown that crystalline domains are present within seconds after preparation of a thin film electrolyte, and that crystallization continues after the preparation of a thin film electrolyte.(*5, 18*) Age, method of preparation, and thermal history are all known to change the crystalline content of polymer electrolytes.(*15-18*)

For PEO:Li salt systems, numerous techniques, such as differential scanning calorimetry and complex AC impedance, are available to study the physical and conductivity properties of PEO-based SPE's, but none of these techniques provide fundamental chemical insight into the PEO:Li chemical structure. Low temperature X-ray crystallography has provided a structure for crystalline 3:1 PEO:LiTf systems.(*20*) However, this method cannot be used

on dilute PEO:salt systems due to insufficient long-range structural order necessary for diffraction.(*15*)

The ^{13}C CPMAS spectra of pure PEO and dilute salt PEO complexes show a broad and a narrow NMR signal that are superimposed. For pure PEO, these components have been assigned to the amorphous and the crystalline domains, but the assignments have varied. Connor et al. originally used proton spin lattice relaxation to study the heterogeneous nature of pure PEO.(*21*) The broad component, with a fast relaxation rate, was assigned to the amorphous region. While the narrow component, with longer relaxation rates, was assigned to the crystalline region. This assignment was later revised by Dechter who assigned the broad component to the crystalline and the narrow component to the amorphous based on a reanalysis of the proton and ^{13}C rotating frame spin lattice relaxation data ($T_{1\rho}$).(*22*) Tegenfeldt *et al*. reanalyzed and agreed with the results found by Dechter.(*23*)

All NMR studies of PEO electrolytes since Dechter have used his pure PEO assignments. Proper assignment is important for VT NMR experiments (used to understand polymer backbone dynamics) and REDOR NMR experiments (used to elucidate local structure). However, pure PEO and PEO electrolytes are fundamentally different samples and interchanging the NMR assignments should not be taken lightly. Thus, we have investigated and assigned the NMR signals for the amorphous and crystalline phases of a dilute PEO electrolyte. We have the benefit of using the 3:1 PEO:LiTf sample, which is crystalline, as a standard to aid in the assignment of the

crystalline region. It has been previously demonstrated that high salt concentrations only retain the narrow component while the more dilute PEO-salt samples contain both the narrow and broad components.(*24-26*) However, NMR assignments for the amorphous or crystalline region in the PEO:salt systems have not been made. With the recent introduction of REDOR NMR experiments, it is now imperative to accurately assign the NMR components that represent the amorphous and crystalline regions.

Using ^{13}C $T_{1\rho}$ data for the 3:1 PEO:LiTf sample, we assigned the narrow component to the crystalline region. However, assigning the 20:1 PEO:LiTf sample is more complicated, arising from the heterogeneous nature of these samples. In dilute PEO:salt electrolytes, there exist 4 possible regions: 1) pure amorphous PEO, 2) pure crystalline PEO, 3) lithium containing amorphous PEO, and 4) lithium containing crystalline PEO. Phase diagrams only show the presence of pure crystalline PEO and crystalline PEO:salt complex,(*11*) while IR/RAMAN studies show amorphous PEO:salt phase but no pure amorphous PEO.(*5*) Thus, PEO electrolytes only have 3 regions: 1) pure crystalline PEO, 2) lithium containing amorphous PEO, 3) lithium containing crystalline PEO. Previous solid-state NMR studies assign the narrow ^{13}C peak to the amorphous region, while the broad peak represents the crystalline region for pure PEO, but no direct assignments have been made for dilute PEO:salt complexes. It is unclear whether the broad peak for the dilute PEO:salt electrolytes is due to a mixture of pure crystalline PEO and amorphous PEO:LiTf regions. Alternatively, the broad

component may arise solely from the amorphous PEO:LiTf regions. To clarify assignment of the ^{13}C data, we reinvestigated the NMR spectrum of pure PEO using samples of pure powdered 100 kDa PEO, annealed pure powdered 100 kDa PEO, and a thin film of 100 kDa PEO cast from an acetonitrile solution. These different samples produced a narrow NMR peak under conditions that favored crystalline formation. Thus, we have reassigned the narrow peak to the crystalline region and the broad peak to the amorphous region for pure PEO. Additional ^{13}C solid-state NMR experiments with PEO:LiTf electrolytes were used to assign the broad component of the NMR signal to amorphous PEO:LiTf region and the narrow component to the crystalline PEO and PEO:LiTf regions. These assignments are reversed from that of Dechter and Tegenfeldt, thus prior NMR experiments of pure PEO and PEO electrolytes that rely on the previous assignments need to be reexamined.

Experimental:

Sample preparation

Poly (ethylene oxide) (PEO) with an average molecular weight of 2000 Da (Polysciences, Inc.) and 100,000 Da (Sigma-Aldrich) were used as received. Anhydrous acetonitrile (99.8%) was obtained from Aldrich and used as received. Lithium trifluoromethanesulfonate (lithium triflate, LiTf) was obtained from Aldrich and dried in a vacuum oven at 120 ºC for 48 hours prior

to use. All chemicals were stored and used in a dry argon or nitrogen atmosphere glovebox with moisture less than 1 ppm. 100 kDa pure PEO powder sample was transferred directly from the bottle into the NMR rotor. The annealing of this sample was performed in the NMR rotor by heating to 60 ºC and holding the temperature for 10 hours before cooling at 5 ºC increments, with the temperature held at each increment for 5 hours. 100 kDa pure PEO thin films casts were prepared with exactly the same method as the polymer electrolyte samples, except no LiTf was added. Polymer–salt solutions were prepared by dissolving weighed amounts of PEO and LiTf in dry acetonitrile and stirring for 24 hours to insure a homogeneous solution. To obtain the polymer electrolyte sample, the solutions were cast onto Teflon® sheets and the acetonitrile was allowed to evaporate in the glovebox for 48 hours. Samples were held under vacuum of 25 mmHg for 24 hours before use.

NMR experiments

All solid-state experiments were performed using a 3-channel Varian UnityInova NMR spectrometer (B_o = 7 T) with a 5 mm, 3-channel, magic angle spinning Varian APEX® probe. NMR samples were packed into zirconia pencil rotors inside a dry glovebox. Boron nitride spacers and plugs were used and sealed with epoxy to prevent contamination by atmospheric moisture. Drive and bearing gas were provided by dry, compressed air. The ^{13}C chemical shifts were referenced to an external standard of glycine (carbonyl resonance at 176.4 ppm). The sample temperature was maintained

at 25 ºC throughout NMR data collection. ^{13}C T_{IS} curves were collected with a typical cross polarization experiment with the duration of the contact time array between 0.01 and 8 ms. Data acquisition and processing was accomplished with VNMRJ (version 1.1D) provided by Varian Inc.

Results and Discussion:

The ^{13}C CPMAS NMR spectrum for PEO has broad and narrow NMR signals for the amorphous and crystalline regions, but these signals are superimposed and difficult to assign. Initially, Connor *et al*. noted that the ^{1}H spectrum for pure PEO consists of two superimposed NMR signals, one broad and one narrow peak.(*21*) Through proton spin-lattice relaxation experiments, it was observed that the broad component has a fast relaxation rate, while the narrow component has a slow relaxation rate. Conner *et al*. assigned the broad component to the amorphous region and the narrow component to the crystalline region. This assignment was made under the assumption that the amorphous region would have a larger CSA tensor, giving rise to a broad peak with a fast relaxation rate due to its higher degree of molecular motion. On the contrary, the crystalline region would have a smaller CSA tensor, producing a narrower peak with a slow relaxation rate due to the hampered molecular motion. Dechter reexamined pure PEO with CPMAS and observed that there were two superimposed NMR peaks for both the ^{1}H and the ^{13}C signals at short contact times.(*22*) The introduction of a

dipolar dephasing period prior to data collection resulted in the disappearance of the broad component. With this observation, Dechter assigned the broad component to the crystalline region under the assumption that the crystalline region would have a stronger dipole contact with the lattice and dephase quickly. Tegenfeldt *et. al*. reanalyzed the room temperature spectrum of pure PEO and performed a variable temperature study.(*23*) Tegenfeldt agreed with the room temperature assignment made by Dechter: that the component with fast relaxation is due to the crystalline component. However, Tegenfeldt stated that below 250 K, the relaxation rates for these two components change making the component with fast relaxation the amorphous region.

Our lab examines various PEO solid polymer electrolytes with REDOR to gain insight about the local structure around the lithium ions. Thus, it becomes crucial to know which signal represents either the crystalline or amorphous region. Upon collecting CPMAS data for the PEO:LiTf 20:1 at various contact times (T_{IS}), we observed the same behavior as previously reported for pure PEO samples (superimposed broad and narrow NMR signals). However, when we collected the same data for the PEO:LiTf 3:1 electrolyte, only the narrow peak was present at any contact time. This sample is crystalline with a published crystal structure,(*20*) which means the narrow signal assignment represents the crystalline phase. The assignment of the narrow signal in the PEO:LiTf 3:1 electrolyte is different than the previously accepted assignment for pure PEO. It is important to note that the 20:1 PEO:LiTf samples are composed of pure PEO and PEO:LiTf; thus, to

fully understand the assignments for the 20:1 PEO:LiTf, the pure PEO assignments must be taken into account. For dilute PEO:salt electrolytes, phase diagrams show the presence of only pure crystalline PEO and crystalline PEO:salt complexs,(*11*) but IR/RAMAN studies have shown the presence of an amorphous PEO:salt phase.(*5*) Thus, the pure amorphous PEO does not contribute to the NMR signals observed for the 20:1 PEO:LiTf electrolytes. We reinvestigated the NMR assignments of pure PEO, as they are imperative to fully understanding the NMR assignment of the 20:1 PEO:LiTf electrolytes.

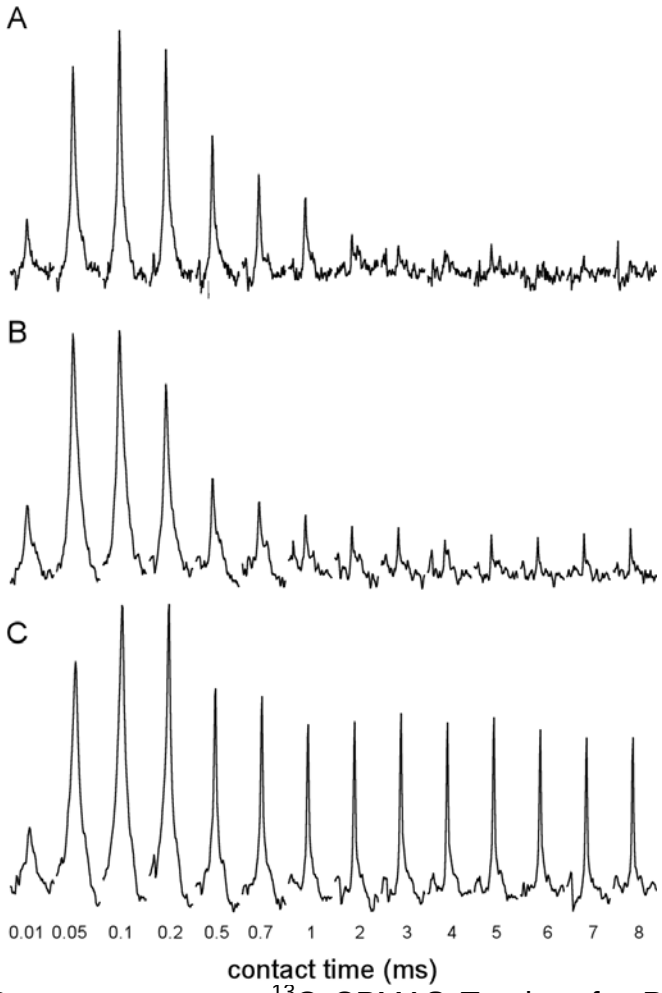

Figure 3.1. Room temperature ^{13}C CPMAS T_{IS} data for PEO powder (A), after heating to 60 ºC and slowly cooling to 25 ºC (B), and as a thin film cast from acetonitrile solution (C). The narrow signal from crystalline PEO is absent in the neat sample (A). After thermal annealing, a small narrow NMR signal is observed due to the formation of a crystalline fraction (B). Dissolution in acetonitrile increases polymer mobility and the polymer is allowed to precipitate with a large crystallization fraction (C). The narrow signal at a contact time of 8 ms has a chemical shift of 69.5 ppm with a linewidth of 135 Hz, and the broad signal (with narrow portion subtracted out) at a contact time of .1 ms has a chemical shift of 72 ppm with a linewidth of 974 Hz. All spectra are of 100 kDa PEO, Spinning rate = 5 kHz, recycle time = 10 s, 20 Hz line broadening, 256 scans.

All spectra in Figure 3.1 were taken under the same experimental parameters using 100 kDa PEO and, as expected, a single peak is seen for the polymer backbone (CH_2) groups. Figure 3.1A shows the T_{IS} (contact time array) data for powder PEO collected shortly after material was received from Sigma-Aldrich. In this T_{IS} data set, the broad component is primarily the only NMR signal observed. If the previously accepted assignments for pure PEO were correct then this would mean that the sample is almost completely crystalline, but this seems unlikely as X-ray crystallography is impossible.(*15*) Thermal annealing increases backbone mobility allowing for polymer reorientation (i.e. artificial aging increases crystallinity), while casting from acetonitrile increases the crystalline fraction. In the latter case, slow evaporation of the solvent occurs over two days, during which time the polymer slowly precipitates from solution and crystalline domains are easily formed. Both of these techniques increase the crystallization kinetics resulting in the growth of the crystalline region.(*4, 16, 18, 19*) However, the casting method significantly increases the growth of the crystalline phase due to uniform reorientation of the PEO backbone from increased mobility in solution. It is also well know that slow crystallization kinetics continue for months after sample preparation. It takes weeks to years to growth crystals large enough for X-ray diffraction.(*4, 16, 18*) Thus, the age and preparation techniques of the samples are very important as the sample spectra/properties will change over time.(*15-18*) With knowledge of how

thermal and casting treatments affect the crystallinity of the samples, we are able change the crystallinity and observe changes in the NMR signal.

Thermal annealing (temperature was held at 60 ºC for 10 hours then slowly lowered at a rate of 5 ºC every 5 hours until 25 ºC was reached) resulted in a new small narrow signal observed at contact times greater than 2 ms as shown in Figure 3.1B. As mentioned above, thermal annealing increases the amount of the crystalline region; thus we assign the appearance of the new NMR signal to the crystalline region. The casting process changes crystallization kinetics and should result in a significant growth of the crystalline regions.(*19*) Figure 3.1C reaffirms the assignment of the narrow NMR signal to the crystalline region, as we observe a substantial increase in the narrow NMR signal. Since these conditions cause notable increases of the narrow signal observed at contact times greater than 2 ms, we reassign the narrow NMR signal to the crystalline region and the broad NMR signal to the amorphous region. The broad NMR signal has a linewidth of 974 Hz and a chemical shift of 72 ppm, which agrees well with previously reported PEO spectra.(*27-29*) However, the narrow NMR signal has a linewidth of 135 Hz and a chemical shift of 69.5 ppm, which is shifted up field from previously observed 71 ppm.(*27-29*) The reason for the deviation of the narrow NMR signal from the previously reported values is not evident, but does not effect our assignments.

Although SPEs are chemically distinct from pure PEO, they also have amorphous and crystalline regions whose respective NMR signals have not

been assigned. Figures 3.2A, 3.2B and 3.2C show the T_{IS} (contact time array) data for the 2 kDa 3:1 PEO:LiTf (crystalline), 2 kDa 20:1 PEO:LiTf (crystalline and amorphous), and 100 kDa 20:1 PEO:LiTf (crystalline and amorphous) samples. The slight difference in the signal intensity between 2B and 2C is due the higher amount of pure crystalline PEO present in the 100 kDa PEO sample, as determined from REDOR dephasing curves (*vide infra* Figure 3.6). However, this difference does not affect the assignment of the amorphous and crystalline peaks; thus, the discussion below refers to both 20:1 PEO:LiTf samples.

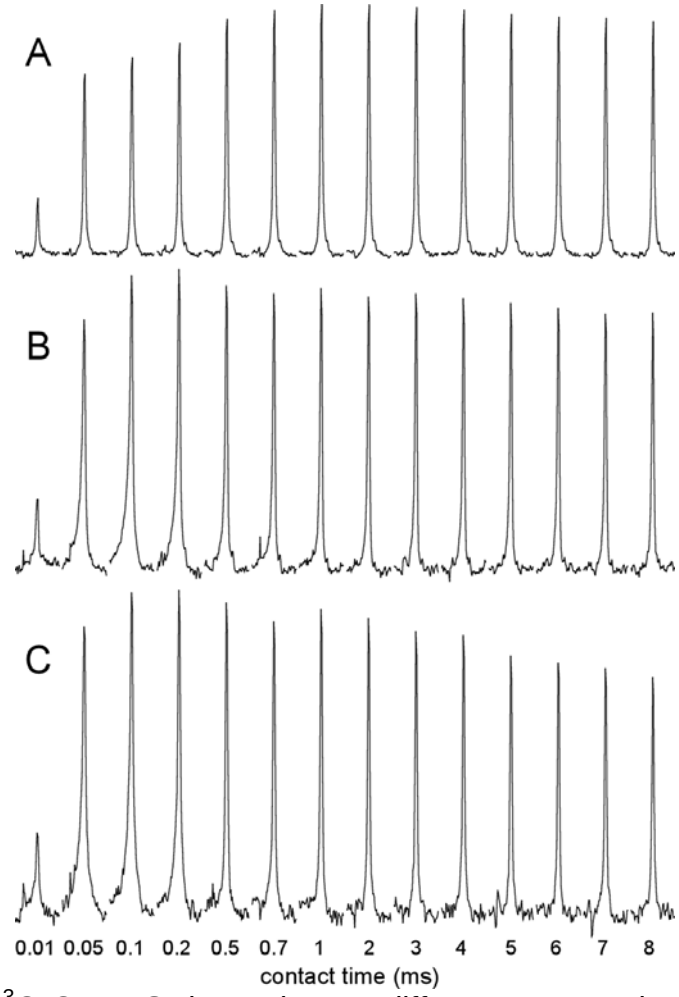

Figure 3.2. ^{13}C CPMAS data taken at different contact times to reflect the $^{1}H/^{13}C$ cross polarization dynamics (T_{IS}). The crystalline 3:1 PEO:LiTf sample shows a narrow line (chemical shift of 68.2 ppm and linewidth of 264 Hz) with a slower buildup and slower decay of the ^{13}C magnetization when compared with the more dilute 20:1 PEO:LiTf samples. Here, 20:1 PEO:LiTf formed with 2 kDa PEO shows narrow (chemical shift of 68.2 ppm and linewidth of 270 Hz) and broad (chemical shift of 70.7 ppm and linewidth of 1042 Hz) at short contact times (B). Only the narrow component survives at longer contact times. When 20:1 PEO:LiTf is created with 100 kDa PEO, both components are seen with the chemical shifts and linewidths (C) yet decay of the narrow ^{13}C signal is faster than the other samples. This behavior is caused by the presence of crystalline pure PEO domains in addition to crystalline PEO:LiTf. Spinning rate = 5kHz, recycle time =10 s, line broadening = 20 Hz, scans = 256.

All spectra in Figure 3.2 were taken under the same experimental parameters and, as expected, a single peak is seen for the polymer backbone

(CH_2) groups. The T_{1S} data for the crystalline 2 kDa 3:1 electrolyte contains only the narrow component; therefore, we assigned the narrow component to the crystalline region. This NMR signal has a linewidth of 264 Hz and a chemical shift of 68.2 ppm, which is close to the previously report chemical shift of 68.9 ppm.(*25, 26*) The 20:1 samples are heterogeneous and their NMR signals consist of a broad component and a narrow component at short contact times (0.1 ms). However, at longer contact times (8 ms) only the narrow component is present, which has the same linewidth and chemical shift as the 3:1 sample. Thus, by comparing the signal shape and linewidth of the crystalline 3:1 sample, and from our reanalysis of pure PEO, we have assigned the narrow component to the crystalline phases and the broad component to the amorphous phase. The broad NMR signal has a linewidth of 1042 Hz and chemical shift of 70.7 ppm. To our knowledge, this is the first in-depth assignment of the broad NMR signal for the 20:1 PEO:LiTf sample, but it follows the same trend as the pure PEO samples. The upfield shifts observed for both PEO:LiTf NMR signals, from that of pure PEO, is due to the increased shielding of the carbons caused by the strong interaction of the lithium ion with the PEO backbone.(*25, 26*) As judged from the phase diagrams and IR/RAMAN studies, the amorphous pure PEO is not present(*5, 11*) thus, the broad component only represents the amorphous PEO:LiTf.

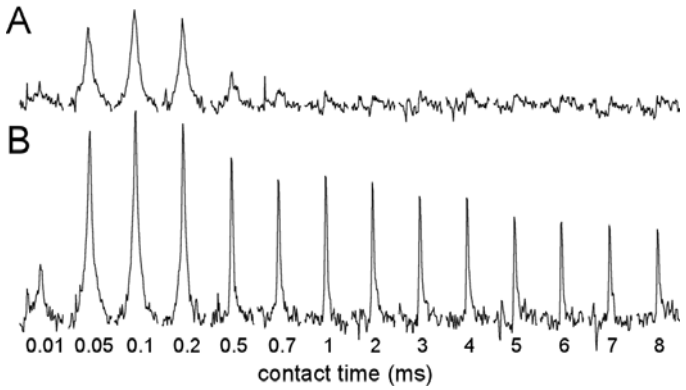

Figure 3.3. Shows the resulting T_{IS} curves from the spectral subtraction of 3:1 PEO:LiTf and 2 kDa 20:1 PEO:LiTf (3.3 A), and 3:1 PEO:LiTf and 100 kDa 20:1 PEO:LiTf (3.3 B). The heterogeneous 20:1 PEO:LiTf samples have different domains: crystalline 3:1 PEO:LiTf, amorphous PEO:LiTf, and crystalline pure PEO. The T_{IS} data for 3:1 PEO:LiTf serves as a baseline to understand the other domains. Spectral subtraction of data in Figure 3.2 A (crystalline PEO:LiTf) from 2 B (crystalline and amorphous PEO:LiTf) results in a set of T_{IS} data for the amorphous PEO:LiTf domains in 2 kDa PEO (3.3 A). The apparent $T_{1\rho}$ for the amorphous PEO:LiTf is 0.45 ms. Spectral subtraction with the 100 kDa PEO data set reveals the presence of a narrow component with a chemical shift of 69.5 ppm and linewidth of 152 Hz (3.3 B). These data have been scaled to take into account the amount of pure crystalline PEO material determined from the $^{13}C\{^{7}Li\}$ REDOR dephasing curves.

As observed in Figure 3.2, the 3:1 and 20:1 electrolytes have different T_{IS} data. Due to the lack of molecular motion in the crystalline 3:1 sample, it is not surprising that the ^{13}C retains its magnetization for a long period of time, resulting in a strong signal at long contact times. The 20:1 sample has a different and more complex $T_{1\rho}$ behavior due to the presence of crystalline (PEO:LiTf and pure PEO) and amorphous (PEO:LiTf) phases, which have very different dynamics. Dynamic data can be acquired from the heterogeneous 20:1 samples by subtracting the T_{IS} curve of the 3:1 sample as shown in Figure 3.3. Subtracting the 3:1 T_{IS} curve removes the contributions of the crystalline PEO:LiTf region and leaves behind the

contributions of the amorphous PEO:LiTf and pure crystalline PEO regions. This results in the T_{IS} data for a broad component (amorphous PEO:LiTf) and a narrow component (pure crystalline PEO). Since the two different molecular weight samples have different factions of pure crystalline PEO, REDOR data were taken to determine their ratios and the appropriate scaling factors (Figure 3.6). A crystalline signal at long contact time (> 2 ms) is not seen in Figure 3.3A due to the small amount of pure crystalline PEO present. The broad component in Figures 3.3A is due to the amorphous PEO:LiTf region in the 20:1 sample composed of 2 kDa PEO. The ^{13}C magnetization is lost within 1 ms, suggesting a higher degree of molecular motion. Because the amorphous region is responsible for the transport of the lithium ions, a higher degree of molecular motion is not unexpected. The difference spectrum of 20:1 PEO:LiTf composed of 100 kDa PEO shown in Figure 3.3B has both a broad component and a narrow component. The broad line represents the amorphous PEO:LiTf region and the narrow line represents the pure crystalline PEO (this has the same linewidth and chemical shift as seen in pure PEO suggesting the absence of any lithium ion interactions, otherwise there would be chemical shift change from the increased shielding of the lithium ion). The amorphous region is the most interesting, as it is responsible for ionic conductivity, yet it cannot be directly studied using X-ray crystallography, IR/RAMAN, DSC, or complex impedance.(*15*) However, the amorphous region can be investigated with NMR. Previous variable temperature (VT) NMR studies have focused on understanding the dynamics

of the crystalline and amorphous regions.(*24, 30, 31*) However, these studies have used the assignment previously given to pure PEO and need to be reanalyzed in light of our new assignments. The ability to obtain $T_{1\rho}$ data for the amorphous region provides the opportunity to describe PEO chain dynamics as a function of temperature. $T_{1\rho}$ values are obviously different, estimated to be 0.45 ms for the amorphous regions, 64.5 ms for the 3:1 PEO:LiTf, and 14 ms for the 100 kDa pure crystalline PEO. The fastest $T_{1\rho}$ rate is for the amorphous domains, whereas the crystalline PEO:LiTf domains are the most rigid. Compared to the pure crystalline PEO, the salt serves to quench motion in the crystalline phase, presumably by locking neighboring PEO chains into a helix around the lithium cation.(*20*)

Conclusions:

Researchers have been working for the last 30 years to improve the ionic conductivity of solid polymer electrolytes. In order to do this, it is crucial to thoroughly understand these systems and their different phases. However, there is currently no technique, other than NMR, capable of directly observing the amorphous phases. Since NMR is able to observe both crystalline and amorphous phases, it is necessary to accurately assign the portion of the NMR signal that represents these regions.

We have revised the previous assignments for pure PEO and, for the first time, assigned the NMR signals for the PEO:LiTf solid polymer

electrolytes. For both the pure PEO and the 20:1 PEO:LiTf samples we assign the broad component to the amorphous region and the narrow component to the crystalline regions. Our reassignment of pure PEO is reversed from the previously accepted assignment as is our new assignment for PEO:salt electrolytes. However, all NMR studies of PEO electrolytes to date have used the previous assignments given to pure PEO. Thus, all current understanding of electrolyte polymer backbone dynamics gained from NMR must be reanalyzed using the correct assignments.

Section 2: Local Lithium Structure of PEO Lithium Electrolytes

Introduction:

For PEO:Li salt systems, impedance measurements can be used to evaluate ion transport,(*32*) but these measurements do not provide fundamental chemical insight into the PEO-to-lithium chemical structure. Low temperature X-ray crystallography data of crystalline PEO electrolytes revealed a PEO helix around a central core of lithium cations.(*20*) Triflate anions, $CF_3SO_3^-$, participate in lithium coordination by forming bridges between two lithium cations. However, the use of X-ray crystallography requires a high degree of order that is not present in the dilute PEO electrolytes.(*15*)

Dilute PEO electrolytes are heterogeneous at room temperature, consisting of a pure PEO phase, a crystalline PEO-salt phase, and an amorphous phase containing some dissolved salt.(*3, 9-11, 33*) It has been observed in numerous PEO:salt systems that ionic conductivity occurs mainly in the amorphous phase.(*3*) Heating the polymer near 100 ºC significantly increases conductivity, attributed to a melting of the crystalline phase.(*5*) Thus, there have been various efforts made to reduce the amount of the crystalline phase at room temperature, thereby increasing conductivity by using plasticizers and copolymers.(*1*) These efforts would benefit from the ability to characterize how the lithium environment changes with different

plasticizers and copolymers. This would provide a means to identify the interactions that prevent lithium mobility, and also identify the best method to encourage lithium mobility.

X-ray crystallography cannot be employed to study dilute polymer electrolytes because the reduction in crystallinity destroys the long-range structural order necessary for diffraction,(*15*) but solid-state NMR is ideally suited to provide structural data for the heterogeneous domains within dilute polymer electrolytes. Previously, a variety of solid-state NMR experiments have been conducted, but these experiments cannot provide the detailed structural information available from REDOR data. This has been demonstrated by the recent REDOR study of a crystalline 6:1 PEO:$LiPF_6$ sample,(*34*) which agreed with the previously published X-ray structure.

We use $^{13}C\{^{7}Li\}$ (REDOR) experiment to study the PEO lithium triflate (PEO:LiTf) solid polymer electrolyte system. The dilute PEO:LiTf systems are composed of two regions that contain lithium triflate; the crystalline and amorphous regions. Although the amorphous region is thought to be responsible for this systems conductivity, it is quite difficult to isolate the amorphous NMR signal from the crystalline NMR signal.(*34*) However, it is relatively easy to isolate the crystalline NMR signal by using contact time editing. Understanding the structure of these crystalline microdomains is vital in order to develop methods to liberate the lithium cations trapped within them. Here, $^{13}C\{^{7}Li\}$ REDOR NMR data was collected for the crystalline 3:1 PEO:LiTf and the crystalline microdomains for the 20:1 PEO:LiTf. Our data

clearly demonstrates that the lithium crystalline microdomains are nearly identical to those of a crystalline 3:1 sample, for which the crystal structure is known. $^{13}C\{^{7}Li\}$ REDOR data was also used to quantify the ratio between the amount of pure crystalline PEO and crystalline PEO:LiTf within 2 kDa and 100 kDa PEO electrolytes. In addition, we also identify the inability to characterize the lithium environment of the amorphous region with REDOR NMR experiments at ambient temperature.

Experimental:

NMR experiments

All solid-state experiments were performed using a 3-channel Varian UnityInova NMR spectrometer (B_o = 7 T) with a 5 mm, 3-channel, magic angle spinning Varian APEX® probe. NMR samples were packed in Zirconia pencil rotors inside a dry glovebox. Boron nitride spacer and plug were used and sealed with epoxy to prevent contamination by atmospheric moisture. Drive and bearing gas were provided by dry, compressed air. The ^{13}C chemical shifts were referenced to an external standard of glycine (carbonyl resonance at 176.4 ppm). The sample temperature was maintained at 25 ºC throughout NMR data collection. Data acquisition and processing was accomplished with VNMRJ (version 1.1D) provided by Varian Inc.

REDOR data were collected using a sample spinning rate of 5000 Hz, cross-polarization contact time of 8000 μs, and ^{1}H decoupling at an rf power level of 50 kHz. The rf power for the ^{13}C and ^{7}Li channels was 50 and 86 kHz, respectively. The XY-8 phase cycling scheme was used on both the ^{13}C and ^{7}Li channels.(*35*) S_o and S_r spectra were recorded at 2,4,6,8…40 rotor cycles. Each spectrum was collected with 256 scans and a 20 s recycle time (^{1}H T_1 = 7 sec). Each ^{13}C{^{7}Li} REDOR data point was divided by 0.93 to scale for the natural abundance of ^{7}Li.

Dipolar coupling constants were determined using the following method. Computer simulations with the SIMPSON(*36*) program were used to create a theoretical REDOR dephasing curve. Simulations involving one ^{13}C and one ^{7}Li were compared to the first four data points to determine the primary lithium-carbon dipolar-coupling constant. From this dipolar-coupling constant the average primary Li-C distances were calculated using eq. 3.1.

$$D = (\mu_o \hbar/4\pi)(\gamma^I \gamma^S/r^3) \qquad (3.1)$$

D from the equation above is the dipolar-coupling constant, μ_o is the permittivity of free space, γ^I is the magnetogyric ratio of the dephasing nuclei (^{7}Li), γ^S is the magnetogyric ratio of the observe nuclei (^{13}C), and r is the internuclear distance.

Fitting procedure

From the reported PEO_3:LiTf crystal structure(*20*), the distance from any carbon to the closest (primary) lithium varies from 2.55 to 3.40 Å, and from any carbon to the second closest (secondary) lithium, the distance varies from 4.0 to 7.4 Å, thus a ^{13}C nucleus may be dephased by two ^{7}Li nuclei at different distances. Lithium cations beyond 7.5 Å do not have a significant contribution to the dipolar dephasing. At short dephasing times (0-2.5 ms), ^{13}C signal loss is caused by the primary lithium due to its much larger dipolar coupling, whereas the secondary lithium does not have a significant effect until dephasing times of 3-8 ms.

Dipolar coupling constants were determined using the following method. Computer simulations with the SIMPSON(*36*) program were used to create a theoretical REDOR dephasing curve. Simulations involving one ^{13}C and one ^{7}Li were compared to the first four data points to determine the primary lithium-carbon dipolar-coupling constant. This primary dipolar-coupling constant was used in subsequent 3-spin (^{13}C, ^{7}Li, ^{7}Li) simulations, which varied the secondary dipolar-coupling constant.

Results and Discussions:

Figures 3.4A and 3.4B show the ^{13}C CPMAS spectra for 3:1 and 20:1 PEO:LiTf. As expected, single peaks are seen for the polymer backbone (CH_2) and the triflate (CF_3) groups. These spectra were taken under the same experimental parameters; however, the 20:1 sample has a much lower signal-to-noise ratio. This arises because only a small fraction of the sample

is solid on the NMR timescale (motions slower than kHz). Solid-state NMR uses cross-polarization to selectively observe the solid-fraction.(*26, 37-39*) Because the cross-polarization dynamics in the 20:1 sample are similar to those in the highly crystalline 3:1 sample, the signal in Figure 3.4 B is assigned to the microcrystalline domains within the heterogeneous 20:1 polymer electrolyte sample.

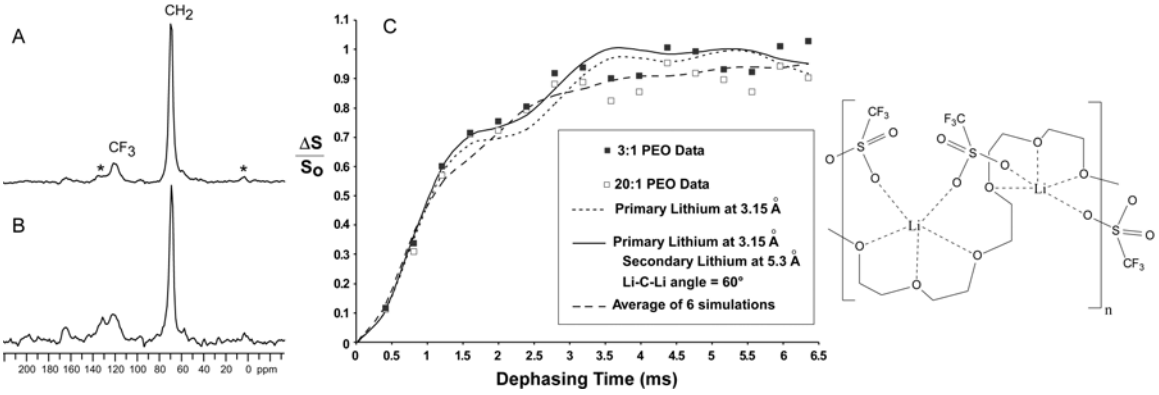

Figure 3.4. Shows the ^{13}C CPMAS spectra for the 2 kDa 3:1 and 20:1 PEO:LiTf and the $^{13}C\{^{7}Li\}$ REDOR dephasing curve for the 2 kDa 3:1 and 20:1 PEO:LiTf. (A) ^{13}C CPMAS of 2000 MW PEO lithium triflate O:Li = 3:1, (B) ^{13}C CPMAS of 2000 MW PEO lithium triflate O:Li = 20:1. B_0 = 7 T, contact time = 8 ms, spinning rate = 5 kHz, recycle time = 20 s, line broadening = 100 Hz, linewidth = 330 Hz, scans = 256 for A and B. (C) $^{13}C\{^{7}Li\}$ REDOR dephasing curve for 3:1 PEO:LiTf and 20:1 PEO:LiTf signal.

REDOR dephasing curves for 3:1 and 20:1 PEO:LiTf are shown in Figure 3.4C. It is easy to see that these data points do not have the typical shape of the universal REDOR curve. This is because the universal REDOR curve is generated with spin $^{1}/_{2}$ - $^{1}/_{2}$ systems whereas our $^{13}C\{^{7}Li\}$ is a spin $^{1}/_{2}$ - $^{3}/_{2}$ system. Thus, we used the SIMPSON program to simulate the REDOR dephasing curve that would arise from a spin $^{1}/_{2}$ - $^{3}/_{2}$ systems. Gullion et al

has recently used this simulation program on a similar system. Through the use of SIMPSON simulations and by comparison to Gullion's paper it is apparent that our REDOR dephasing curve has the correct shape and intensity that is expected from the full excitation of the ^{7}Li spins during the REDOR experiment.

In Figure 3.4C, the dashed line represents a SIMPSON simulation with a single lithium dipolar coupling constant of 394 Hz, the solid line represents a single lithium dipolar coupling constant of 375 Hz, and the dotted line represents a single lithium dipolar coupling constant of 358 Hz. These dipolar coupling constants correspond to Li-C distances of 3.10, 3.15 and 3.20 Å. These simulations demonstrate that a distance difference of .05 Å yields an easily distinguishable slope change. With these different dephasing curves we assign the best fit to that which corresponds to 375 Hz or a Li-C distance of 3.15 Å. This value is 10% longer than the average Li-C distance from the PEO_3:LiTf crystal structure published by Lightfoot et. al.,(*20*) which is expected for distances obtained from REDOR. It is well established that distances obtained from REDOR measurements are longer than those obtained from X-ray diffraction,(*40-42*) due to the effects of vibrational and librational motion on the dipolar interaction.(*41*) These simulations demonstrate that our REDOR data reflect the carbon-lithium environment, as shown previously for PEO:$LiPF_6$.(*34*)

The REDOR dephasing data for PEO:LiTf (20:1) are essentially identical to the 3:1 data in the region of 0-2.5 ms. Beyond 3 ms, the 20:1 data

points are slightly lower than the 3:1 data points, yet retain the same sinusoidal shape. The REDOR dephasing curve arises due to the dipolar interaction from the lithium cation. Thus, it is expected in a dilute PEO:LiTf system, such as the 20:1, that the observed REDOR dephasing curve may be less intense due to the small amount of crystalline PEO that does not contain lithium triflate. The REDOR dephasing curve for the 20:1 PEO:LiTf rises to a value of .95 ($\Delta S/S_o$), rather than the expected 1. This is caused by crystalline, lithium free, PEO segments that contribute to the S_o signal, but not the S_r signal. Thus, we can estimate that 5% of the crystalline segments do not have lithium near by. Such a chemical environment could arise at the edges of the crystalline microdomains. Both the 3:1 and 20:1 REDOR dephasing curve are slightly less intense than the simulated curves form the SIMPSON program. This is most likely due to the effects of multiple weaker dipolar interactions from secondary, and tertiary lithium ions. Strikingly, the initial slope of the dephasing curves for 3:1 and 20:1 PEO:LiTf samples indicate that the average primary Li-C distances must be very similar. This can only occur if the 20:1 and 3:1 PEO:LiTf samples have nearly identical local structures inside their respective crystalline fractions. Likewise, the data show that the distributions of secondary and tertiary lithium atoms are quite similar for the two samples. Thus, the molecular architecture within the microcrystalline domain of 20:1 is almost certainly a helix, the known structure of the 3:1 compound.

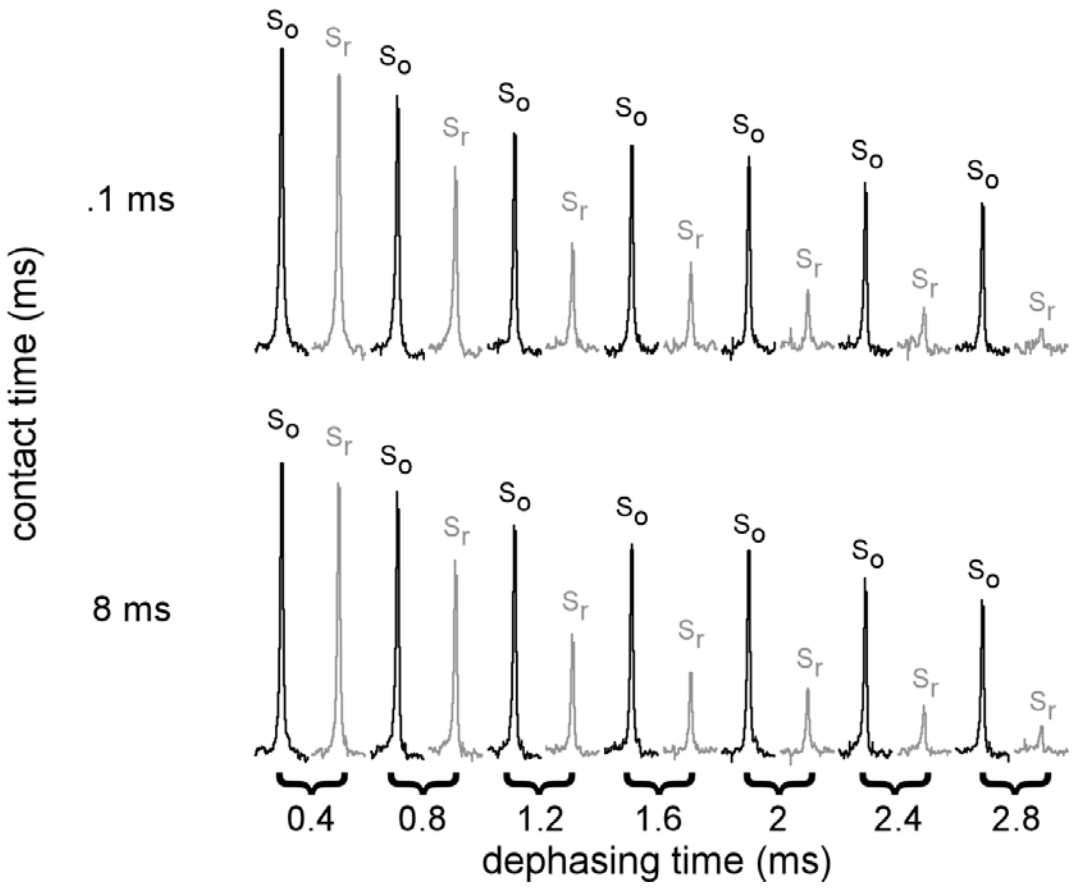

Figure 3.5. Comparison of the 2 kDa 20:1 PEO lithium triflate $^{13}C\{^{7}Li\}$ REDOR data collected at contact times of 0.1 and 8 ms. The expected narrow component in the 0.1 ms data is absent, presumably due to fast T_2 relaxation. Spinning rate = 5 kHz, recycle time =10 s, line broadening = 100 Hz, scans = 256

The amorphous region is the most interesting, as it is responsible for ionic conductivity, yet it cannot be directly studied using X-ray crystallography, IR/RAMAN, DSC, or complex impedance.(*15*) With the ability to separate the NMR signals for the amorphous and crystalline regions, it becomes possible to study the local lithium environment for these regions. Characterization of the crystalline region using REDOR has already be achieved.(*43*) However, it

is also necessary to understand the structure of the amorphous region in order to improve ionic conductivity within SPE's.(*34, 43*) With this in mind, we collected REDOR data at a contact time of 0.1 ms. From the ^{13}C CPMAS data in Figure 3.2, the signal at 0.1 ms is composed of both the crystalline and amorphous regions, suggesting the possibility to obtain a REDOR dephasing curve for the broad (amorphous) component by a spectral subtraction of the REDOR data at contact times of 0.1 and 8 ms. Figure 3.5 shows the S_o and S_r REDOR NMR signals for a contact time of 0.1 and 8 ms. Upon inspection of these two data sets, it is observed that they have only the narrow component, while the broad component is absent. The reason the broad component is missing is not fully understood, but is most likely due to fast T_2 relaxation. With pure PEO, Dechter observed the disappearance of the broad component when a 2 ms dephasing period was introduced prior to data collection.(*22*) Dechter attributed this to the dipolar interactions completely dephasing the signal; however, in our sample the T_2 relaxation rate of this sample is too fast to measure ^{13}C-^{7}Li dipolar coupling. Therefore, it is not possible to obtain detailed information about the local lithium environment for the amorphous region using REDOR at ambient temperature. However, it may be possible to collect REDOR information for the amorphous region at temperatures below its glass transition (-60 ºC).

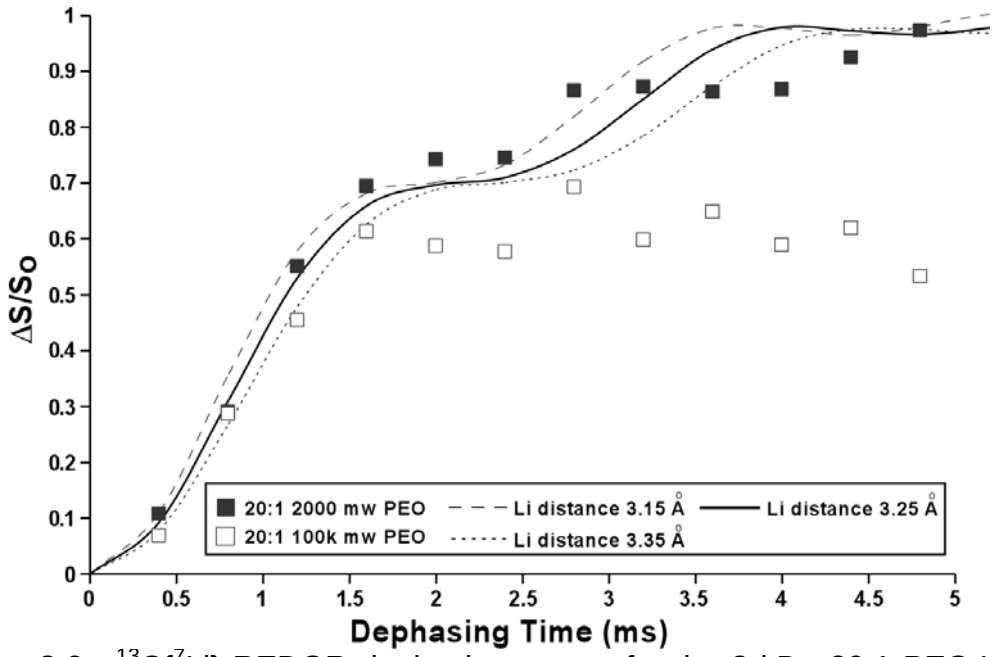

Figure 3.6. $^{13}C\{^{7}Li\}$ REDOR dephasing curves for the 2 kDa 20:1 PEO:LiTf and the 100 kDa 20:1 PEO:LiTf. The dephasing curves do not reach unity as pure PEO is present in the dilute, heterogeneous, SPE samples. Simulations of the dephasing curves (solid, dashed, and dotted lines) were performed with the SIMPSON program. The accuracy of the simulation is reduced past 3 ms due to the inability to perform simulations with 4 spins or more. Spinning rate = 5kHz, contact time = 8 ms, recycle time =10 s, line broadening = 100 Hz, scans = 256

Although we are unable to collect REDOR data for the amorphous PEO:LiTf region, we can and have collected REDOR for the crystalline PEO:LiTf region. Figure 3.6 shows the REDOR dephasing curves for the 2 kDa and 100 kDa samples of 20:1 PEO:LiTf collected at 25 ºC. These curves have the same basic shape. Beyond 1 ms, the 100 kDa data points are 25% lower in intensity than the 2 kDa data points, yet retain the same sinusoidal shape. Due to the similarity in the initial part of the dephasing curve and both samples sharing the similar sinusoidal dephasing curve, we believe that the local lithium environment of the 100 kDa 20:1 PEO:LiTf sample is essentially the same as the previously reported REDOR structure of the 2 kDa 20:1

PEO:LiTf sample.(*43*) The presence of crystalline pure PEO will contribute to the S_o signal, but not the S_r signal. This causes the dephasing curve to rise to a value corresponding to the fraction of crystalline PEO:LiTf present rather than unity. As seen in Figure 3.6, the REDOR dephasing curve for the 2 kDa rises to a value of 0.95 ($\Delta S/S_o$), rather than the expected 1. Thus, 5% of the crystalline material is pure crystalline PEO and does not have lithium nearby. However, the 100 kDa rises to a value of 0.7 ($\Delta S/S_o$), rather than 1. Thus, 30% of the crystalline material is pure crystalline PEO and does not have lithium nearby. It is expected that increasing the molecular weight of the polymer system, such as the 100 kDa PEO, would enable a larger amount of pure crystalline PEO to form resulting in the reduced intensity of the REDOR dephasing curve. Such a chemical environment could arise with increased polymer length by allowing for better polymer packing permitting larger sections of the polymer to form crystalline domains. These crystalline, lithium free, PEO segments contribute to the S_o signal, but not the S_r signal resulting in a decrease in the dephasing curve as observed in Figure 3.6.

We also note that the intensity of the REDOR curve is a direct and quantitative measurement of the percentage of dephasers present. Thus, the REDOR dephasing curve maximum directly measures the percentage of crystalline PEO:LiTf. Phase diagrams and IR/RAMAN studies have shown the absence of the pure amorphous PEO phase,(*5, 11*) therefore the difference in dephasing curve intensities is due to the pure crystalline PEO. Thus, the REDOR data for the 100 kDa 20:1 PEO:LiTf in Figure 3.6 verifies

our observation that the pure crystalline PEO gives a narrow peak (as shown in Figures 3.1 & 3.3B).

Conclusions:

In the last decade, a great deal of understanding and information has been gained for the crystalline SPE through the use of X-ray crystallography.(*15, 20, 44-49*) However, this information has been missing for the dilute PEO:salt electrolytes. The use of REDOR has been a valuable tool for measuring molecular structures of non-refractive materials, including solid polymer electrolytes. It has been demonstrated by Rhodes and Frech that X-ray data for the 20:1 PEO:LiTf contains no diffraction peaks for the crystalline region.(*5, 15*) We show that not only is it possible to observe the crystalline region of 20:1 sample with solid-state NMR, but that REDOR data gives structural information for the microcrystalline domain. The lithium environment in the microcrystalline domains of 20:1 PEO:LiTf is indistinguishable from the much larger crystal regions of 3:1 PEO:LiTf, for which a crystal structure is known. Rhodes and Frech also concluded that the structure of the microcrystalline domains of 10:1 and 20:1 PEO:LiTf samples is similar to the structure of the 3:1 PEO:LiTf, based on inferences made from IR/RAMAN studies.(*15*)

The presence of a crystalline region in 20:1 PEO:LiTf is consistent with published phase diagrams(*11*) and information that has been inferred from

vibrational spectroscopy studies of the 10:1 PEO:LiTf samples.(*15*) Our investigation has primarily focused on the structure of the lithium-PEO backbone interactions. However, this only provides half of the information needed to describe the lithium containing microcrystalline domains within the 20:1 PEO:LiTf sample. The other important interactions are those between the lithium cations and triflate anions. Rhodes and Frech provide this information form detailed analysis of vibrational spectroscopy data.(*15*) In a series of elegant experiments, they show that the lithium-triflate interactions in the microcrystalline domains of the 20:1 and 10:1 PEO:LiTf samples are similar to that of the 3:1 PEO:LiTf sample. These data are the first structural information for ions within the microcrystalline domain, an important discovery that impacts the ability of the Li^+ and Tf^- to separate during ion conduction within the polymer network.(*15*) From the combination of these separate investigations, it can be stated that the PEO/lithium/triflate structure of the microcrystalline domains in the 20:1 PEO:LiTf samples have the same structure as the crystalline 3:1 PEO:LiTf sample.

Using REDOR to understand the microscopic structure of solid polymer electrolytes is a first step towards future improvements of both conductivity and material properties. Such structural information identifies the molecular interactions that retard lithium ion mobility, providing chemical targets to increase conductivity. Likewise, REDOR will prove a powerful tool to evaluate molecular-level engineering strategies aimed towards alleviating crystalline domains.

Additionally, we have demonstrated that the higher molecular weight PEO electrolyte contains a larger amount of pure crystalline PEO than the lower molecular weight PEO electrolyte. Unfortunately, we have also revealed the inability to collect REDOR data for the amorphous region at ambient temperature. However, there is a wealth of dynamic information that can now be obtained for both the amorphous and crystalline regions.

Section 3: Dynamics of the PEO Backbone in Lithium Electrolytes.

Introduction:

It has been well established that the lithium containing amorphous region in PEO:LiTf electrolytes is responsible for the observed ionic conductivity.(*3*) Lithium ion migration is facilitated by the segmental motion of the polymer backbone that is present in the amorphous region. Thus, increasing segmental motion either through manipulation of the electrolyte material or by variation of the operating temperature is well documented. Numerous studies have correlated the linewidth of static ^{7}Li spectra with the mobility of the lithium ions (or ionic conductivity), which have either been used to evaluate the conductivity properties of the electrolyte or the dependence of ionic conductivity as a function of temperature.(*50-58*) However, there has been limited mobility data collected for the PEO backbone with ^{13}C NMR studies. This area has also been hampered by the incorrect assignment of the NMR signals made by previous researchers as discussed in section 1 of this chapter. In this section, we use REDOR, T_{IS} curves, and static ^{7}Li NMR experiments observe dynamical changes in the PEO backbone at various temperatures.

Experimental:

NMR Experiments

All solid-state experiments were performed using a 3-channel Varian UnityInova NMR spectrometer (B_o = 7 T) with a 5 mm, 3-channel, magic angle spinning Varian APEX® probe. NMR samples were packed into zirconia pencil rotors inside a glovebox. Boron nitride spacers and plugs were used and sealed with epoxy to prevent contamination by atmospheric moisture. Drive and bearing gas were provided by dry, compressed air. The ^{13}C chemical shifts were referenced to an external standard of glycine (carbonyl resonance at 176.4 ppm). The sample temperatures ranged from 25 – 100 ºC throughout NMR data collection. Data acquisition and processing was accomplished with VNMRJ (version 1.1D) provided by Varian Inc.

^{13}C T_{IS} and REDOR data were collected for temperatures between 25 and 70 ºC at 5 ºC increments using the same contact times and parameters described in sections 1 & 2 of this chapter.

Static ^{7}Li linewidth data were collected using a typical block decay pulse sequence with proton decoupling, a recycle time of 10 s, a temperature range of 25 to 100 ºC at 5 ºC increments, and 64 scans. The linewidth of each spectrum was measure and plotted vs. temperature to reveal the

correlation between lithium ion mobility, PEO backbone mobility, and temperature.

Results and Discussions:

Understanding any structural changes between the PEO backbone and the lithium ions at different temperatures may improve our understanding of the mechanism for ionic conductivity. Thus, REDOR experiments were collected at temperature ranging from 45 to 75 ºC at 5 ºC increments in an effort to obverse if any profound structural changes occur. Variable temperature $T_{1\rho}$ experiments were also collected at temperatures ranging from 25 to 75 ºC in 5 ºC increments in an effort to obverse and understand the changes in molecular motions and melts of the different regions for the 20:1 sample. It is well understood that the room temperature 20:1 sample consists of three different regions: 1) crystalline pure PEO, 2) lithium containing crystalline PEO region (thought to be a 3:1 complex), and 3) lithium containing amorphous PEO region (structure unknown). Of these 3 regions only 2 are depicted in current phase diagrams: the crystalline pure PEO and the lithium contain crystalline PEO. Thus, DSC measurements only show the T_g of the lithium containing amorphous PEO (-60 ºC), the T_m's of the crystalline pure PEO (65 ºC) and the lithium containing crystalline PEO (118 ºC). Very little is known about the effects of temperature for the lithium containing amorphous region at temperatures above T_g. Variable

temperature $T_{1\rho}$ experiments show the melts of regions as well as their changes in mobility, while variable temperature REDOR experiments provide information on structural changes, local lithium mobility changes, and also changes in the amount of lithium in the microcrystalline region if any occur.

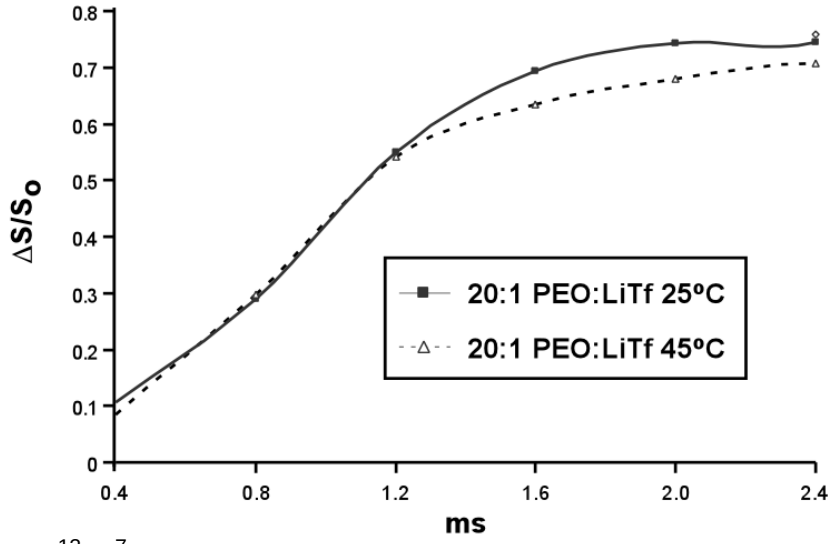

Figure 3.7. $^{13}C\{^{7}Li\}$ REDOR dephasing curves for the 100 kDa 20:1 PEO lithium triflate at 25 and 45 ºC. The dephasing curves are very similar with a smaller intensity observed for the dephasing curve collected at 45 ºC. This is most likely due to added motion slightly weakening the dipolar interaction between ^{7}Li and ^{13}C. Spinning rate = 5kHz, contact time = 8 ms, recycle time =10 s, line broadening = 100 Hz, scans = 256

Figure 3.7 shows the REDOR dephasing curves collected at 25, 45, and 55 ºC. There is only a slightly different between these REDOR dephasing curves, thus we conclude there is no significant change in the microcrystalline structure about the lithium ion at temperature between 25 to 55 ºC. However, it was not possible to collect REDOR dephasing curves at temperatures above 55 ºC (data not shown). This means that the dipolar interactions between the ^{7}Li and ^{13}C have been destroyed. There are four possible reasons for this 1) there is too much vibrational motion of the lithium-

oxygen coordination bonds, 2) there is too much librational motion in the PEO backbone, 3) there is too much through space motion due to the melting of the other domains, or 4) the sample has melted and all lithium is now in liquid PEO phase. We can rule out the latter possibility due to the ability to observe a PEO signal at temperatures above 70 ºC, but any of the other three is possible. In order to better understand these possible mobility issues it is necessary to collect $T_{1\rho}$ data at these temperatures.

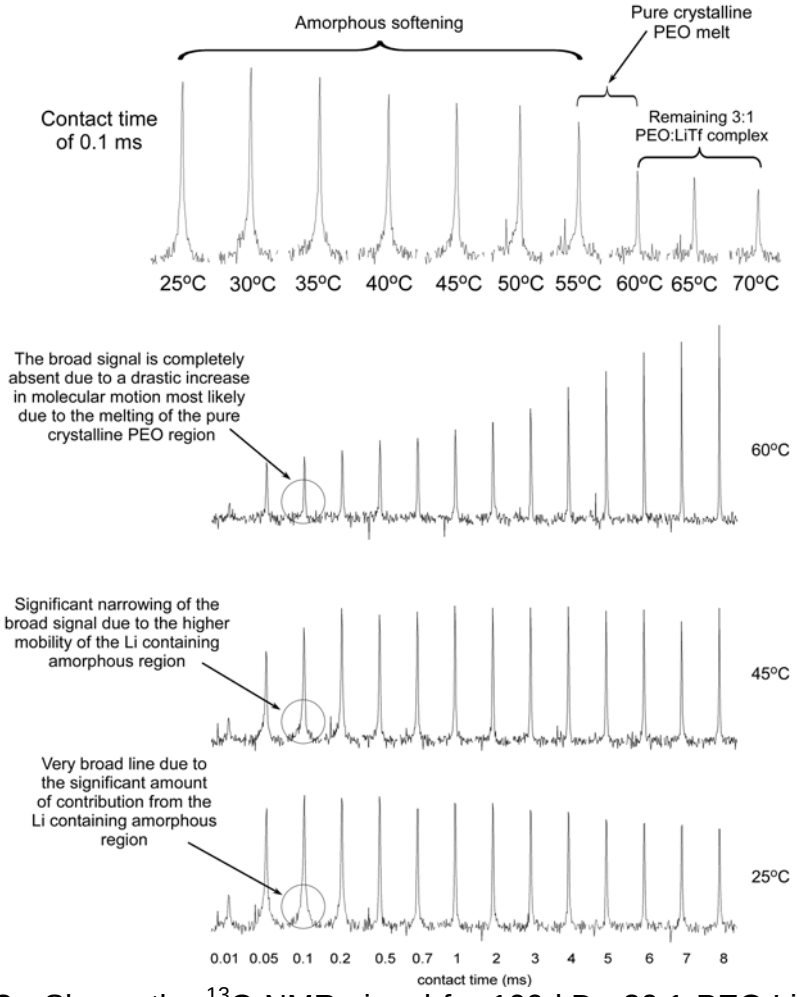

Figure 3.8. Shows the ^{13}C NMR signal for 100 kDa 20:1 PEO:LiTf collected at a contact time of 0.1 ms and variable temperature (25 – 70 ºC in 5 ºC intervals) (top portion), and the ^{13}C TIS curves at temperature of 25, 45, and 60 ºC (bottom portion). Changes in the NMR signal during the variable temperature array show the softening of the amorphous region (25 – 45 ºC) as observed by the disappearance of the broad component, and the melting of the pure crystalline PEO (55 – 60 ºC) as observed by the narrowing and loss of signal intensity. Below this portion of the Figure is shown the T_{IS} curves for 25, 45 (softening of amorphous region), and 60 ºC (melting of pure crystalline PEO). The changes in the morphology of the sample can be followed by the changes between these three T_{IS} curves. The T_{IS} curve at 25 ºC exhibits a higher intensity at 0.1 ms than 8 ms due to the contribution of the amorphous region. Significant increase in motion for the region (amorphous softening) is observed at 45 ºC as indicated by the decrease in signal intensity at 0.1 ms due to the decreased contribution of signal intensity from the amorphous region. At 60 ºC the T_{IS} curve undergoes a drastic change in shape indicating a phase change of the pure crystalline PEO (melting), thus the remaining signal represents the crystalline PEO:LiTf region.

Figure 3.8 shows the changes in the ^{13}C signal collected with a contact time of 100 ms for the 20:1 PEO:LiTf at variable temperatures, as well as the ^{13}C T_{IS} curves at temperatures of 25, 45, and 60 ºC. The temperature array shows a reduction in the ^{13}C signal for the lithium containing amorphous region as the temperature rises. A significant signal reduction is observed at 45 ºC, which results in the narrowing of the ^{13}C signal at 0.1 ms. This also results in a change of the overall T_{IS} curve shape between 25 and 45 ºC. The observed signal reduction of the lithium containing amorphous region's signal is most likely due to the increasing mobility of this region, which results in the partial destruction of the dipolar interaction between the $^{1}H/^{13}C$. CPMAS transfers polarization from the ^{1}H to the ^{13}C based upon the dipolar interaction between the two nuclei. The higher the mobility of a system the weaker the dipolar interactions, resulting in less efficient polarization transfer between the nuclei. Less efficient polarization transfer creates smaller NMR signals. In this manner, ^{13}C T_{IS} curves directly detect changes in the PEO backbone dynamics. The NMR signal will continue to decrease until there is sufficient molecular motion to completely destroy the dipolar interactions, which results in an unobservable NMR signal for CPMAS experiments. This is observed for the broad component in the ^{13}C T_{IS} curves from 25 to 55 ºC, which indicates that the mobility of the lithium containing amorphous regions increases with increasing temperature. However, there are no significant changes observed for the NMR signals of the pure and lithium containing crystalline regions in this temperature range indicating that the mobility of

these regions are primarily unchanged. This is most likely due to the temperature being below the melting point of the pure and lithium containing crystalline regions.

At 60 ºC there is a significant change in the T_{IS} curve shape and only the narrow NMR signal is observed. This drastic change in the T_{IS} curve and observed linewidth of the NMR signal is most likely due to a large increase in the molecular motion of the PEO backbone. Since this temperature is close to the reported T_m value of the pure crystalline PEO region in the 20 PEO:LiTf electrolyte,(*5*) we assigned this observed phenomena to the melting of pure crystalline PEO. However, the observation of a CPMAS signal indicates that there is a remaining solid portion. Frech et. al. has shown that the lithium containing crystalline region for 20:1 PEO:LiTf samples has a T_m of 118 ºC,(*5*) thus we assign the existing NMR signal to the microcrystalline 3:1 domains. However, there is a drastic change in the shape of the T_{IS} curve at temperatures above 60 ºC. This is initially puzzling as there are no significant changes in the crystalline 3:1 PEO:LiTf samples in the 60 to 70 ºC temperature range (data not shown). This may be partial explained from reported DSC data. From DSC data, the 3:1 PEO:LiTf has a T_m of 180 ºC with a fairly narrow linewidth, but the 3:1 microcrystalline domains in the 20:1 PEO:LiTf samples have a T_m of 118 ºC with a broad linewidth (linewidth is 100 to 140 ºC).(*5*) The most likely reason for this is that crystalline sample relies on the vibrational and librational forces to break apart the PEO-Li interactions, but the heterogeneous samples have microcrystalline PEO-Li

complexes that are surrounded by molten material. This molten material adds a high degree of molecular motion at the interface between the two regions that may aid in “unzipping” the PEO-Li complex, thereby lowering the melt point of these microcrystalline domains. Thus, at 60 ºC the 3:1 microcrystalline domains are “floating” in a gelatinous material. So even though the 3:1 microcrystalline domain are still solid these crystallites are in constant bobbing and rocking motions, which changes the efficiency of polarization transfer, resulting in the observed shape change in the T_{IS} curve.

Previous variable temperature studies have focused primarily on ^{7}Li NMR experiments.(*50-58*) These experiments correlate the mobility of the lithium ion with segmental motion of the amorphous PEO backbone. However, this approach gives no information on the dynamics of the other domains and how they interact. There have been a limited number of ^{13}C $T_{1\rho}$ studies performed and most were fairly vague and relied on the previous peak assignments for pure PEO. As seen in section 1 of this chapter, the previous NMR assignments for pure PEO were incorrect, thus subsequent studies that replied on these assignments are flawed.

Maunu *et. al.* investigated the $T_{1\rho}$ relaxation rates for PEO:salt of $LiClO_4$, $NaClO_4$, BaSCN, BaI_2, and $Ba(ClO_4)_2$. This investigation was carried out at ambient temperature and high salt concentrations (10:1 to 1:1). This studied observed primarily the narrow NMR signal and seen that decreasing the salt concentration increased the relaxation rate.(*24*) This group also carried out a variable temperature study of 10:1 PEO:$Ba(ClO_4)_2$ samples.

Due to the relatively high salt concentration, the narrow signal was primarily observed and studied. They report that the $T_{1\rho}$ rate increase as temperature increases. There is no mention of shape changes for the T_{IS} curves, but this is probably due to the high salt concentrations.(*30*) To my knowledge, there has not previously been a variable temperature study of T_{IS} curves or $T_{1\rho}$ rates for dilute PEO:salt samples. The observation of the temperature dependence on the dynamics of the amorphous, pure crystalline PEO, and lithium containing crystalline PEO regions are missing from the NMR studies. Also the drastic change that we observed for the shape of the T_{IS} curves at the pure crystalline PEO melt has not been previously reported.

The REDOR and T_{IS} data above suggest that there is a significant increase in polymer backbone mobility, which we have assigned to the melting of pure crystalline PEO (observed at 60 ºC). The melting of the pure crystalline region should result in a significant increase in lithium ion mobility resulting in higher ionic conductivity. Thus, we collected static ^{7}Li NMR data at variable temperatures to confirm the above observed mobility changes. An increase in the lithium ion mobility, results in the observation of a narrower lithium NMR signal. The lithium linewidth data was plotted vs. temperature (Figure 3.9). As seen in Figure 3.9, this resulted in the steady narrowing of the lithium linewidth at temperature between 25 to 55 ºC, but the lithium linewidth narrows by ~150 Hz from 55 to 60 ºC. This drastic narrowing of the linewidth indicates a significant increase in the mobility of the lithium ions attributed to the melting of the pure crystalline PEO. This is in good

agreement with the inferences made form the REDOR and T_{IS} data above. The lithium linewidth continues to narrow from 60 to 100 ºC, but the rate that ion mobility increase is less that for temperature between 25 to 55 ºC. This is most likely because the mobility changes for the remaining crystalline material (3:1 PEO:LiTf complex) is limited, since the melting point for this region is above these temperatures. However, our lithium linewidth data agrees with the accepted trends previously reported.(*5*)

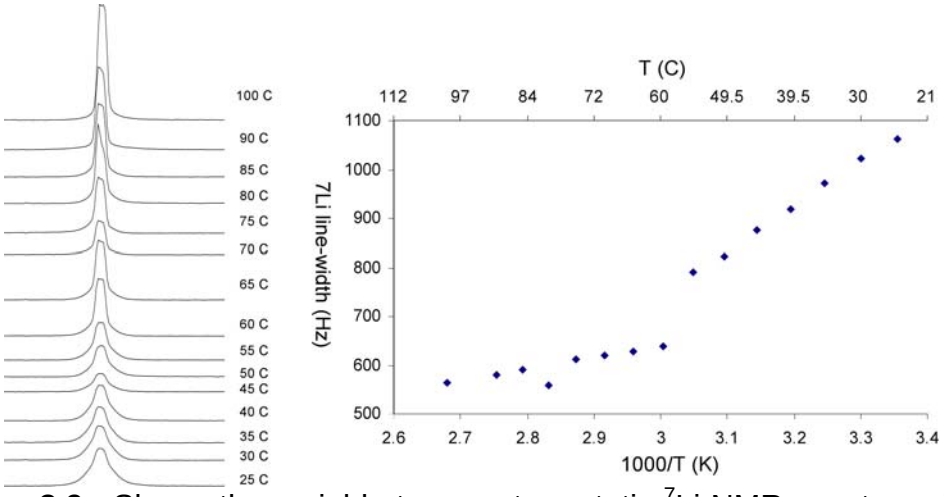

Figure 3.9. Shows the variable temperature static ^{7}Li NMR spectra collected from 25 – 100 ºC in 5 ºC intervals (left side), and a chart of temperature vs. ^{7}Li linewidth (right side). This demonstrates the narrowing of the NMR signal due to the increase in lithium ion transport as temperature increases. It is also observed that there is a drastic narrowing of the ^{7}Li linewidth between the temperature of 55 and 60 ºC, indicating the melting of the pure PEO crystalline region and increase in PEO backbone mobility. The right side of the Figure shows a graph of temperature vs. ^{7}Li linewidth. This graph shows that the decrease at a faster rate from 25 – 55 ºC than it does from 60 – 100 ºC, and that there is a sudden decrease in ^{7}Li linewidth of ~150 Hz from 55 – 60 ºC. The drastic change in linewidth corresponds with the melting of the pure crystalline PEO region, resulting in an increase of mobile PEO to transport the lithium cations through the material.

Conclusions:

No significant structural changes were observed with variable temperature REDOR experiments. T_{IS} curves shown that the lithium containing amorphous regions molecular mobility steadily increases with increasing temperature. T_{IS} curves also shown that the pure crystalline PEO region quickly melts and becomes very mobile between 55 and 60 ºC as demonstrated by a drastic change in the shape of T_{IS} curve. This is corroborated with the drastic narrowing of the lithium linewidth in lithium variable temperature experiments. The inability to collect a REDOR dephasing curve at temperature above 55 ºC indicate that the dipolar interactions between ^{13}C and ^{7}Li are averaged away. Judging from the collected T_{IS} and Li linewidth data, it is most likely that the dipolar interactions are being average away by the bobbing and rocking movements of the crystallites within the molten PEO material.

Reference:

1. V. Chandrasekhar, *Adv. Polym. Sci.* **135**, 139 (1998).
2. P. V. Wright, *Br. Polym. J.* **7**, 319 (1975).
3. C. Berthier *et al.*, *Solid State Ionics* **11**, 91 (1983).
4. R. Frech, S. Chintapalli, P. G. Bruce, C. A. Vincent, *Chem. Commun.*, 157 (1997).
5. R. Frech, S. Chintapalli, P. G. Bruce, C. A. Vincent, *Macromolecules* **32**, 808 (1999).
6. B. L. Papke, M. A. Ratner, D. F. Shriver, *J. Electrochem. Soc.* **129**, 1434 (1982).
7. Y. G. Andreev, P. G. Bruce, *J. Phys.: Condens. Matter* **13**, 8245 (2001).
8. M. Armand, J. M. Tarascon, *Nature* **414**, 359 (2001).
9. Z. Gadjourova, Y. G. Andreev, D. P. Tunstall, P. G. Bruce, *Nature (London)* **412**, 520 (2001).
10. S. Lascaud *et al.*, *Macromolecules* **27**, 7469 (1994).
11. A. Vallee, S. Besner, J. Prud'homme, *Electrochim. Acta* **37**, 1579 (1992).
12. M. Kumar, S. S. Sekhon, *Ionics* **8**, 223 (2002).
13. S. Chintapalli, R. Frech, *Solid State Ionics*, 341 (1996).
14. S. Chintapalli, R. Frech, *Solid State Ionics* **85**, 61 (1996).
15. C. P. Rhodes, R. Frech, *Macromolecules* **34**, 2660 (2001).
16. S. Chintapalli, R. Frech, *Electrochim. Acta* **43**, 1395 (1998).
17. L. Yang, A. Zhang, B. Qiu, *Solid State Ionics* **28-30**, 1029 (1988).
18. B.-K. Choi, *Solid State Ionics* **168**, 123 (2004).
19. B. L. Papke, M. A. Ratner, D. F. Shriver, *J. Electrochem. Soc.* **129**, 1694 (1982).
20. P. Lightfoot, M. A. Mehta, P. G. Bruce, *Science* **262**, 883 (1993).

21. T. M. Connor, A. Hartland, *J. Polym. Sci.: Polym. Phys. Ed.* **7**, 1005 (1969).

22. J. J. Dechter, *J. Polym. Sci.: Polym. Phys. Ed.* **23**, 261 (1985).

23. A. Johansson, J. Tegenfeldt, *Macromolecules* **25**, 4712 (1992).

24. S. L. Maunu, K. Soljamo, M. Laantera, F. Sundholm, *Macromol. Chem. Phys.*, 723 (1994).

25. J. Spevacek, J. Brus, *Macromol. Symp.*, 111 (2003).

26. J. Spevacek, J. Dybal, *Macromol. Rapid Commun.* **20**, 435 (1999).

27. J. Brus, J. Dybal, P. Schmidt, J. Kratochvil, J. Baldrian, *Macromolecules* **33**, 6448 (2000).

28. S. Schantz, *Macromolecules* **30** 1419 (1997).

29. J. Spevacek, L. Paternostre, P. Damman, A. C. Draye, M. Dosie`re, *Macromolecules* **31**, 3612 (1998).

30. S. Schantz, S. L. Maunu, *Macromolecules* **27**, 6915 (1994).

31. M. Wobst, *J. Polym. Sci. Part B: Polym. Phys.* **26**, 527 (1988).

32. P. G. C. Bruce, Stephen A.; Lightfoot, Philip; Mehta, Mary Anne, *Solid State Ionics*, 191 (1995).

33. D. Fauteux, P. McCabe, *Polym. Adv. Techn.* **6**, 83 (1995).

34. D. Reichert, O. Pascui, P. Judeinstein, T. Gullion, *Chem. Phys. Lett.* **402**, 43 (2005).

35. T. Gullion, *Concepts Magn. Reson.* **10**, 277 (1998).

36. M. Bak, J. T. Rasmussen, N. C. Nielsen, *J. Magn. Reson.* **147**, 296 (2000).

37. A. F. Bartolotta, Claudia; Geppi, Marco; Minniti, Domenico; Visalli, Giuseppe, *Solid State Nucl. Magn. Reson.*, 231 (1997).

38. P.-L. Kuo, S.-S. Hou, C.-Y. Lin, C.-C. Chen, T.-C. Wen, *J. Polym. Sci. Part A: Polym. Chem.*, 2051 (2004).

39. J. Spevacek, J. Brus, J. Dybal, *Solid State Ionics* **176**, 167 (2005).

40. A. Boman, U. Edlund, H. Forster, D. Johnels, *Acta Chemica Scandinavica* **53**, 699 (1999).

41. Y. Ishii, T. Terao, S. Hayashi, *J. Chem. Phys.* **107**, 2760 (1997).

42. L. J. Smith, F. P. Boulineau, D. Raftery, A. Wei, *J. Am. Chem. Soc.* **125**, 14958 (2003).

43. J. R. Wickham, S. S. York, N. M. Rocher, C. V. Rice, *J. Phys. Chem. B* **110**, 4538 (2006).

44. G. S. MacGlashan, Y. G. Andreev, P. G. Bruce, *Nature (London)* **398**, 792 (1999).

45. E. Staunton, Y. G. Andreev, P. G. Bruce, *J. Am. Chem. Soc.* **127**, 12176 (2005).

46. A. M. Christie, S. J. Lilley, E. Staunton, Y. G. Andreev, P. G. Bruce, *Nature (London)* **433**, 50 (2005).

47. Z. Stoeva, I. Martin-Litas, E. Staunton, Y. G. Andreev, P. G. Bruce, *J. Am. Chem. Soc.* **125**, 4619 (2003).

48. C. Zhang, E. Staunton, Y. G. Andreev, P. G. Bruce, *J. Am. Chem. Soc.* **127**, 18305 (2005).

49. S. J. Lilley, Y. G. Andreev, P. G. Bruce, *J. Am. Chem. Soc.* **128**, 12036 (2006).

50. C. Roux, W. Gorecki, J. Y. Sanchez, M. Jeannine, E. Belorizky, *J. Phys. Condens. Matter* **7**, 6823 (1995).

51. C. Roux, W. Gorecki, J. Y. Sanchez, M. Jeannine, E. Belorizky, *J. Phys. Condens. Matter* **8**, 7005 (1996).

52. D. Golodnitshy *et al.*, *J. Phys. Chem. A* **105**, 10098 (2001).

53. L. Hong, L. Shi, X. Tang, *Macromolecules* **36**, 4989 (2003).

54. P. H. d. Souza *et al.*, *Chem. Mater.* **13**, 3685 (2001).

55. J. Adebahr *et al.*, *Phys. Chem. Chem. Phys.* **5**, 720 (2003).

56. S. Wong, S. Vasudevan, R. A. Vaia, E. P. Giannelis, D. B. Zax, *J. Am. Chem. Soc.* **117**, 7568 (1995).

57. P. Mustarelli, C. Capiglia, E. Quartarone, C. Tomasi, P. Ferloni, *Phys. Rev. B* **60**, 7228 (1999).

58. K. J. Adamic *et al.*, *Chem. Mater.* **3**, 534 (1991).

Part II

Solid-State NMR Investigations of Teichoic Acid Biopolymers

Chapter 4:

Teichoic Acid background

Teichoic acids play a major role in the survival and prosperity of gram-positive bacteria. Some of the major functions of teichoic acids are intercalating nutrients and waste products, cell-to-cell signaling, resistance to antibiotics (promoting cell virulence), as well as being the primary adhesion molecule.(*1-10*) Teichoic acid is a major component (30–60% by mass) of gram-positive cell walls.(*3, 5, 11*) The cell wall of gram-positive bacteria is a complex system of lipids and proteins within a peptidoglycan matrix.[11]

A peptidoglycan matrix is a copolymer composed of a disaccharide backbone with repeating units of N-acetylglucosamine (GlcNAc) and N-acetylmuramic acid (MurNAc) that are cross-linked with peptides (Ala-i-Gln-Lys-Ala).(*5*) Peptidoglycan is the major structural unit of the cell wall that helps the cell retain shape, undergo division, and maintain hydrostatic pressure within the cell. Recent data suggests that peptidoglycan has large pores, which allows teichoic acid inclusion.(*12*) There are two different types of teichoic acids in the cell wall of gram-positive bacteria, being lipoteichoic acid (LTA) and wall teichoic acid (WTA).(*3, 5, 11*)

Teichoic Acid Structure

Both LTA and WTA contain disaccharide D-glucose head groups with a teichoic acid chain attached (Figure 4.1A, B, & C).(*5*) There are two possible forms of WTA, being either the poly(glycerol-phosphate) backbone (Figure 4.1B) or poly(ribitol-phosphate) backbone (Figure 4.1C). However, LTA is composed of only the poly(glycerol-phosphate) backbone (Figure 4.1A).(*13, 14*) Through proton and carbon liquid state NMR, the structure of teichoic acids has been determined.(*15-21*) The teichoic acid chain is a poly(phosphodiester) with an average length of 20-50 repeat units,(*5, 16, 18, 20, 22*) although some bacterial strains have been shown to have significantly fewer repeat units,(*15*) decorated with D-alanine, *N*-acetylglucosamine, and hydroxyl groups.(*22-24*) At pH < 7, the D-alanine groups are cationic, the phosphodiesters are anionic, and both the N-acetylglucosamine and hydroxyls are neutral.(*22-24*) This results in incomplete charge neutralization,(*4*) which allows teichoic acid to form ionic bonds with surrounding fluids, dissolved ions, and substrates as well as intramolecular contact ion pairs between the D-alanine and phosphate groups. The distribution of alanine, *N*-acetylglucosamine, and hydroxyl branches is heterogeneous and varies with different bacterial strains.

The main difference between LTA and WTA is that LTA contains a lipid tail group while WTA is covalently attached to the cell wall.(*5*) It has been well established that the lipid tail group on the LTA is anchored in the cell

membrane with the teichoic acid chain extending out past the cell wall (Figure 4.1D),(*25*) while the head group of WTA is covalently anchored to the cell wall through a phosphodiester bond.(*5*) However, the structure/orientation of WTA within the cell wall is not as definitive. Does WTA remain completely within the cell wall (Figure 4.1E) or extend out of the cell wall (Figure 4.1F & 4.1G)? Whether the orientation of WTA maintains a unique conformation or exhibit all possible conformations is uncertain, but bacterial adhesion studies suggest that WTA is capable of extending past the cell wall (Figure 4.1E & 4.1F).(*26, 27*)

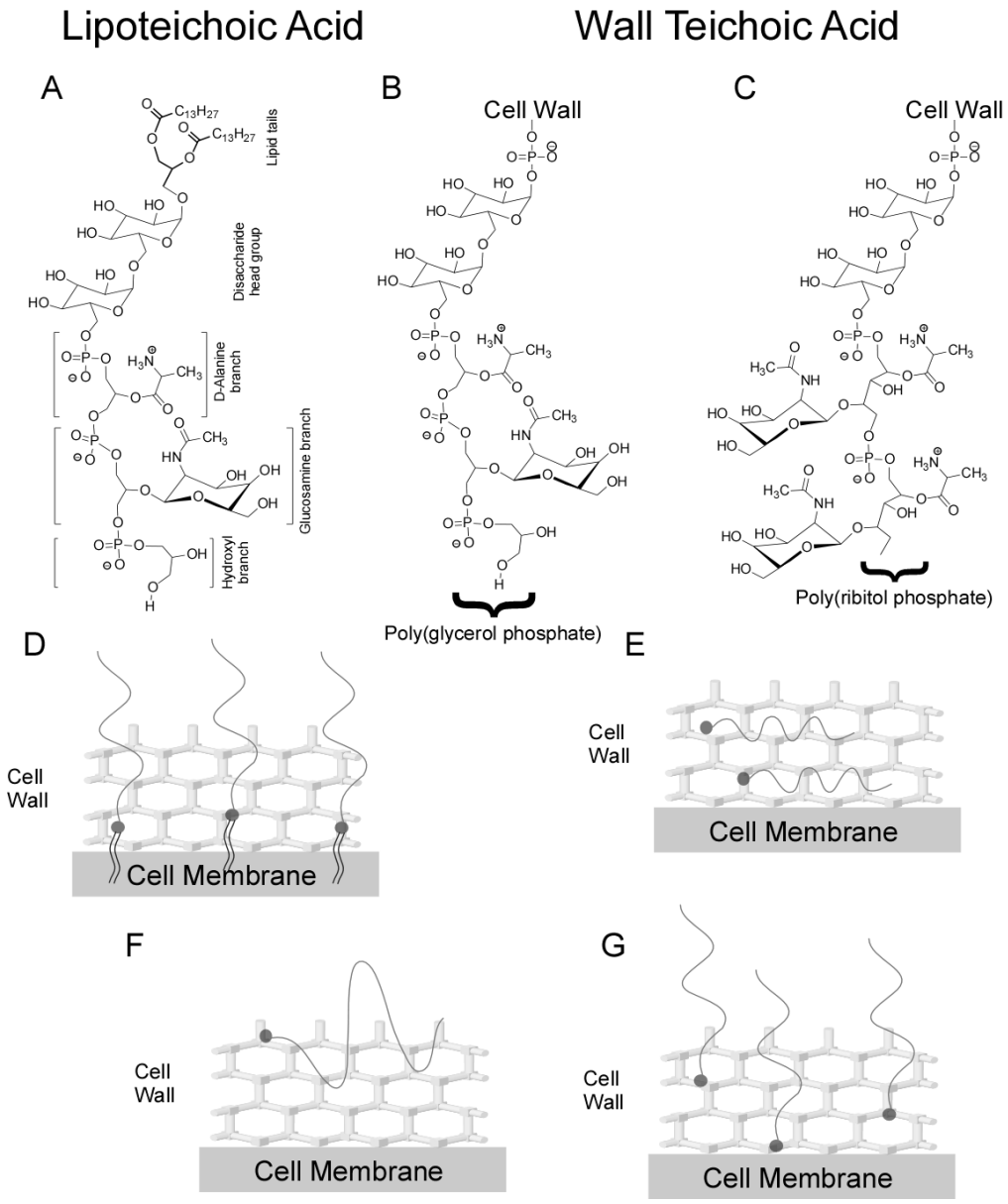

Figure 4.1. Shows the chemical structure of teichoic acids found in the cell wall of Gram(+) bacteria. The polyphosphate backbone is very long, with 40-50 repeat units dependent upon the species of bacteria. The many different constituents of teichoic acid facilitate chemical interactions with various ionic species, water, and the cell wall (peptidoglycan).

Formation of Teichoic Acids

The biosynthetic mechanism of LTA formation is not well understood.(*5, 8, 20, 22, 28-31*) It is typically thought that a glycerol phosphate is joined to a glycolipid, and subsequent glycerol phosphates extend the teichoic acid chain length. N-acetylglucosamine units are then incorporated via uridine 5'-diphospho-N-acetylglucosamine (UDP-GlcNAc) and a GlcNAc transfer protein.(*32*) Dlt operons encode the biosynthesis of carrier proteins responsible for the addition of D-alanine by esterification of the glycerol units of the LTA backbone.(*20, 29*) Structures of these biochemical compounds are shown in Figure 4.2. The genetic basis for LTA synthesis is unknown; thus, generation of LTA-absent mutants is not possible.(*5, 13, 33, 34*) A complex, multi-step, chemical synthesis of LTA has been reported.(*16, 18, 35, 36*) However, these teichoic acids are very short having 5 phosphate repeat units, and exhibit a 100 fold reduction in bioactivity compared to natural LTA.(*18*) This synthesis scheme allows D-alanine to be replaced with L-alanine, which causes a complete loss of bioactivity.(*18*)

Knowledge of the biosynthetic pathway of WTA formation is more complete, as assembly and transport events have been linked to several genes and their associated proteins. For *B. subtilis* strain 168, the teichoic acid backbone is composed of poly(glycerol phosphate) and the genes are denoted *tagABCEFGHO.*(*13, 37, 38*) Production of the poly(ribitol phosphate) form of WTA in *B. subtilis* W23 is controlled by synthesis proteins that are

produced by genes *tarABIJKLDF.*(*13, 38*) Efforts are underway to identify the structure of the protein products, thereby aiding in the development teichoic acid synthetic pathway inhibitors.(*39, 40*) The synthesis of important substrates has been reported for the enzymes tagA and tagB. This work demonstrates the function of tagA and tagB, while also providing useful insights towards drug based on enzyme inhibition. Isotopic labeling with tritium has allowed radioisotope studies of the poly(glycerol phosphate) backbone.(*34*) This data showed that the majority (70-80%) of the 2-^{3}H-glycerol is used for the poly(glycerol phosphate) of WTA rather than the poly(glycerol phosphate) of phospholipids or LTA.

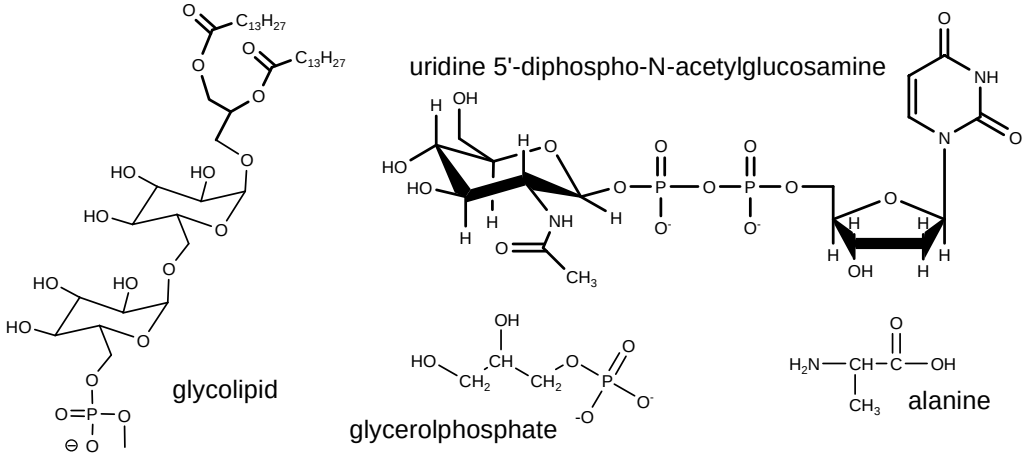

Figure 4.2. Displays the chemical structures of biochemical compounds that are involved in the production of LTA.

Teichoic Acids regulate nutrients (metal binding)

Teichoic acids can extend away from the cell and are one of the first cellular components to come in contact with other cells, molecules, nutrients,

and surfaces. The cell wall of gram-positive bacteria attracts metal cations because of its net negative charge, largely due to the phosphate groups of teichoic acids, although there is a contribution from anionic amino acids in the peptide stems and cross-links.

Teichoic acid binds metals in a competitive manner due to its anionic phosphate groups. However, it is important to note that at pH of 7 the phosphate groups are deprotonated (PO_4^-), while the amines of the alanine braches are protonated (NH_3^+). The difference in charge facilitates the formation of an ion pair between the phosphate and alanine groups. This ion pairing prevents these phosphates from participating in metal binding, which was demonstrated by an 60% increase in Mg^{2+} binding when D-Alanine was removed from the teichoic acids.(*41*) This lead to two different proposed binding structures of Mg^{2+} with the phosphates of the teichoic acid backbone. Both of these structures show the Mg^{2+} ion binding in a monodentate fashion with either a signal phosphate or acting as a bridging atom between two phosphates (Figure 4.3).(*42, 43*) However, removal of the teichoic acid polymer from *S. aureus* did not completely eliminate Mg^{2+} binding demonstrating that peptidoglycan also plays a significant role in Mg^{2+} binding.(*44*) The addition of NaCl and KCl had little effect on Mg^{2+} concentration while $CaCl_2$ replaced Mg^{2+} in the cell wall.(*45*) Metal binding of Mg^{2+}, Fe^{3+}, Cu^{2+}, Na^+ and K^+ are showed to be favored, while Mn^{2+}, Zn^{2+}, Ca^{2+}, Au^{3+}, and Ni^{2+} show intermediate binding and Hg^{2+}, Sr^{2+}, Pb^{2+}, Ag^+, Li^+, Ba^{2+}, Co^{2+} and Al^{3+} show little or no binding.(*46, 47*) This metal binding trend

is not easily explained, but seems to be related with the atomic radii of the metals, with the optimal atomic radii being between 0.7 and 1 Å. The uptake of Mg^{2+} ions is vital for bacterial survival, which is demonstrated by the replacement of Mg^{2+} with Ca^{2+} resulting in bacterial death. The need for teichoic acid to associate and migration Mg^{2+} ion through the cell wall is demonstrated by studies of bacteria grown in low Mg^{2+} concentrations. These bacteria showed significant increases in the amount of teichoic acid that the bacteria produced in the cell wall, which resulted in a higher affinity for Mg^{2+}.(*48, 49*) Bacterial strains with teichoic acid removed show a decreased affinity for Mg^{2+}, K^{+}, and Na^{+} and an inability to bind Ca^{2+}.(*44*) This demonstrates that both teichoic acid and peptidoglycan are responsible for the binding of Mg^{2+}, K^{+}, and Na^{+}, but teichoic acid is solely responsible for the binding of Ca^{2+}.

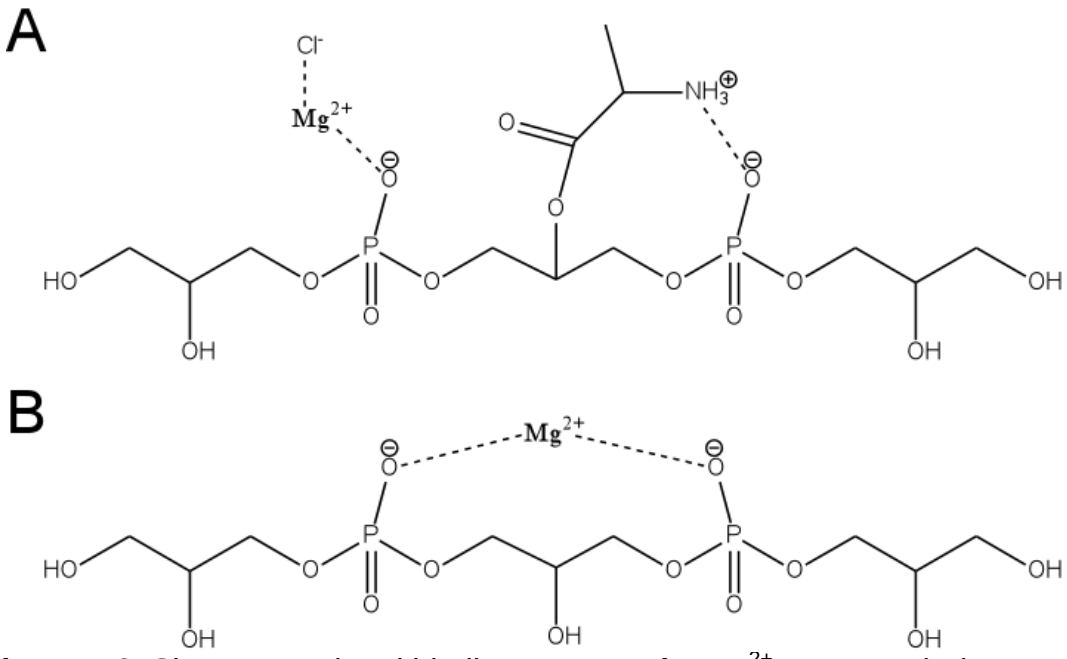

Figure 4.3. Shows postulated binding structure for Mg^{2+} to LTA. A) shows the monodentate of Mg^{2+} to one phosphate with the other tied up with an ion pair to alanine. B) shows the monodentate bridging of Mg^{2+} between two phosphates in the absence of the ion pair to alanine.

Teichoic Acids are vital for bacterial survival

It has been demonstrated that teichoic acids are crucial to the regulation of mitosis and bacterial defenses. Bacterial mutants with D-alanine deficient LTA are more susceptible to various antimicrobial agents,(*30, 31*) which may be a result of altered ionic interactions. Removal of D-Alanine from teichoic acids has also shown to increase the susceptibility to attack from human neutrophils.(*50, 51*) Mice, which were infected with these mutated bacteria, exhibit lower bacterial counts in their infected organs due to their diminished defensive capabilities. LTA is also thought to protect the

bacteria in acidic conditions (such as in tooth carries) and the removal of the alanine branches leads to bacterial death.(*5, 8, 20, 22, 30*) *Lactobacillus casei* mutants with D-alanine deficient LTA were unable to divide and the exhibited abnormal cell shapes.(*51, 52*) Other mutation studies have shown that the D-alanine groups are needed to inhibit autolysis.(*53, 54*) Autolysin AcmA binding to LTA increases when the D-alanine groups are removed, which results in faster degradation of the peptidoglycan cell wall and cell death.

Antibiotics resistant strains are known and increasing, but the development of antibiotics has decreased.(*33, 40*) Due to their active role in bacterial defense, teichoic acids have become antimicrobial targets. As mentioned above, teichoic acids play a crucial role in the regulation of the cell wall; thus, blocking production of teichoic acids will cause cell death. Since it is known that tagA and tagB enzymes are important to the biosynthesis of teichoic acid, cell death can be caused by inhibiting these enzymies.(*40, 55*) It has also been mentioned that the D-alanine braches play an important role in the functionality of teichoic acids. Thus, dlt operons are now a new antibiotic target due to their role in D-alanine addition to teichoic acids.(*33*) This also makes the teichoic acid more susceptible to cationic antimicrobial peptides due to the loss of repulsive forces that were provided by the D-alanine braches.(*33*)

Teichoic Acids participation in cell signaling

Gram-positive bacteria in the bloodstream cause infections throughout the body. LTA has been shown to activate cytokines, which are small proteins involved in the regulation of the immune response. Cytokine release was demonstrated by the binding of purified LTA to the toll-like receptor TLR-2.(*3, 18, 56-58*) The immune response triggered by cytokine release can be either inflammatory or anti-inflammatory depending on the type that is released.(*56*) The undesirable response to cytokine release is inflammation, which is typical observed with bacterial infections. The ability of LTA to induce an inflammatory cytokine release is thought to be a cause of sepsis, septic shock, and multiple organ failure.(*56, 59, 60*) This generally happens when LTA is released from bacteria as antibiotics destroy them, which is one reason why antibiotics that target teichoic acid are desirable.(*61*) However, recent studies have shown that LTA aids in the symbiotic relationship between intestinal bacteria and the host through controlling anti-inflammatory cytokine release.(*56*), (*62*) These different immune responses are thought to occur due to the slightly different compositions of LTA between different stains of bacteria. This has been demonstrated with *lactobacilli* bacteria through comparison between the wild type and D-alanine deficient LTA containing mutants, which showed a dramatic decrease in the amount of pro-

inflammatory cytokine release.[56] This change in immune response is due to the TLR-2 receptors being a pattern recognition receptor, which makes the type of cytokine release dependent on the composition of LTA.(*56*)

Teichoic Acids are a primary adhesion molecule

Teichoic acids can extend out past the edge of the cell wall and are thought to be the bacterium's initial adhesion molecule.(*1-4, 9, 10, 63*) Bacterial adhesion is a crucial step for the formation of biofilms, which are colonies of bacterial cells that have adhered to a surface and formed a protected biological environment.(*64-76*) The formation of biofilms can be condensed into a four-step process.(*4, 77-79*) First, planktonic cells attach to the surface, followed by the production of extracellular polymeric substances (slime), the development of a biofilm architecture, and finally biofilm spreading through bacterial release (Figure 4.4).

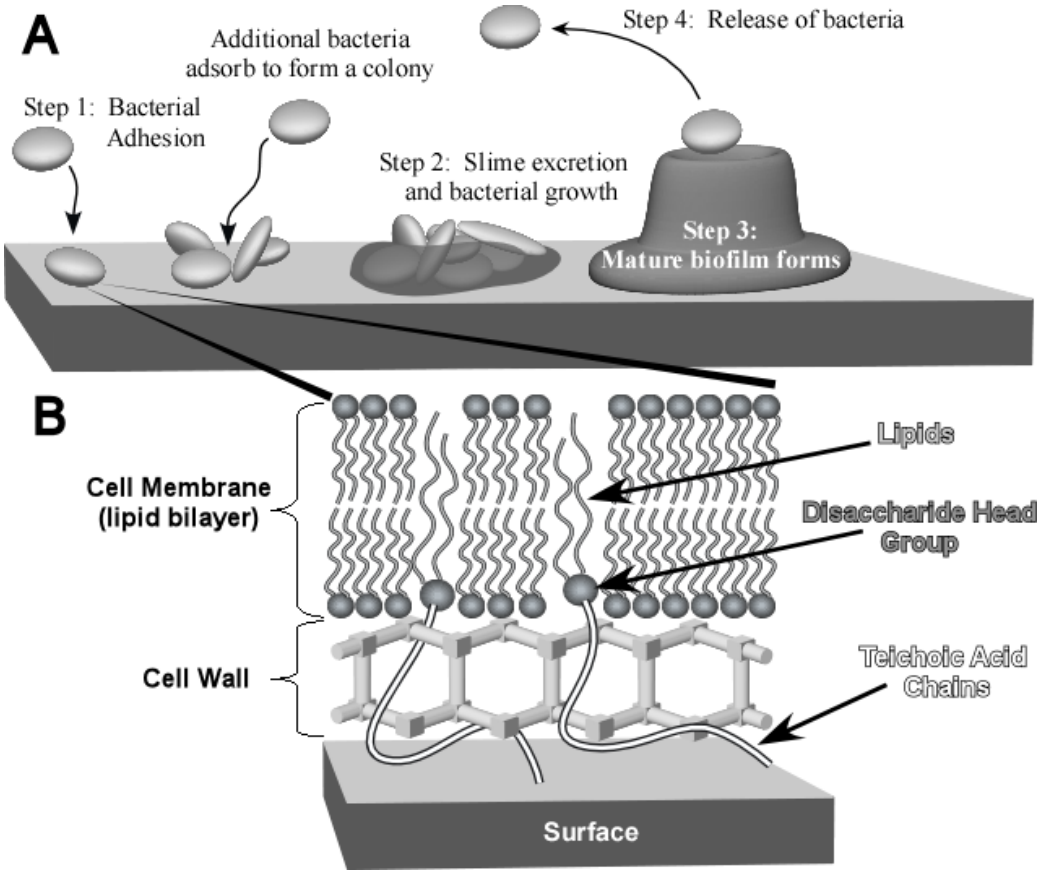

Figure 4.4. A) shows the 4 step process involved in the formation of biofilms. B) shows the lipoteichoic acid is anchored to the cell membrane and extends out past the edge of the cell wall being the initial molecular contact between the bacterium and other materials.

Gram-positive biofilms are associated with a host of different post-surgical chronic infections.(*2, 3, 8, 19, 30, 58, 80-85*) These different infections are associated with a wide variety of materials and tissues. Catheters,(*63, 77, 79, 86*) contact lenses,(*77, 86*) intrauterine devices (IUD),(*77, 86*) and dental unit water lines(*77*) are just some medical materials that have been shown to contain biofilms that provide a means of pathogen introduction into the body. Biofilms are also responsible for various chronic infections of different tissues within the body such as dental cavities,(*86, 87*)

(*78, 79, 88*) and native valve endocarditis,(*77, 89*) prosthetic heart valves,(*79, 86*) pacemakers,(*79*) joints/bone implants,(*63, 79*) vascular grafts,(*79, 86*) and other implant materials can also be infected with biofilms and are generally the root of post-surgical chronic infections. It has also been suggested that these implant materials may become infected after implantation by biofilms that were either already within the body or introduced after surgery.(*79*) Gram-positive biofilms have also been indicated as a cause of septic shock and multiple organ failure.(*56, 59, 60*) Although biofilms are detrimental to biological health, they can actually be beneficial to industrial materials by acting as a protective layer that prevents corrosion.(*90*)

Efforts to eliminate existing biofilms have met with minimal success, due to the ability of the protective slime layer to regulate the substances that migrate through it.(*63, 77-79*) Studies have shown that it takes 10 – 1000 times the concentration of an antimicrobial agent to kill a biofilm than it does to kill a single bacterium.(*77, 78*) Thus, preventive treatments may be the best way to eliminate biofilm infections; however, this requires a detailed understanding of the initial steps of biofilm formation. Jefferson's review states that 'knowledge of how biofilms adhere to solid surfaces is crucial to understanding biofilm growth'.(*78*) However, there is very little molecular level information available for the initial bacterial adhesion to solid surfaces.

Due to the orientation differences shown in Figures 4.1D-G, it is thought that the primary function of LTA is cell signaling and adhesion,(*1, 4, 5, 33*) while the primary function for WTA is thought to be ion transport and

control of the enzymes responsible for bacterial growth and division.(*91, 92*) It has been shown that D-alanine deficient LTA bacterial mutants lose their ability to adhere to polystyrene, glass, and metal oxide surfaces, indicating that LTA is the initial contact, must be the present to adhere, and must exhibit some cationic character.(*1, 4, 5*) It has also been shown that the addition of Mg^{2+} restores its adhesion ability, reaffirming the need for cationic charges, allowing LTA to promote adhesion through charge interactions.(*4, 5*) The D-alanine deficient LTA *Listeria monocytogenes* mutants also exhibited diminished adhesion abilities onto mammalian cells.(*1*) Though it is not clear how D-alanine contributes to this adhesion mechanism. Although LTA is generally accepted as being the initial adhesion molecule,(*4, 63*) there are cases that have correlated WTA with biofilm formation on endothelial cells in nosocomial infections.(*89, 93*) These studies have shown that WTA deficient *S. aureus* infected within the nostrils of rats, human nasal epithelial cells, blood-borne infections, endothelial cells, and internal rabbit organs (heart, kidneys, and spleen), all exhibited dramatic reductions in adhesion densities.(*89, 93, 94*)

Reference:

1. E. Abachin *et al.*, *Mol. Microbiol.* **43**, 1 (2002).
2. H. S. Courtney, D. L. Hasty, J. B. Dale, *Ann. Med.* **34**, 77 (2002).
3. I. Ginsburg, *Lancet Infect. Dis.* **2**, 171 (2002).
4. M. Gross, S. E. Cramton, F. Gotz, A. Peschel, *Infect. Immun.* **69**, 3423 (2001).
5. F. C. Neuhaus, J. Baddiley, *Microbiol. Mol. Biol. Rev.* **67**, 686 (2003).
6. L. M. Tellefson, G. R. Germaine, *J. Dent. Res.* **63**, 188 (1984).
7. L. M. Tellefson, G. R. Germaine, *Infect. Immun.* **51**, 750 (1986).
8. C. Weidenmaier, S. A. Kristian, A. Peschel, *Curr. Drug Targets* **4**, 643 (2003).
9. R. Rose, *Biochim. Biophys. Acta* **1475**, 76 (2000).
10. I. Fedtke, F. Gotz, A. Peschel, *Int. J. Med. Microbiol.* **294**, 189 (2004).
11. L. L. Graham, T. J. Beveridge, *J. Bacteriol.* **176**, 1413 (1994).
12. S. O. Meroueh *et al.*, *Proc. Natl. Acad. Sci. U.S.A.* **103**, 4404 (2006).
13. A. P. Bhavsar, E. D. Brown, *Mol. Microbiol.* **60**, 1077 (2006).
14. A. P. Bhavsar, L. K. Erdman, J. W. Schertzer, E. D. Brown, *J. Bacteriol.* **186**, 7865 (2004).
15. P. Roethlisberger *et al.*, *Eur. J. Biochem.* **267**, 5520 (2000).
16. A. Stadelmaier, S. Morath, T. Hartung, R. R. Schmidt, *Angew. Chem. Int. Ed.* **42**, 916 (2003).
17. N. V. Potekhina, A. S. Shashkov, L. I. Evtushenko, S. y. N. Senchenkova, I. B. Naumova, *Carbohyd. Res.* **338**, 2745 (2003).
18. S. Morath, A. Stadelmaier, A. Geyer, R. R. Schmidt, T. Hartung, *J. Exp. Med.* **195**, 1635 (2002).
19. S. Morath, A. Geyer, I. Spreitzer, C. Hermann, T. Hartung, *Infect. Immun.* **70**, 938 (2002).
20. B. F. Volkman *et al.*, *Biochemistry* **40**, 7964 (2001).

21. W. Fischer, T. Behr, R. Hartmann, J. Peter-Katalinic, H. Egge, *Eur. J. Biochem.* **215**, 851 (1993).

22. M. P. Heaton, F. C. Neuhaus, *J. Bacteriol.* **176**, 681 (1994).

23. T. Behr, W. Fischer, J. Peterakatalinic, H. Egge, *Eur. J. Biochem.* **207**, 1063 (1992).

24. H. Iwasaki, A. Shimada, K. Yokoyama, E. Ito, *J. Bacteriol.* **171**, 424 (1989).

25. A. Peschel, *Trends Microbiol* **10**, 179 (2002).

26. F. Fiedler, *Infection* **16**, S92 (1988).

27. J. Endl, H. P. Seidl, F. Fiedler, K. H. Schleifer, *Microbiology* **135**, 215 (1983).

28. M. P. Heaton, F. C. Neuhaus, *J. Bacteriol.* **174**, 4707 (1992).

29. M. Perego *et al.*, *J. Biol. Chem.* **270**, 15598 (1995).

30. A. Peschel *et al.*, *J. Biol. Chem.* **274**, 8405 (1999).

31. C. Poyart, M. Lamy, C. Boumaila, F. Fiedler, P. Trieu-Cuot, *J. Bacteriol.* **183**, 6324 (2001).

32. Kawamura, T.; Kimura, M.; Yamamori, S.; Ito, E., *J. Biol. Chem.* **253**, 3595 (1978).

33. F. Gotz, *Curr. Opin. Microbiol.* **7**, 477 (2004).

34. H. M. Pooley, D. Karamata, *Microbiology-Uk* **146**, 797 (2000).

35. K. Fukase *et al.*, *Bull. Chem. Soc. Jpn.* **65**, 2643 (1992).

36. K. Fukase, T. Yoshimura, S. Kotani, S. Kusumoto, *Bull. Chem. Soc. Jpn.* **67**, 473 (1994).

37. A. P. Bhavsar, R. Truant, E. D. Brown, *J. Biol. Chem.* **280**, 36691 (2005).

38. J. W. Schertzer, A. P. Bhavsar, E. D. Brown, *J. Biol. Chem.* **280**, 36683 (2005).

39. C. Ginsberg, Y. H. Zhang, Y. Q. Yuan, S. Walker, *ACS Chem. Biol.* **1**, 25 (2006).

40. N. L. Pohl, *ACS Chem. Biol.* **1**, 14 (2006).

41. S. Heptinstall, A. R. Archibald, J. Baddiley, *Nature (London)* **225**, 519 (1970).

42. P. A. Lambert, I. C. Hancock, J. Baddiley, *Biochem. J.* **151**, 671 (1975).

43. J. Baddiley, I. C. Hancock, P. M. A. Sherwood, *Nature (London)* **243**, 43 (1973).

44. T. J. Beveridge, R. G. E. Murray, *J. Bacteriol.* **141**, 876 (1980).

45. R. J. Doyle, T. H. Matthews, U. N. Streips, *J. Bacteriol.* **143**, 471 (1980).

46. T. J. Beveridge, S. F. Koval, *Appl. Environ. Microbiol.* **42**, 325 (1981).

47. T. J. Beveridge, R. G. E. Murray, *J. Bacteriol.* **127**, 1502 (1976).

48. D. C. Ellwood, *Biochem. J.* **118**, 367 (1970).

49. D. C. Ellwood, D. W. Tempest, *Adv. Microb. Physiol.* **7** 83 (1972).

50. L. V. Collins *et al.*, *J. Infect. Dis.* **186**, 214 (2002).

51. E. Palumbo *et al.*, *J. Bacteriol.* **188** 3709 (2006).

52. A. Ntamere, D. Taron, F. Neuhaus, *J. Bacteriol.* **169**, 1702 (1987).

53. A. Steen *et al.*, *J. Bacteriol.* **187**, 114 (2005).

54. W. Fischer, P. Rosel, H. Koch, *J. Bacteriol.* **146**, 467 (1981).

55. P. Canepari, M. Boaretti, M. M. Lleo, G. Satta, *Antimicrob. Agents Chemother.* **34**, 1220 (1990).

56. C. Grangette *et al.*, *Proc. Natl. Acad. Sci. U.S.A.* **102**, 10321 (2005).

57. S. G. Morath, Armin; Hartung, Thomas, *J. Exp. Med.* **193**, 393 (2001).

58. N. W. J. Schroder *et al.*, *J. Biol. Chem.* **278**, 15587 (2003).

59. C. Thiemermann, *Microbes Infect* **4**, 927 (2002).

60. R. Schwandner, R. Dziarski, H. Wesche, M. Rothe, C. J. Kirschning, *J. Biol. Chem.* **274**, 17406 (1999).

61. C. Heer, K. Stuertz, R. R. Reinert, M. Mader, R. Nau, *Infection* **28**, 13 (2000).

62. W. M. de Vos, *Proc. Natl. Acad. Sci. U.S.A.* **102**, 10763 (2005).

63. F. Gotz, *Mol. Microbiol.* **43**, 367 (2002).

64. S. E. Cramton, C. Gerke, N. F. Schnell, W. W. Nichols, F. Gotz, *Infect. Immun.* **67**, 5427 (1999).

65. W. Ziebuhr *et al.*, *Mol. Microbiol.* **32**, 345 (1999).

66. P. Fey *et al.*, *J. Infect. Dis.* **179**, 1561 (1999).

67. F. Gotz, C. Heilmann, S. Cramton, *Adv. Exp. Med. Biol.* **485**, 103 (2000).

68. C. Heilmann, C. Gerke, F. Perdreau Remington, F. Gotz, *Infect. Immun.* **64**, 277 (1996).

69. C. Heilmann, M. Hussain, G. Peters, F. Gotz, *Mol. Microbiol.* **24**, 1013 (1997).

70. C. Heilmann *et al.*, *Mol. Microbiol.* **20**, 1083 (1996).

71. P. Heilmann, C. Wuster, C. Prolingheuer, M. Gotz, R. Ziegler, *Calcif. Tissue Int.* **62**, 383 (1998).

72. M. Rupp, P. Fey, C. Heilmann, F. Gotz, *J. Infect. Dis.* **183**, 1038 (2001).

73. J. Schneider *et al.*, *Calcif. Tissue Int.* **74**, 246 (2004).

74. F. Schumacherperdreau, C. Heilmann, G. Peters, F. Gotz, G. Pulverer, *FEMS Microbiol. Lett.* **117**, 71 (1994).

75. C. vonEiff *et al.*, *J. Bacteriol.* **179**, 4706 (AUG, 1997).

76. W. Ziebuhr *et al.*, *Infect. Immun.* **65**, 890 (1997).

77. R. M. Donlan, J. W. Costerton, *Clin. Microb. Rev.* **15**, 167 (2002).

78. K. K. Jefferson, *FEMS Microbiol. Lett.* **236**, 163 (2004).

79. L. Hall-Stoodley, J. W. Costerton, P. St, *Nat. Rev. Microbiol.* **2**, 95 (2004).

80. J. Cohen, *Nature (London)* **420**, 885 (2002).

81. D. L. Hasty, I. Ofek, H. S. Courtney, R. J. Doyle, *Infect. Immun.* **60**, 2147 (1992).

82. S. A. Kristian *et al.*, *J. Infect. Dis.* **188**, 414 (2003).

83. E. Mattsson, T. Hartung, S. Morath, A. Egesten, *Infect. Immun.* **72**, 4322 (2004).

84. T. Mitchell, *Nat. Rev. Microbiol.* **1**, 219 (2003).

85. S. von Aulock *et al.*, *Immunobiology* **208**, 413 (2003).

86. J. W. Costerton, P. S. Stewart, E. P. Greenberg, *Science* **284**, 1318 (1999).

87. F. H. Jones, *Surface Science Reports* **42**, 75 (2001).

88. R. K. Rose, S. D. Hogg, R. P. Shellis, *J. Dent. Res.* **73**, 1742 (1994).

89. C. Weidenmaier *et al.*, *J. Infect. Dis.* **191**, 1771 (2005).

90. S. Ponmariappan, S. Maruthamuthu, N. Palaniswamy, R. Palaniappan, *Corrosion Rev.* **22**, 307 (2004).

91. I. B. Naumova *et al.*, FEMS *Microbiol. Rev.* **25**, 269 (2001).

92. R. Wodzki, *Makromol. Chem.* **194**, 2239 (1993).

93. C. Weidenmaier *et al.*, *Nature Medicine* **10**, 243 (2004).

94. C. Weidenmaier *et al.*, *Infect. Immun.* **73**, 8033 (2005).

Chapter 5:

Chapter 5 consists of 2 sections.

Section 1: Adhesion Differences of Teichoic Acids on Various Surfaces: Phosphorus Solid-State NMR Study

Introduction

Biofilms are colonies of bacterial cells that have adhered to a surface and formed a protected biological environment. The formation of biofilms can be condensed to a four-step process.(*1-4*) First, planktonic cells attach to the surface, followed by the production of extracellular polymeric substances (slime), the development of a biofilm architecture, and finally biofilm spreading through bacteria release.

Gram-positive biofilms are associated with a host of different post-surgical chronic infections.(*1, 3-13*) These different infections are associated with a wide variety of materials and tissues. Efforts to eliminate existing biofilms have met with minimal success. This is due to the ability of the protective slime layer to regulate substance migration.(*1, 3, 4, 7*) Studies have shown that it takes 10 – 1000 times the amount of an antimicrobial agent to kill a biofilm than it does to kill a single bacterium.(*1, 3*) Thus, preventive treatments may be the best way to eliminate biofilm infections. Development of preventative treatments requires a detailed understanding of the initial steps of biofilm formation. However, there is very little molecular

level information available for the initial adhesion of bacteria to solid surfaces since this interface is very challenging to study with many analytical techniques. Solid-state NMR is a powerful analytical tool for studying adsorbed species on various surfaces. Yet, there has only been a limited number of NMR studies of teichoic acids[14-19] and none for teichoic acids adhered to surfaces. Thus, solid-state NMR was employed to gain molecular level information of teichoic acid adsorbates.

For gram-positive biofilms the initial adhesion molecule is thought to be teichoic acid.(*2, 7*) The cell wall of gram-positive bacteria contains two different types of teichoic acids being lipoteichoic acid (LTA) and wall teichoic acid (WTA).(*13*) Both LTA and WTA contain a disaccharide D-glucose head group with a teichoic acid chain attached.(*13*) Through proton and carbon liquid state NMR, the structure of teichoic acids has been determined.(*16, 17, 19-23*) The teichoic acid chain is a poly phosphodiester with an average length of 40-50 repeat units decorated with D-alanine, glucosamine, and hydroxyl groups.(*13, 17, 21, 23, 24*) The main difference between the two teichoic acids is that LTA contains a lipid tail group anchored in the cytoplasm lipid by-layer with the teichoic acid chain extending out past the cell wall(*25*) and WTA is covalently attached to the cell wall,(*13*) which has lead to some different functional roles for these teichoic acids.

The current thinking is that the primary function of LTA is cell signaling and adhesion,(*2, 10, 13, 26*) while the primary function for WTA is though to be adhesion, ion transport, and control of the enzymes responsible for

bacterial growth and division.(*27, 28*) LTA is generally accepted as being the initial adhesion molecule,(*2, 7, 13, 26*) although there are cases that have correlated WTA with biofilm formation.(*5, 11*) WTA is also a target for anti-bacterial drug research thus understanding the adhesion properties could be of great benefit to this field.(*10*)

^{31}P solid-state NMR has been used to gain structural and dynamic insight of various phosphorus containing molecules on several different materials.(*29-35*) In this chapter the adhesion properties of both LTA and WTA are studied for various biologically relevant materials.(*8, 36-39*) Here, we use ^{31}P solid-state NMR experiments to gain information about the chemical environments and molecular motions of LTA and WTA by measuring the changes in CSA tensors (Δ_{CSA}), asymmetry parameters (η), and rotating frame spin-lattice relaxation ($T_{1\rho}$) rates for LTA and WTA before and after adhesion to TiO_2.

Experimental

Sample preparation

Staphylococcus aureus lipoteichoic acid (LTA) was purchased from InvivoGen as a lyophilized powder. Staphylococcus aureus wall teichoic acid (WTA) in cell wall and staphylococcus aureus cell wall were provided to us from Prof. Eric Brown (McMaster Univ.). LTA and WTA samples were dissolved in double distilled water followed by the addition of the desired substrate. This was immediately followed by thoroughly mixing the solution

with a vortex mixer and allowed to sit for 24 hours at 4 °C. Samples were then centrifuged and the remaining pellet was initially dried in a desiccator followed by drying under room temperature vacuum oven. The dried pellet was then packed directly into the NMR rotor. Partially hydrated samples were packed into NMR rotor after desiccant drying then remaining water was removed by placing the NMR rotor in the vacuum oven.

The substrates, which the teichoic acids were adhered to, are cellulose (obtained from Aldrich), titanium dioxide (obtained from Kerr-McGee), and cell wall material (obtained from Prof. Eric Brown).

NMR Experiments

Solid-state NMR experiments were performed using a three-channel NMR spectrometer (^{1}H = 300 MHz, UnityInova, Varian Inc.) and a 5 mm, three-channel, magic-angle-spinning NMR probe (Varian APEX design). CPMAS experiments were used collected and analyzed for CSA and asymmetric data. CPMAS experiments of LTA and WTA samples were collected with 100,000 scans, 1 s repetition rate, 3000 Hz spinning rate, and a contact time of 1000 μs with ^{1}H decoupling at an RF power level of 50 kHz. $T_{1\rho}$ data was collected under the same condition as above with a contact time array and the spinning speed increased to 9000 Hz for signal-to-noise ratio improvement of adsorbed samples. Drive and bearing gas were provided by dry compressed air. ^{31}P chemical shift data were referenced to an external

standard of 85% phosphoric acid (0 ppm). The temperature was 25 $^{\circ}$C. Data acquisition and analysis were accomplished using VnmrJ 1.1D and the STARS software packages provided by Varian Inc.

Results and Discussion

Biofilms are found in almost all environmental condition and on various surfaces that have drastically different properties (surface charge, surface functional groups, etc.).(*1-13*) It is well known that the first adhesion/chemical interaction that a bacterium has with other objects uses the teichoic acid biopolymer. Although the existence and role of this biopolymer is known for the formation of biofilms there is little to no structural information known for teichoic acids adhered to surfaces. Solid-state NMR is a powerful analytical tool that has been implemented on various systems to study structure and mobility.(*29-35*) Here, we use ^{31}P solid-state NMR experiments to gain information about the chemical environments and molecular motions of LTA and WTA by measuring the changes in their isotropic chemical shift (σ^{iso}), CSA tensors (Δ_{CSA}), asymmetry parameters (η), and rotating frame spin-lattice relaxation ($T_{1\rho}$) rates for LTA and WTA before and after adhesion to various materials.

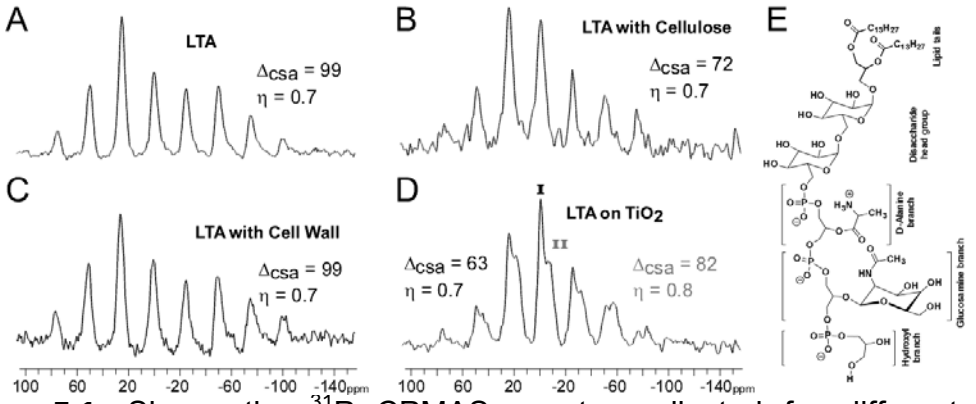

Figure 5.1. Shows the ^{31}P CPMAS spectra collected for different LTA samples. A) shows the ^{31}P CPMAS spectrum collected for pure LTA. This spectrum has a σ^{iso} = 0, Δ_{CSA} = 99, and a η = 0.7. B) shows the ^{31}P CPMAS spectrum collected for LTA adhered to cellulose. This spectrum has a σ^{iso} = 0, Δ_{CSA} = 72, and a η = 0.7. The change in Δ_{CSA} indicates a slight change in the conformation of the LTA backbone. C) shows the ^{31}P CPMAS spectrum collected for LTA adhered to the cell wall. This spectrum has a σ^{iso} = 0, Δ_{CSA} = 99, and a η = 0.7, which is the same as pure LTA indicating that there is no change in the conformation of the LTA backbone. D) shows the ^{31}P CPMAS spectrum collected for LTA adhered to TiO_2. This spectrum has two unique NMR species: species I is assigned to the species that is far away from the TiO_2 surface with observed σ^{iso} = 0, Δ_{CSA} = 63, and a η = 0.7, while species II is assigned to the species that is close to the TiO_2 surface with observed σ^{iso} = -6, Δ_{CSA} = 82, and a η = 0.8. The observation of two unique NMR species and changes in Δ_{CSA} and η indicate that there is a major change in the structure of LTA when adhered to TiO_2. E) show the chemical structure of LTA. All spectra were taken with a delay time of 1s and 100,000 scans. The Δ_{CSA} and η values were achieved using the STARS simulation program provide by Varian.inc

For a bases of comparison, a ^{31}P CPMAS spectrum was collected for pure lipoteichoic acid (LTA) shown in Figure 5.1A. This is a typical ^{31}P CPMAS spectrum with a σ^{iso} (0 ppm) and a series of spinning side bands that map out Δ_{CSA} (99 ppm) and η (0.7) of pure LTA. Subsequent experiments were collected with LTA absorbed on a series of different materials that resulted in deviations from the σ^{iso}, Δ_{CSA}, and η values collected for pure LTA indicating changes in the structural and chemical environments.

The first material studied was titanium dioxide, which is a material commonly used in various implant materials.(*8, 37-39*) Any structural information obtained from the absorption of LTA on TiO_2 may be useful in developing future protocols that would discourage the formation of biofilms (thought to be responsible for most post-surgical infections(*1, 3-13*)) on these implant materials. Figure 5.1 D shows LTA adsorbed onto TiO_2 surface. The most notable difference between pure LTA and LTA on TiO_2 is that there are two observed isotropic phosphorus signals, which have different Δ_{CSA} and η values indicating that the adhesion of LTA onto TiO_2 is heterogeneous causing portions of the LTA backbone to experience a unique phosphorus chemical environment. The isotropic signal that has shifted upfield (-6 ppm) experiences the largest structural change; thus, it is assigned to the portion of teichoic acid chain that is closest to the TiO_2 surface. The downfield species (0 ppm) is assigned to the portion of teichoic acid further away from the TiO_2 surface, as the chemical shift is unchanged. Absorption of LTA onto TiO_2 is also indicated by the change in the rotating frame spin-lattice relaxation ($T_{1\rho}$) rate. Higher molecular mobility is indicated by faster $T_{1\rho}$ rates, being that the more mobile a molecule the faster the $T_{1\rho}$ rate. Pure LTA has a $T_{1\rho}$ of ~3.5 ms while LTA on TiO_2 has a $T_{1\rho}$ of ~30 ms indicating that the molecular motion of the LTA is hampered by adhesion (Table 1). Thus, the significantly slower $T_{1\rho}$ rates for LTA on TiO_2 than that of pure LTA indicates that molecular motion is hampered by adhesion. Each isotropic signal has a unique Δ_{CSA} value indicating a different structural conformation of the LTA

backbone. However, the upfield signal (-6 ppm) has a η value of 0.8; this large η value indicates that there is a higher degree of axial asymmetry, which also indicates that this species is closer to the TiO_2 surface.

With this knowledge we speculate that the alanine groups are responsible for adhesion of LTA onto TiO_2. The reason for this is that the alanine groups carry a positive charge (NH_3^+) while the zeta potential for TiO_2 is negative two (-2). Thus, it is favorable for the alanine (NH_3^+) to be attracted to the TiO_2 surface and for the phosphate groups (PO_4^-) to be repulsed. The rest of the LTA components are neutral and would not contribute to the above charge interactions. This hypothesis agrees well with biological studies that have used mutated bacterial stains. These studies focused on the adhesion properties of bacterial stains that were deficient in alanine containing LTA, which resulted in the inability of LTA to adhere to metal oxide surfaces.(*2*, *13*, *26*) The bacterial adhesion properties were restored by the addition of magnesium, thereby demonstrating the importance of the cationic component in teichoic acids.(*2, 13*) We have no definitive data for the structure of LTA on TiO_2, but it is likely that the phosphates next to the positively charged alanine groups are close to the surface, while the rest of the negatively charged LTA backbone is further away from the surface resulting in an absorbed structure similar to that shown in Figure 5.2 C.

The next material studied is cellulose, since it is found in a variety of medical wrappings (bandages, gaze, medical dressings, etc.). Cellulose is a natural product most commonly found in cotton fibers and is a polymeric

polysaccharide of β-D-glucose sugars. Figure 5.1 B shows the ^{31}P CPMAS spectrum collected for LTA on cellulose. The σ^{iso} is unchanged, but Δ_{CSA} (72 ppm) has changed giving rise to the unique spinning side band pattern observed. The σ^{iso} and the η values did not change indicating that the phosphorus environment is primarily unchanged and not in close proximity to the cellulose; however, the change in Δ_{CSA} indicates that there is an overall change in the orientation of the LTA most likely due to rearrangement of the LTA backbone and functional groups. Absorption of LTA on cellulose is also indicated by the change of the $T_{1\rho}$ rate (~8 ms) shown in Table 5.1. With this knowledge, we speculate that the glucosamine groups are responsible for adhesion of LTA onto cellulose due to their similarity with the cellulose backbone as shown in Figure 5.2 A. As with TiO_2, we have no definitive data for the structure of LTA on cellulose; yet, it is unlikely that the phosphate or alanine groups would be responsible for adhesion as there is no change in the σ^{iso} or η values and cellulose has a neutral charge.

Peptidoglycan (PGN) is the cell wall backbone, void of all other biomolecules, which is a network consisting of a disaccharide sugar backbone that is crossed linked with amino acids. In nature, LTA is in continuous contact with the cell wall making it important to understand these interactions. The addition of pure LTA to PGN resulted in a ^{31}P CPMAS spectrum (Figure 5.1 C) that is identical to pure LTA. However, the observed $T_{1\rho}$ rate (~8 ms) is very similar to that of LTA adhered to cellulose. This data suggest that LTA adheres to PGN in a similar fashion to that of cellulose as

shown in Figure 5.2 B. The lack of spectral changes between pure LTA and LTA - PGN suggest that this binding does not affect the chemical environment of the phosphorus. The reason for this is unclear, but may be due to the differences between cellulose and PGN. PGN is a highly cross-linked polymer where cellulose is not. The cross linking may cause a situation that results in polysaccharides being either less accessible or spaced further apart than they are in cellulose. In this situation, when LTA adheres to cellulose, the glucosamine groups may bunch together which would result in a conformational change of the LTA backbone as seen by the change in Δ_{CSA}. However, if the polysaccharides in PGN are less accessible, then the glucosamine groups may not bunch together; thus, there would be no incentive for the LTA backbone to change conformations. With these experiments, it is not possible to decisively determine the structure of these binding modes, but future studies will focus on this issue.

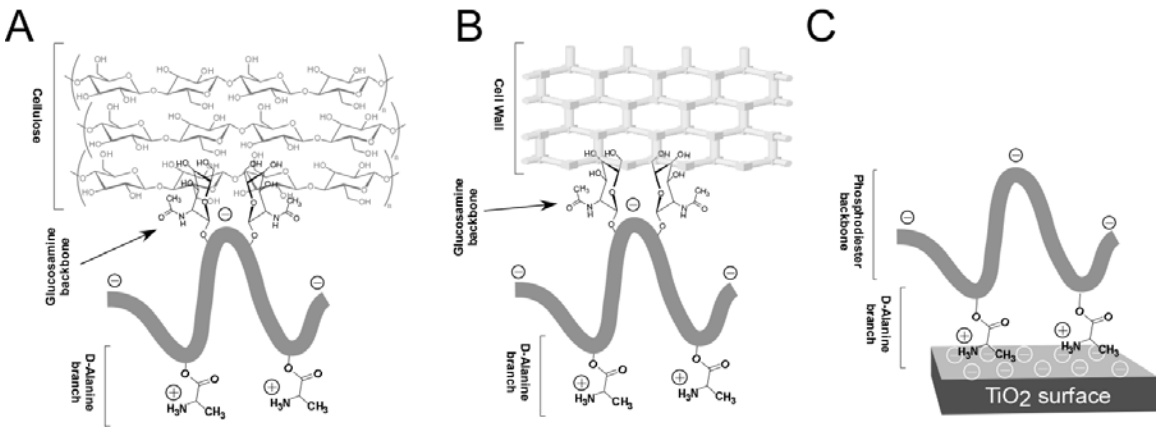

Figure 5.2. Shows the proposed adhesion interaction for LTA onto different materials. A) Depicts the glucosamine group adhering to cellulose through hydrogen bonding. B) Depicts the glucosamine group adhering to the cell wall through hydrogen bonding. C) Depicts the alanine groups adhering to the TiO_2 surface through electrostatic interactions resulting in some of the backbone phosphates being in close proximity to the surface and other further away from the surface.

In bacteria, the cell wall is always present when LTA binds to any surface; thus, we took the sample from Figure 5.1C (LTA-PGN) and absorbed it onto TiO_2. The ^{31}P CPMAS spectrum for this sample (Figure 5.3B) was similar to that obtained for LTA on TiO_2 (Figure 5.3A), but yielded a unique set of CSA tensors and asymmetric parameters, suggesting a different phosphorus chemical environment than seen in the previous samples. The isotropic peaks observed have the same shifts as previously seen with LTA on TiO_2 indicating a similar heterogeneous adhesion. Although the samples were dried using the same conditions as LTA on TiO_2, both species have faster $T_{1\rho}$ rates (species I ~8 and species II ~10). The only apparent cause for this increase in $T_{1\rho}$ rates is the presence of water (hydrated); thus, this sample was submitted to further vacuum drying. This resulted in a similar spectrum; however, there were evident changes in the spectrum for LTA-PGN

on TiO_2 (Figure 5.3C) resulting in different Δ_{CSA} and η values. These changes suggest a slight change in the chemical structure of the sample, most likely due to the removal of water, but still exhibited an unchanged $T_{1\rho}$ rate (species I ~8 and species II ~10). This fast $T_{1\rho}$ rate indicates that there is still some water present (partially hydrated), which means that the change in chemical structure may be due to the LTA backbone partially collapsing around the remaining waters of hydration. Thus, this sample was submitted to an addition 4 days of vacuum drying that resulted in a ^{31}P CPMAS spectrum with only 1 isotropic peak (Figure 5.3D). The isotropic peak was observed at –6 ppm, which was the same chemical shift as for the surface bound portion of LTA with similar Δ_{CSA} and η values. Figure 5.3E shows an overlay of dehydrated LTA on TiO_2 and dehydrated LTA-PGN on TiO_2. This helps to show the similarity between the species that are in close proximity to the surface and reinforces their NMR assignments.

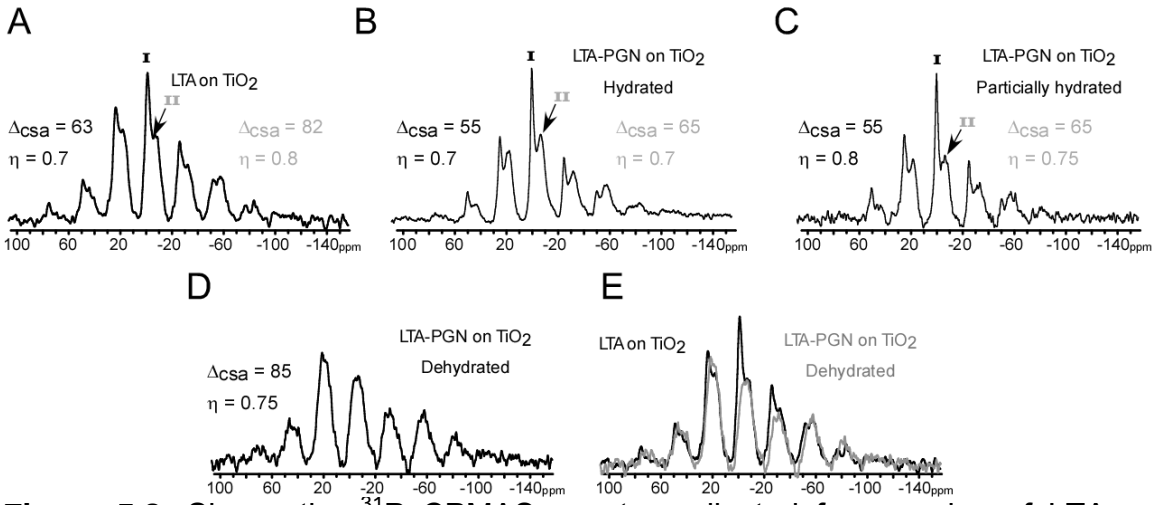

Figure 5.3. Shows the ^{31}P CPMAS spectra collected for samples of LTA adhered to both the cell wall (PGN) and TiO_2 with different amounts of waters of hydration. A) shows the ^{31}P CPMAS spectrum from Figure 5.1 D (LTA-TiO_2) for comparison purposes. B) shows the ^{31}P CPMAS spectrum collected for LTA adhered to PGN and TiO_2 with the highest water content (LTA-PGN on TiO_2 hydrated). This spectrum has the same σ^{iso} values as LTA-TiO_2 (0 for species I and –6 for species II), but different Δ_{CSA} (55 for species I and 65 for species II) and η (0.8 for species I and II) values. The change in resolution, Δ_{CSA} and η values indicate a slight change in the conformation of the LTA backbone from LTA-TiO_2. C) shows the ^{31}P CPMAS spectrum collected for LTA adhered to PGN and TiO_2 with lower water content than LTA-PGN on TiO_2 hydrated. This spectrum also has the same σ^{iso} values as LTA-TiO_2 (0 for species I and –6 for species II), but different Δ_{CSA} (55 for species I and 65 for species II) and η (0.7 for species I and 0.75 for species II) values than either LTA on TiO_2 or LTA-PGN on TiO_2 hydrated. The changes in resolution and η values indicate a slight change in the conformation of the LTA backbone from LTA on TiO_2 and LTA-PGN on TiO_2 hydrated. D) shows the ^{31}P CPMAS spectrum collected for LTA adhered to PGN and TiO_2 dehydrated. This spectrum only has NMR species with observed σ^{iso} = -6, Δ_{CSA} = 85, and a η = 0.75, which indicates that all phosphates in the LTA backbone are now in close proximity to the surface. This indicates that there is a major change in the structure of LTA when the waters of hydration are removed. E) show the LTA-PGN on TiO_2 dehydrated spectrum (gray) with the LTA on TiO_2 (black) superimposed to demonstrate the similarity between species II and the dehydrated species. All spectra were taken with a delay time of 1s and 100,000 scans. The Δ_{CSA} and η values were achieved using the STARS simulation program provide by Varian.inc

This demonstrates that LTA can simultaneously adhere to both PGN and TiO_2, but the adhesion of LTA onto PGN prior to TiO_2 adhesion changes the phosphodiester backbone structure in a manner that traps water. This is not observed for LTA on TiO_2; thus, this must be a product of the simultaneous adhesion of PGN and TiO_2. Why is this phenomenon not observed with LTA on TiO_2, and how does the LTA structure change? These questions are answered by revising or adding to the proposed structure shown in Figure 5.2C. Since, the surface of TiO_2 has a Zeta potential of –2 we hypothesize that the portions of LTA with alanine (+1) are attracted to the surface while the phosphate groups (-1) are repelled from the surface. The separation between like charges creates a void to be filled. In the LTA on TiO_2 we believe that the glucosamine groups rotate and point toward the surface, thereby filling the void. This would create steric-hindrance between the phosphodiester backbone and the surface preventing the collapse of the backbone, thus maintaining charge separation as shown in Figure 5.4 A. However, since LTA uses its glucosamine groups to adhere to PGN they are no longer available to prevent the collapsing of the phosphodiester backbone resulting in water being trapped in the void between the backbone and the surface as shown in Figure 5.4B. As these waters of hydration are forcefully remove through vacuum drying the backbone slowly collapses (Figure 5.4C) until no more water is present resulting in all of the LTA backbone being in close proximity with the surface (Figure 5.4D). This also explains why it is so much harder to completely dry this sample.

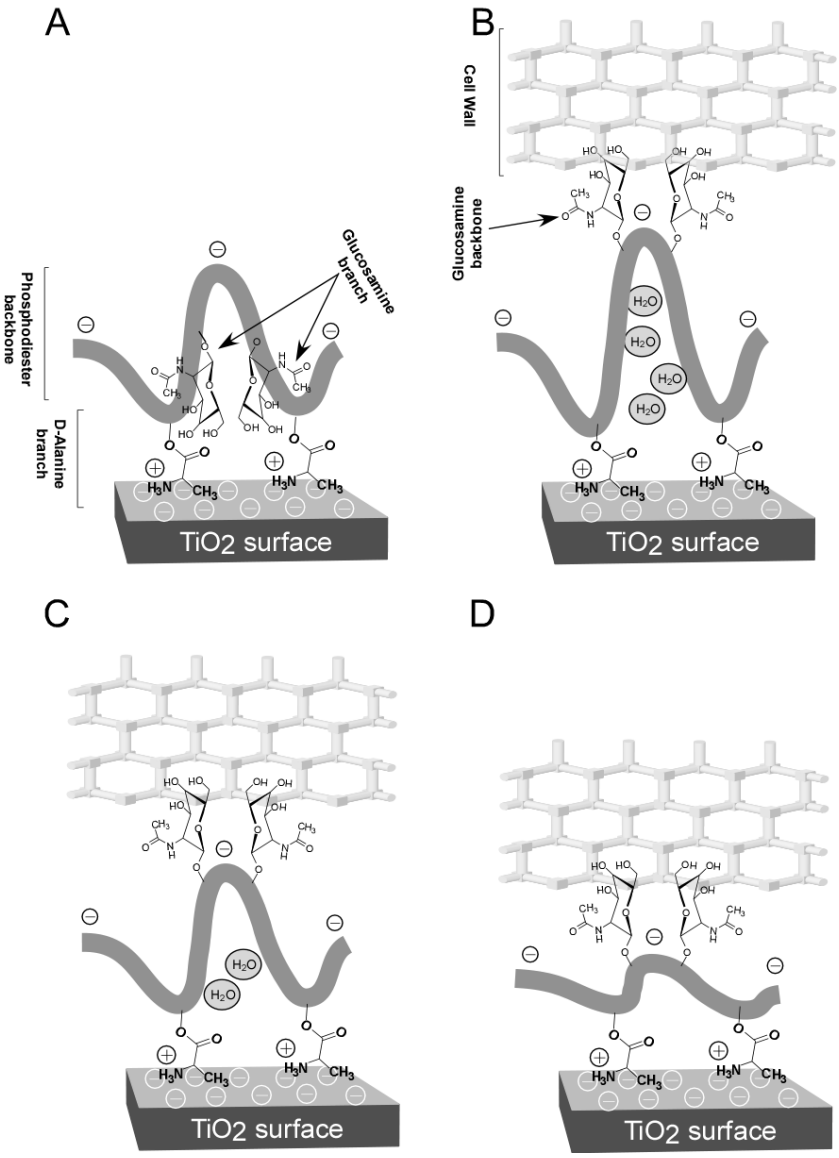

Figure 5.4. Illustrates proposed adhesion structures for LTA on TiO_2 and for LTA-PGN on TiO_2 as the waters of hydration are removed. A) shows a revised adhesion model from Figure 5.2 C. From the LTA-PGN on TiO2 data it has become evident that glucosamine groups are important to separate part of the phosphodiester backbone from the surface. Thus, we believe that the glucosamine are rotated toward the surface and prevents the phosphodiester backbone from collapsing onto the surface through steric-hindrance when dehydrated. B-D) demonstrate that due to the adhesion interaction of the glucosamine groups to the cell wall they are not available to prevent the phosphodiester backbone from collapsing onto the surface. This results in the trapping of water between the phosphodiester backbone and the collapse of the phosphodiester backbone onto the surface with dehydration.

As previously stated, it is well known that LTA extends away from the cell wall and is the primary adhesion molecule for biofilm formation.(*2, 7*) The importance of WTA for bacterial adhesion is less known, but some studies suggest that WTA is primarily responsible for biofilm formation on nasal epithelial cells.(*5, 11*) Figures 5.5 B-E show a series of collected ^{31}P CPMAS spectra of different WTA samples. These spectra allow a direct comparison between the affects that adhesion has on the teichoic acid chain in WTA. To begin this comparison it is necessary to compare WTA, wall teichoic acid that is in the cell wall matrix, with LTA (Figures 5.5 A & B). Figures 5.5 A & B are exactly the same indicating that there is no difference in the phosphate structure within the cell wall matrix, but the $T_{1\rho}$ rate for WTA is dramatically longer (~83 ms) than that of pure LTA (~3.5). This indicates that the molecular motions between the two are very different. The dynamics of WTA are greatly hampered perhaps due to both steric interaction of the cell wall and an adhesion interaction of the functional groups with the cell wall, but we are unable to differentiate between the two possibilities at this time. From these results it seems likely that WTA is completely contained within the cell wall in this lyophilized powder (Figure 5.6A).

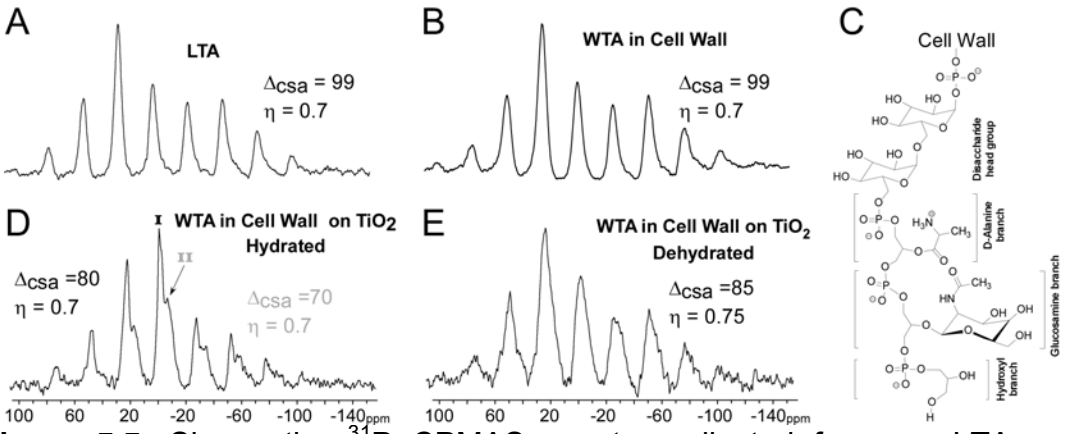

Figure 5.5. Shows the ^{31}P CPMAS spectra collected for pure LTA and different WTA samples. A) shows the ^{31}P CPMAS spectrum collected for pure LTA. This spectrum has a σ^{iso} = 0, Δ_{CSA} = 99, and a η = 0.7. B) shows the ^{31}P CPMAS spectrum collected for WTA. This spectrum has a σ^{iso} = 0, Δ_{CSA} = 99, and a η = 0.7. This spectrum is identical to pure LTA indicating that LTA and WTA in the cell wall have the same structure. C) shows the chemical structure for WTA. D) shows the ^{31}P CPMAS spectrum collected for WTA adhered to TiO_2. This spectrum has two unique NMR species: species I is assigned to the species that is far away from the TiO_2 surface with observed σ^{iso} = 0, Δ_{CSA} = 80, and a η = 0.7, while species II is assigned to the species that is close to the TiO_2 surface with observed σ^{iso} = -6, Δ_{CSA} = 70, and a η = 0.7. This sample has almost identical NMR spectrum as the LTA-PGN on TiO_2 hydrate sample in Figure 5.3 B. E) shows the ^{31}P CPMAS spectrum collected for WTA adhered to TiO_2 dehydrated. This spectrum only has NMR species with observed σ^{iso} = -6, Δ_{CSA} = 85, and a η = 0.75, which indicates that all phosphates in the WTA backbone are now in close proximity to the surface. This sample has almost identical NMR spectrum as the LTA-PGN on TiO_2 hydrate sample in Figure 5.3 D. The similarities between LTA-PGN and WTA adhered to TiO_2 indicates that they have the same adhesion structure and interactions. All spectra were taken with a delay time of 1s and 100,000 scans. The Δ_{CSA} and η values were achieved using the STARS simulation program provide by Varian.inc

It has been shown that the formation of biofilms in nasal cavities is due to WTA adhering to nasal epithelial cells, however the adhesion role of WTA is not well defined. Thus, we adhered WTA to TiO_2 and collected ^{31}P CPMAS data. As mentioned above, lipoteichoic acid heterogeneously adheres to TiO_2 resulting in two resolved NMR signals. We have also adhered WTA to TiO_2 to

assist in understanding whether WTA can extend out past the cell wall far enough to adhere materials. If WTA extends out past the cell wall and plays an active role in the adhesion properties of bacteria, then we should observe a similar NMR spectrum for heterogeneous adhesion. Indeed, there are two NMR signals observed at 0ppm and –6ppm with Δ_{CSA} and η values that resemble those of the hydrated LTA-PGN on TiO_2 (Figure 5.5D). This means that the glucosamine groups of WTA are also adhered to the cell wall and that there are waters of hydration trapped between the surface and phosphodiester backbone (Figure 5.6B), as seen with hydrated LTA-PGN on TiO_2. With additional vacuum drying the spectrum changed and was identical to dehydrated LTA-PGN on TiO_2 (Figure 5.5E). The observed $T_{1\rho}$ rate for dehydrated WTA was ~ 14 ms, which is slightly longer that than of dehydrated LTA-PGN on TiO2 (~ 8). The difference between these two samples is probably due to an immobile portion of WTA that is trapped within the cell wall (Figure 5.6C). The very long $T_{1\rho}$ rate observed for the lyophilized powder indicates that almost all of the WTA is inside the cell wall initially, but the ability of WTA to adhere to TiO_2 and trap waters of hydration indicates that WTA significantly extends out past the cell wall in order to adhere to materials.

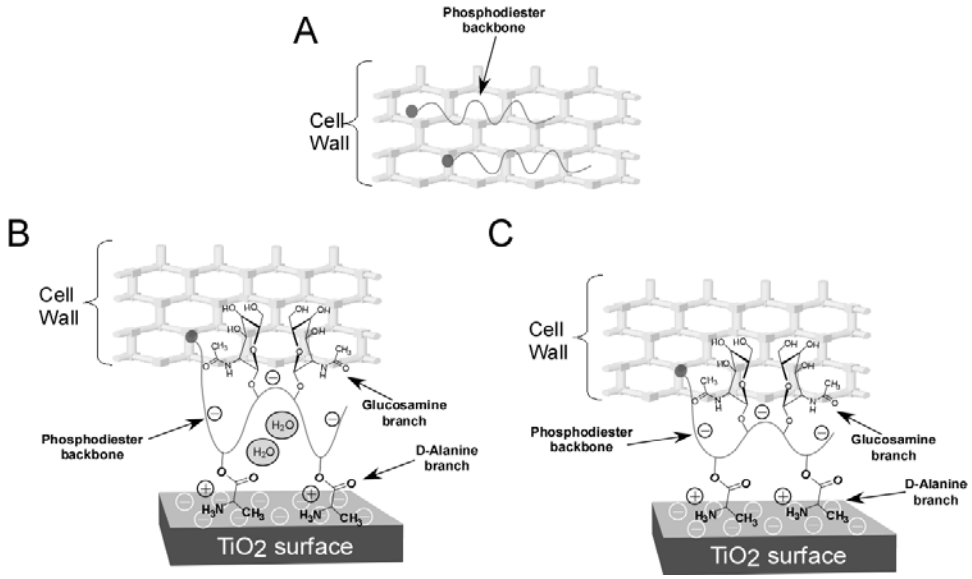

Figure 5.6. Illustrates proposed structures for unbound WTA and for WTA on TiO_2 as the waters of hydration are removed. A) shows that WTA primarily resides inside to the cell wall matrix as suggested by the long $T_{1\rho}$ relaxation rates. B & C) demonstrate that due to the adhesion interaction of the glucosamine groups to the cell wall they are not available to prevent the phosphodiester backbone from collapsing onto the surface. This results in the trapping of water between the phosphodiester backbone and the collapse of the phosphodiester backbone onto the surface with dehydration, very similar to LTA-PGN on TiO_2.

Table 1. $T_{1\rho}$ Rates of Teichoic Acid Adhered to Various Materials	
Sample	**$T_{1\rho}$(ms)**
pure LTA	~ 3.5
LTA on TiO_2 Species I	~ 30.3
LTA on TiO_2 Species II	~ 31.5
LTA - cellulose	~ 8.3
LTA - PGN	~ 8.5
LTA - PGN on TiO_2 Hydrated Species I	~ 8
LTA - PGN on TiO_2 Hydrated Species II	~ 10
LTA - PGN on TiO_2 Partially Hydrated Species I	~ 8
LTA - PGN on TiO_2 Partially Hydrated Species II	~ 10
LTA - PGN on TiO2 Dehydrated	~ 8.5
WTA in Cell Wall	~ 83.3
WTA in Cell Wall on TiO_2 Dehydrated	~ 14.3

Table 2. $T_{1\rho}$ Rates of Teichoic Acid at different field strengths	
Sample	**$T_{1\rho}$(ms)**
pure LTA at 300 MHz	~ 3.5
LTA on TiO_2 Species I at 300 MHz	~ 30.3
LTA on TiO_2 Species II at 300 MHz	~ 31.5
pure LTA at 600 MHz	~ 1
LTA on TiO_2 Species I at 600 MHz	~ 5
LTA on TiO_2 Species II at 600 MHz	~ 5

Understanding the mechanism of relaxation for the $T_{1\rho}$ rates can reveal structural information. $T_{1\rho}$ relaxation occurs through two mechanisms; dipolar interactions and chemical shift anisotropy (CSA). The dipole - dipole relaxation mechanism is independent of the external magnetic field strength; therefore, the relaxation rate remains the same regardless of the external magnetic field strength. However, the CSA relaxation mechanism is dependent on the external magnetic field strength; therefore, the relaxation rate changes when the external magnetic field strength changes. Thus, the collection of $T_{1\rho}$ rates at different external magnetic field strengths will aid in the determination of the primary relaxation rate mechanisms; thereby providing structural insights into these different samples (Table 2).

At a magnetic field strength of 300 MHz the $T_{1\rho}$ rate for pure LTA is ~3.5 ms, but at 600 MHz the $T_{1\rho}$ rate increases to ~1 ms. However, the $T_{1\rho}$

rate for LTA on TiO_2 is ~30 ms at a magnetic field strength of 300 MHz and drastically increases to ~5 ms at a magnetic field strength of 600 MHz. The $T_{1\rho}$ rate for LTA on TiO_2 is 6 times faster at a magnetic field strength of 600 MHz than it is at 300 MHz. Since the $T_{1\rho}$ rate for LTA on TiO_2 significantly increases with an increase in magnetic field strength increase, we assign the primary relaxation mechanism to CSA relaxation. However, assignment of the relaxation mechanism for the pure LTA is not as simple. The $T_{1\rho}$ rate for pure LTA is only 3.5 times faster at a magnetic field strength of 600 MHz than at 300 MHz. Thus, it is more likely that relaxation mechanism is a mixture of dipolar interactions and CSA. If this were not the case the increase in relaxation rates would be the same factor for both samples.

Previous literature reports that pure LTA forms contact ion pairs between the alanine and phosphate groups.(*13*) Thus, the protons of the NH_3^+ group would be close to phosphate group causing strong dipolar interactions and increased relaxation (Figure 5.7 A). There are several other phosphate groups that are not close to the alanine groups; therefore, they not have strong dipolar interaction with protons and relax through the CSA relaxation mechanism. The removal of the dipolar interaction relaxation mechanism when LTA is adhered to TiO_2 supports the proposed chemical structure from our CPMAS NMR data and previous biological studies, which suggests that the alanine groups are adhered to the surface.(*2, 13, 26*) The removal of the dipolar interaction is caused by the contact ion pair being broken when the alanine group adheres to the surface, which results in the

lengthening in distract between the NH_3^+ and phosphate groups as shown in Figure 5.7 B.

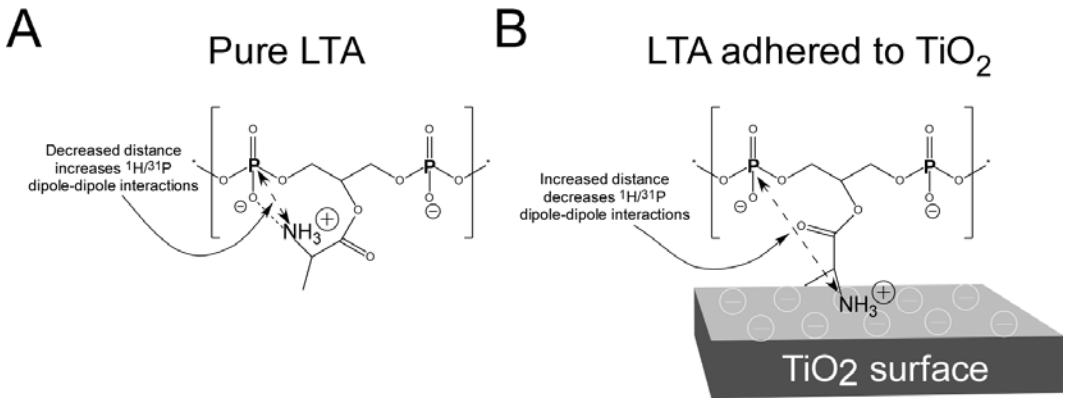

Figure 5.7. Demonstrates the changes in dipolar interaction between NH_3^+ and PO_4^- groups when LTA is adhered onto TiO_2. A) shows that the contact ion pair present in pure LTA increases the dipolar interaction between the phosphate group and the NH_3^+ resulting in mixed relaxation mechanisms. B) shows that the contact ion pair is broken when LTA is adhered to TiO_2 resulting in a decreased dipolar interaction and a relaxation mechanism that is primarily CSA relaxation.

Conclusions

We have shown through the use of CPMAS NMR that there are unique structures for pure LTA and LTA adhered to TiO_2, cellulose, and PGN. Our hypothesis is that these unique adhesion structures are brought about due to the diversity of available functional groups. Our proposed structures have LTA adhering to cellulose and PGN with the glucosamine groups and to TiO_2 with the alanine groups. $T_{1\rho}$ rates were used to confirm adhesion through hampered (longer $T_{1\rho}$ rates) molecular motion.

We have also shown that the simultaneous adhesion of LTA to PGN and TiO_2 (LTA-PGN on TiO_2) resulted in an adhesion structure that facilitated

absorbed water. We propose that this is prevented in LTA on TiO_2 due to the steric-hindrance of the glucosamine braches. However, these groups are also used to adhere LTA to PGN; thus, they are not able to prevent the absorption of water.

The CPMAS signal for pure LTA and WTA were identical, but WTA has a very long $T_{1\rho}$ rate indicating that WTA has the same structure inside the cell wall as pure LTA. The long $T_{1\rho}$ rate suggests that as a lyophilized powder WTA is most likely completely contained within the cell wall. However, it exhibits the same heterogeneous adhesion on TiO2 as LTA and exhibits the same water dependence as LTA-PGN. This indicates that WTA has the same interaction with the cell wall as LTA and that it has the ability to extend out past the cell wall when in the presence of other materials.

We were also able to identify the relaxation mechanisms for pure LTA and LTA on TiO_2. The latter was found to be primarily CSA relaxation, while the former was found to be a mixture of both dipolar interaction and CSA relaxations. The difference between these two is that the contact ion pair present in pure LTA is broken in LTA on TiO_2 in order for the NH_3^+ groups to adhere to the TiO_2 surface.

So far all structural characterizations are mostly speculation with little definitive data. In order to improve our understanding of the structure of teichoic acids adhered to various materials, future studies will employ the use of REDOR experiments for distance measurements (through isotopic labels)

and comparison with simulated NMR spectra from quantum mechanical models of these systems.

Section 2: Phosphorus Solid-State NMR and *Ab Initio* Studies of the Binding Motif for Lipoteichoic Acid Bound to Magnesium

Introduction

LTA and WTA have both been associated with the transportation of nutrients and ions.(*13*) Teichoic acids can extend away from the cell and are one of the first cellular components to come in contact with other cells, molecules, nutrients, and surfaces. The cell wall of gram-positive bacteria attracts metal cations because of its net negative charge, which is largely due to the phosphate groups of teichoic acids, although there is a contribution from anionic amino acids in the peptide stems and cross-links.

At pH 7 the amine group of the alanine braches are cationic (NH_3^+), and the phosphate groups are anionic. Thus, teichoic acid binds metals due to its anionic phosphate groups. However, it is important to note that the alanine and phosphate groups are thought to form an ion pair, which prevents these phosphates from participating in metal binding. The hindering of Mg^{2+} by ion pairing was demonstrated by an 60% increase in Mg^{2+} binding when D-Alanine was removed from the teichoic acids.(*40*) This lead to two different proposed binding structures of Mg^{2+} with the phosphates of the teichoic acid backbone: Mg^{2+} ion binding in a monodentate fashion with either a signal phosphate or acting as a bridging atom between two phosphates.(*41*) However, removal of the teichoic acid polymer from *S. aureus* did not

completely eliminate Mg^{2+} binding, demonstrating that the peptidoglycan also plays a significant role.(*42*)

The uptake of Mg^{2+} ions is vital for bacterial survival, which is demonstrated by the replacement of Mg^{2+} with Ca^{2+} resulting in bacterial death. The need for teichoic acid to associate and assist with the migration of Mg^{2+} through the cell wall is demonstrated by studies of bacteria grown in low Mg^{2+} concentrations. These bacteria showed a significant increases in the amount of teichoic acid that was produced in the cell wall, which resulted in a higher affinity for Mg^{2+}.(*43, 44*) Bacterial strains with teichoic acid removed have shown a decreased affinity for Mg^{2+}, K^{+}, and Na^{+} and an inability to bindCa^{2+}.(*42*) This demonstrates that both teichoic acid and peptidoglycan are responsible for the binding of Mg^{2+}, K^{+}, and Na^{+}, but teichoic acid is solely responsible for the binding of Ca^{2+}. Although the importance of Mg^{2+} to the survival of the bacterium has been well documented,(*43, 44*) there is very little structural information available for the binding molecules and transport mechanisms. This lack of structural information is primarily due to these materials being unsuitable for x-ray crystallography techniques (unable to obtain single crystals). However, solid-state NMR is ideally suited for gaining detailed molecular structure information from these amorphous materials.

It has been previously demonstrated that simulated NMR spectra of energy minimized structures can be a very effective method of determining adhesion structures.(*33*) Thus, we bound LTA to $MgCl_2$ and determined the binding motif through comparison of experimental spectra and simulated

spectra from energy minimized structures. The comparisons between experimental and quantum mechanically generated NMR spectra supports a bidentate Mg^{2+} binding structure instead of the previously accepted monodentate model.(*41*)

Experimental

Sample preparation

Staphylococcus aureus lipoteichoic acid (LTA) was purchased from InvivoGen as a lyophilized powder. LTA was dissolved in a 20 mM $MgCl_2$ (obtained from Sigma-Aldrich) solution of double distilled water followed by lyophilization.

NMR Experiments

Solid-state NMR experiments were performed using a three-channel NMR spectrometer (^1H = 300 MHz, UnityInova, Varian,Inc.) and a 5 mm, three-channel, magic-angle-spinning NMR probe (Varian APEX design). CPMAS experiments collected were analyzed for CSA and asymmetric data. CPMAS experiments of LTA – $MgCl_2$ samples were collected with 100,000 scans, 1 s repetition rate, 3000 Hz spinning rate, and a contact time of 1000 μs with ^1H decoupling at an RF power level of 50 kHz. Drive and bearing gas were provided by dry compressed air. ^{31}P chemical shift data are referenced

to an external standard of 85% phosphoric acid (0 ppm). The temperature was 25 °C. Data acquisition and analysis were accomplished using VnmrJ 1.1D and the STARS software packages provided by Varian,Inc.

Computational Modeling

All computational data were collected with a multiple node cluster running Gaussian03 and Guasview03. Geometry optimizations were ran at the Hartree-Fock theoretical level and 6-31+G (d) basis set, while magnetic shielding tensors were calculated through the GIAO method[45] at a Hartree-Fock theoretical level and a 6-311++G (2d, 2p) basis set for the optimized structures. Isotropic chemical shift (σ^{iso}), chemical shift tensor (Δ_{CSA}), and asymmetry parameter (η) were calculated with following equations.

$$| \sigma^{zz} - \sigma^{iso} | \geq | \sigma^{xx} - \sigma^{iso} | \geq | \sigma^{yy} - \sigma^{iso} |$$

$$\sigma^{iso} = (\sigma^{xx} + \sigma^{yy} + \sigma^{zz})/3$$

$$\Delta_{CSA} = \sigma^{zz} - \sigma^{iso}$$

$$\eta = (\sigma^{yy} - \sigma^{xx})/(\sigma^{zz} - \sigma^{iso})$$

The σ^{iso}, Δ_{CSA}, and η parameters were then entered into the STARS program, provide by Varian,Inc. thereby generating the simulated spectrum.

Results and Discussion

Gram-positive bacteria rely on peptidoglycan and teichoic acids to bind metals from extracellular fluids.(*13*) After binding, metals move to the cell

membrane where they enter the cytoplasm and are used for numerous biochemical processes. Interrupting metal transport in the cell wall is an intriguing antibiotic target. Teichoic acid is nearly 100% responsible for Ca^{2+} uptake whereas it contributes 50% for K^{+}, Na^{+} and Mg^{2+} binding. The interaction of teichoic acids with metals are thought to facilitate the delivery of nutrients to transporters in the cytoplasmic membrane, but occurs through an unknown mechanism. Decades of research have focused on this issue, but have yet to reveal the basic chemical interactions that enable metal binding. This missing knowledge is essential for deciphering bacterial virulence, formulating antibiotic targets, and advancing basic knowledge of bacterial biochemistry.

The main obstacle is the lack of structural data needed to create a molecular scale mechanism. Although the macroscopic binding trends have been characterized, structural biology was impossible due to the lack of samples for X-ray crystallography and the inability to use solution-state NMR. Our solid-state NMR methods are ideally suited to this finally address the metal binding mechanism and our data will be a significant advance in the field of metal binding.

In the early 1970s, X-ray photoelectron spectroscopy was used with samples of teichoic acids bound to Mg^{2+} ions in order to decipher the binding mode of the Mg^{2+} atom. This tool measures the energy of electrons ejected from the Mg^{2+} atom. Because the electrons are also in chemical bonds, the electronic energy of the Mg^{2+} interactions to teichoic acid is altered according

to the binding mode. Their results were interpreted as monodentate binding by a single oxygen of the phosphate group (Chapter 4 Figure 4.3).(*46*) However, we have used solid-state NMR spectroscopy and computational chemistry to demonstrate that Mg^{2+} binding is a bidentate process; thus, refuting the previous monodentate models.

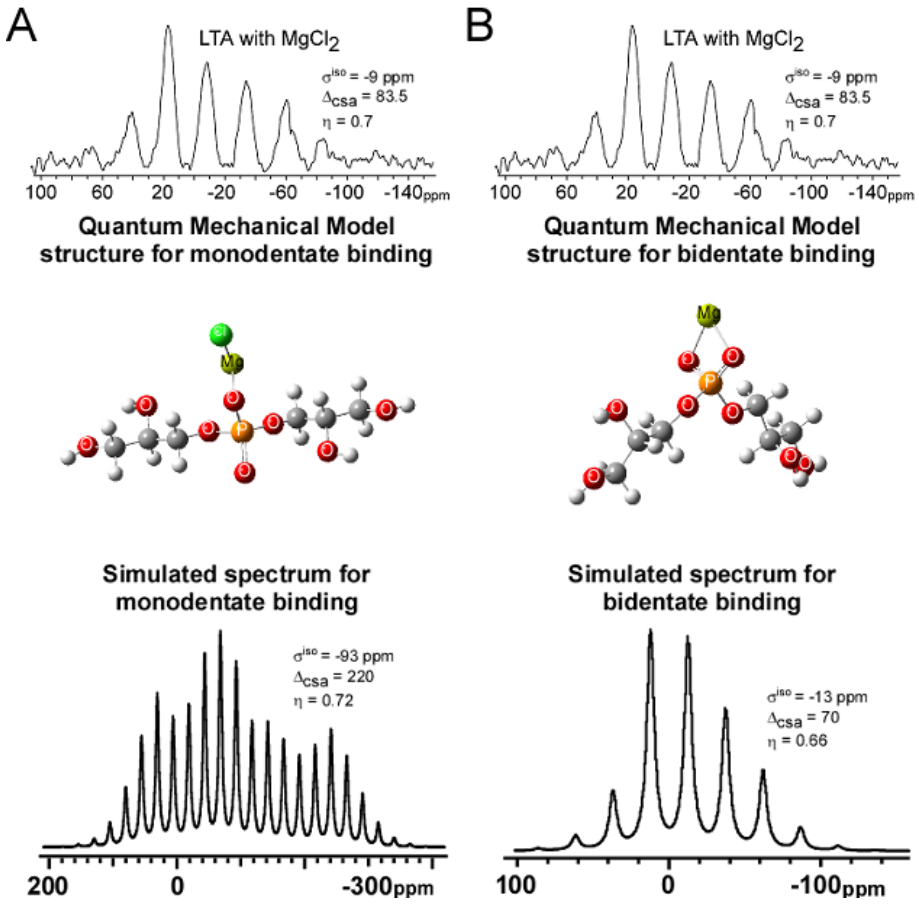

Figure 5.8. ^{31}P CPMAS spectra of LTA bound with $MgCl_2$ as lyophilized powders and simulated NMR spectra from energy minimized structures. A) The top shows the ^{31}P CPMAS NMR spectrum for LTA bound with $MgCl_2$. The middle shows the energy-minimized structure from quantum mechanical calculation for a LTA model compound that experiences monodentate binding with Mg^{2+}. The bottom shows the NMR spectrum that is simulated from this energy-minimized structure (note that due to the large Δ_{CSA} value this spectrum is shown with a large ppm scale). B) The top shows the ^{31}P CPMAS NMR spectrum for LTA bound with $MgCl_2$. The middle shows the energy-minimized structure from quantum mechanical calculation for a LTA model compound that experiences bidentate binding with Mg^{2+}. The bottom shows the NMR spectrum that is simulated from the energy-minimized structure. Comparison with experimental Δ_{CSA}, η, and σ^{iso} values show that Mg^{2+} binding is bidentate. Calculations were performed with Gaussian03 software. Structure minimizations were carried out at the HF/6-31+G (d) basis set while the NMR parameters (CSA (Δ_{CSA}), asymmetry parameter (η), and the isotropic chemical shift (σ^{iso})) were calculated at the HF/6-311++G (2d,2p) level using the GIAO method.

Changes in ^{31}P NMR spectra lead to the observation that Mg^{2+} binding occurs with LTA, and that binding involves the phosphate groups. The binding of Mg^{2+} to LTA is indicated by line broadening (~ double the line-width of pure LTA) and an upfield shift of the isotropic chemical shift to -8.5 ppm (top of Figures 5.8A and 5.8B). The upfield shift observed for Mg^{2+} binding to LTA is due to the increased shielding of the phosphorus atoms caused by the strong interaction of the magnesium ion with the LTA backbone. It has been well established that coordination of cations causes upfield chemical shifts, as demonstrated by PEO:LiTf NMR signals.(*47, 48*) Besides the change in isotropic chemical shift, Mg^{2+} binding is also indicated by a change in the spinning side band pattern. The spinning sideband intensities map out the magnitude of the chemical shift anisotropy (CSA tensors), which describes electron density around the nucleus.

σ^{xx}, σ^{yy}, and σ^{zz} are vectors that describe the CSA tensors; thus, solving these values can be useful in describing structural changes. Since, it is well known that σ^{zz} lies along the P=O bond this value is used to describe changes in the P=O band length.(*49, 50*) Using the STARS simulation program provide by Varian,Inc., we found that Δ_{CSA} = 83.5. The equation STARS uses to calculate Δ_{CSA} is $\Delta_{CSA} = \sigma^{zz} - \sigma^{iso}$; thus, we obtain the σ^{zz} values by rearranging this equation ($\Delta_{CSA} + \sigma^{iso} = \sigma^{zz}$). With this methodology, pure teichoic acid gives a σ^{zz} = 99 ppm while LTA/Mg^{2+} gives a σ^{zz} = 92.5 ppm. The reduction in σ^{zz} is caused by a lengthening of the P=O bond (~ 0.05 Å)(*49, 50*) as it participates in the Mg^{2+} coordination chemistry. A lack of

change in the P=O bond would result in an unchanged σ^{zz} value, but the change in the σ^{zz} value indicates participation of the P=O bond. The participation of the P=O bond in binding Mg^{2+} suggests that the binding structure may be bidentate as the $P\text{-}O^-$ is expected to coordinate with cations. However, a bidentate binding mode disagrees with the model proposed by Baddiley. To clarify the binding structure of Mg^{2+} to LTA quantum mechanical models were used to simulate the NMR spectra for monodentate and bidentate binding structures.

One model was created using the supposed Mg^{2+} binding configuration of a single phosphate oxygen and a Cl^- anion. This is the model Baddiley proposed based on X-ray photoelectron spectroscopy (Figure 5.8 A).(*46*) From the energy minimized structure, the CSA (Δ_{CSA}), asymmetry parameter (η), and the isotropic chemical shift (σ^{iso}) were found. After comparison of theoretical σ^{iso} and Δ_{CSA} parameters to experimental data (Figures 5.8A), it is obvious that enormous differences exist. This leads to the conclusion that the Baddiley model is incorrect for lyophilized $MgCl_2$ teichoic acid. The change observed in the σ^{zz} value prompted us to create a bidentate model. The CSA (Δ_{CSA}), asymmetry parameter (η), and the isotropic chemical shift (σ^{iso}) values are much closer to the experimental data than the Baddiley model (Figure 5.8B). Thus, our conclusion is that Mg^{2+} binding occurs in a bidentate fashion, contradicting the Baddiley model. Additionally, bidentate binding has been previously reported by Mueller et al. for damp adhered to alumina using ^{31}P CPMAS, REDOR, and Gaussian03 calculations.(*33*)

Additional calculations are underway with added water molecules to model the effects of hydration, which is important because Mg^{2+} has an octahedral coordination symmetry. For the bidentate model, 4 waters are needed to accurately reflect the coordination chemistry. Likewise, larger calculations are underway to model the role of D-Ala, NAG, and glycerol in the metal binding geometry.

Conclusions

LTA was mixed with $MgCl_2$, which results in two possible coordination schemes monodentate and bidentate. In order to determine the correct binding motif we compared our experimentally obtained data with simulated NMR spectra from our energy minimized structure. We found that there was very good agreement between our experimental spectra and the simulated spectra for bidentate and very poor agreement with the monodentate model. It is also well known that the σ^{zz} vector runs through the P=O bond, resulting in the ability to characterize the participation of the P=O in the binding of Mg^{2+} cations. Since our simulated NMR data for the bidentate binding model agreed well with our experimental data and the observed change in the σ^{zz} value we have shown that Mg^{2+} cation binds in a bidentate manner. This disproves the prior binding model for Mg^{2+} and can provide insights into cationic migration through the cell wall.

References

1. R. M. Donlan, J. W. Costerton, *Clin. Microb. Rev.* **15**, 167 (2002).
2. M. Gross, S. E. Cramton, F. Gotz, A. Peschel, *Infect. Immun.* **69**, 3423 (2001).
3. K. K. Jefferson, *FEMS Microbiol. Lett.* **236**, 163 (2004).
4. L. Hall-Stoodley, J. W. Costerton, P. St, *Nat. Rev. Microbiol.* **2**, 95 (2004).
5. C. Weidenmaier *et al.*, *Nature Medicine* **10**, 243 (2004).
6. C. Thiemermann, *Microbes Infect* **4**, 927 (2002).
7. F. Gotz, *Mol. Microbiol.* **43**, 367 (2002).
8. F. H. Jones, *Surface Science Reports* **42**, 75 (2001).
9. J. W. Costerton, P. S. Stewart, E. P. Greenberg, *Science* **284**, 1318 (1999).
10. F. Gotz, *Curr. Opin. Microbiol.* **7**, 477 (2004).
11. C. Weidenmaier *et al.*, *J. Infect. Dis.* **191**, 1771 (2005).
12. I. Ginsburg, *Lancet Infect. Dis.* **2**, 171 (2002).
13. F. C. Neuhaus, J. Baddiley, *Microbiol. Mol. Biol. Rev.* **67**, 686 (2003).
14. N. V. Potekhina, A. S. Shashkov, L. I. Evtushenko, S. N. Senchenkova, I. B. Naumova, *Carbohyd. Res.* **338**, 2745 (2003).
15. B. F. Volkman *et al.*, *Biochemistry* **40**, 7964 (2001).
16. W. Fischer, T. Behr, R. Hartmann, J. Peter-Katalinic, H. Egge, *Eur. J. Biochem.* **215**, 851 (1993).
17. S. Morath, A. Stadelmaier, A. Geyer, R. R. Schmidt, T. Hartung, *J. Exp. Med.* **195**, 1635 (2002).
18. P. Roethlisberger *et al.*, *Eur. J. Biochem.* **267**, 5520 (2000).
19. S. Morath, A. Geyer, I. Spreitzer, C. Hermann, T. Hartung, *Infect. Immun.* **70**, 938 (2002).
20. P. Roethlisberger *et al.*, *Eur. J. Biochem.* **267**, 5520 (2000).

21. A. Stadelmaier, S. Morath, T. Hartung, R. R. Schmidt, *Angew. Chem. Int. Ed.* **42**, 916 (2003).

22. N. V. Potekhina, A. S. Shashkov, L. I. Evtushenko, S. y. N. Senchenkova, I. B. Naumova, *Carbohyd. Res.* **338**, 2745 (2003).

23. B. F. Volkman *et al.*, *Biochemistry* **40**, 7964 (2001).

24. M. P. Heaton, F. C. Neuhaus, *J. Bacteriol.* **176**, 681 (1994).

25. A. Peschel, *Trends Microbiol.* **10**, 179 (2002).

26. E. Abachin *et al.*, *Mol. Microbiol.* **43**, 1 (2002).

27. I. B. Naumova *et al.*, FEMS *Microbiol. Rev.* **25**, 269 (2001).

28. R. Wodzki, *Makromol. Chem.* **194**, 2239 (1993).

29. A. C. Larsson *et al.*, *J. Am. Chem. Soc.* **127**, 2218 (2005).

30. J. R. Long, W. J. Shaw, P. S. Stayton, G. P. Drobny, *Biochemistry* **40**, 15451 (2001).

31. T. M. Alam, G. P. Drobny, *Chem. Rev.* **91**, 1545 (1991).

32. C. V. Rice, J. R. Wickham, *J. Am. Chem. Soc.* **127**, 856 (2005).

33. R. A. Fry, K. D. Kwon, S. Komarneni, J. D. Kubicki, K. T. Mueller, *Langmuir* **22**, 9281 (2006).

34. W. J. Shaw, J. R. Long, A. A. Campbell, P. S. Stayton, G. P. Drobny, *J. Am. Chem. Soc.* **122**, 7118 (2000).

35. S. Un, M. P. Klein, *J. Am. Chem. Soc.* **111**, 5119 (1989).

36. S.-J. Xiao, M. Textor, N. D. Spencer, H. Sigrist, *Langmuir* **14**, 5507 (1998).

37. D. M. Ferris *et al.*, *Biomaterials* **20**, 2323 (1999).

38. E. S. Gawalt *et al.*, *Langmuir* **19**, 200 (2003).

39. A. Rezania, R. Johnson, A. R. Lefkow, K. E. Healy, *Langmuir* **15**, 6931 (1999).

40. S. Heptinstall, A. R. Archibald, J. Baddiley, *Nature (London)* **225**, 519 (1970).

41. P. A. Lambert, I. C. Hancock, J. Baddiley, *Biochem. J.* **151**, 671 (1975).

42. T. J. Beveridge, R. G. E. Murray, *J. Bacteriol.* **141**, 876 (1980).

43. D. C. Ellwood, *Biochem. J.* **118**, 367 (1970).

44. D. C. Ellwood, D. W. Tempest, *Adv. Microb. Physiol.* **7** 83 (1972).

45. K. Wolinski, J. F. Hinton, P. Pulay, *J. Am. Chem. Soc.* **112**, 8251 (1990).

46. J. Baddiley, I. C. Hancock, P. M. A. Sherwood, *Nature (London)* **243**, 43 (1973).

47. J. Spevacek, J. Brus, *Macromol. Symp.*, 111 (2003).

48. J. Spevacek, J. Dybal, *Macromol. Rapid Commun.* **20**, 435 (1999).

49. T. M. Alam, *Int. J. Mol. Sci.* **3**, 888 (2002).

50. T. M. Alam, *Ab Initio Calculations of ^{31}P NMR Chemical Shielding Anisotropy Tensors in Phospates: The Effect of Geometry on Shielding*. J. C. Facelli, A. C. d. Dios, Eds., Modeling NMR Chemical Shifts (American Chemical Society, 1999), pp. 320-334.

Chapter 6:

Solid-state ^{31}P and ^{2}H NMR Experiments Reveal Lipoteichoic Acid as an Antifreeze Biomolecule

Introduction

Various organisms live in environments that are at subfreezing temperatures. In order for life to survive at these extreme temperatures they have to find a way to maintain liquid water. The current paradigms use thermodynamic and/or kinetic arguments for cryosurvival in mammals, plants and insects.(*1-3*) At the onset of freezing, frogs excrete large amounts of glucose to lower the freezing point of water, thus preventing the formation of large ice crystals. Fish, plants, and insects inhibit ice formation with antifreeze proteins (AFPs) that bind to the growth face of ice crystals.(*4*) Enthalpic contributions are accompanied by entropic factors from a disorganized chemical system.(*5*) These factors slow the kinetics of crystallization so that AFPs can perform their task at very low concentration, characterized as a non-colligative depression of the freezing point.

Little is known of the cryoprotection chemistry for the predominate organisms in cold environments, microbes.(*6, 7*) Some microbes maintain metabolic activity in extreme cold (below -10 °C), due to processes that have been linked to liquid water found with high salt concentrations (brine veins),

surface adsorption, or extracellular polymer substances.(*7-13*) However, these conditions are not required for bacteria to survive, as bacteria have been cultured from samples of pure ice and snow. In the laboratory, bacteria can be stored at low temperatures without the aid of cryoprotectants, although some species experience a high mortality rate. Nearly 70 years ago, Haines found that 95% of *Staphylococcus aureus* survived rapid freezing at -70 °C, showed little loss of viability after 75 days at -20 °C, and a 10x loss at -2 °C.(*14*) the greater mortality rate slightly below freezing is attributed to a denaturation of DNA, protein damage, and membrane disruption.(*15-21*) These gram-positive bacteria were more freeze resistant than gram-negative *Pseudomonas aeruginosa*, which showed 82% loss upon freezing at -70 °C, a 10x loss at -20 °C and a loss of 6 orders of magnitude at -2 °C. These experiments were carried out in the absence of cryoprotectants that are commonplace in modern microbiology studies. Phillips et al. showed that 15% glycerol, a common cryoprotectant, ensured > 80% survivability for microorganisms frozen at -70 °C for one year.(*22*) gram-positive and gram-negative bacteria were studied, which showed a 40% survival rate in distilled water.

One difference between gram-positive and gram-negative bacteria is that the former has a thick cell wall of peptidoglycan and teichoic acids. The teichoic acid molecules can extend past the cell wall where they are the first contact molecule between the cell and the growing ice crystals. It is known that non-permeable cryoprotective agents, such as polymers and polysaccharides, create a thin layer of liquid water to prevent extracellular ice from contacting the cell

surface.(*2*) The liquid water permits ion exchange and changes in hydration to reduce osmotic stress. In this chapter, we report the discovery that teichoic acid has antifreeze properties, which provide gram-positive bacteria with the capability to maintain liquid water in the peptidoglycan (cell wall) and in the immediate extracellular space. This endogenous cryoprotectant ensures liquid water to prevent cell death. This discovery opens a new paradigm in biochemistry at low temperatures.

The basis for teichoic acid antifreeze properties is most likely due to the heterogeneity of the functional groups. Teichoic acid has an anionic backbone of either glycerol-phosphate or ribitol-phosphate groups, which is decorated with hydroxyl, alanine, and *N*-acetylglucosamine groups. These groups provide teichoic acid with numerous phosphate, hydroxyl, amine, and carboxyl groups that can form hydrogen bonds, ionic interactions, and van der Waals interactions with water and/or ice crystal. Similar chemical rationales are used to explain the properties of other known cryoprotectants.

Bacteria are found in nearly all low temperature environments and must prevent ice formation to ensure survival. Microbial communities have been discovered in ice, snow, permafrost,(*23*) tundra,(*24*) and at the polar ice caps. Analysis of core samples has shown the presence of viable life hundreds of feet below the ice surface. Samples of frozen tundra have yielded various gram-positive, gram-negative, and Archaea species.(*25*) Here, gram-negative *Cryseobacterium* and gram-positive *Enterococci* were found to have a symbiotic interaction. The basis for cryosurvival is unknown, but macromolecules and/or

antifreeze proteins were suspected. Bacteria from Arctic sea ice were found in brine veins or attached to particulate surfaces.(*10*) Surface interactions favored active bacteria at -20 °C. For gram-positive bacteria, some underwent metabolism at temperature of -10 °C, while other bacteria were dormant until warmed to 37 °C. Despite the cold temperatures, cold-adapted pyschrophilic bacteria must have liquid water present at the bacterial interface to permit the exchange of nutrients and waste products.

Examination of the respective genomes have shown that, with only a few exceptions,(*7*) microbes lack the antifreeze proteins found in fish, plants, and insects. Thus, additional factors must permit liquid water at the microbe/ice interface. Liquid water can be found in brine veins of polar sea ice and at the boundaries of dust and soil particulates. However, these conditions are not a requirement for the survival of viable bacteria. It has been suggested that, in nature, cryoprotection can be provided by extracellular polymeric substances (EPS, primarily polysaccharides)(*11, 26-28*) found in the bacterial capsule and biofilm slime. However, the capsule and slime are loosely held to the bacterium and easily washed away.

Teichoic acid, a major component of the gram-positive bacterial cell wall, is a possible *in vivo* and *ex vivo* antifreeze agent. This discovery is based on ^{31}P and ^{2}H solid-state NMR data for lipoteichoic acid dissolved in D_2O, in which liquid water is shown to exist at -40 °C. Solid-state NMR is an excellent tool to distinguish between liquid and solid water. The use of deuterium oxide permits study via ^{2}H wideline NMR spectroscopy. In the absence of sample spinning, the

^{2}H quadrupole moment creates very broad lines in systems with very slow molecular motion. Molecular motion, such as reorientation in liquid water, removes quadrupolar broadening to yield very narrow lines. The sensitivity of the ^{2}H spectral lineshape to molecular motion has resulted in numerous studies on the nature of pure water, the activation energy for water motion in the ice crystal lattice, and the immobilization of water in inorganic salt crystals, soils, alumina, silicate minerals, macroporous and mesoporous materials. Other work has demonstrated the utility of ^{2}H NMR to examine phospholipid motion at water interfaces and the nature of polymer adsorbates.

Experimental

Sample preparation

Ultrapure LTA extracted from *Staphylococcus aureus* was obtained as a lyophilized powder from Invivogen, Inc. and used as received. LTA solutions were prepared by dissolving LTA in D_2O (Cambridge Isotopes) then transferred to a 5 mm zirconia rotor. The rotor was fitted with a Torlon® drive tip and air-tight Teflon® spacers sealed with O-rings. Samples of *Bacillus subtilis* cell wall (WTA and PGN, 9.7 mg) and *Staphylococcus aureus* peptidoglycan (8.2 mg) were mixed with D_2O before loading into the zirconia rotors.

WTA bound to PGN (*Bacillus subtilis*) was obtained from cells isolated from media using centrifugation at 15,000 g for 30 minutes.(*30-32*) Cells were disrupted using a French press. Repeated washing of the cells was accomplished with doubly-distilled water. The cell wall was then centrifuged at

15,000 g for an additional 20 minutes. Treatment with 3% Triton X-100 at 37 °C (30 minutes), followed by 2% SDS (37 °C, 30 minutes) were used to remove the cytoplasmic membrane. Nucleic acids were removed with trypsin (200 μg/ml) and RNase (100 μg/ml) at 37º C for 18 hours. Spectroscopic analysis (260 and 280 nm) verified removal of nucleic acids.

NMR experiments

Solid-state ^{31}P NMR experiments were performed using a 300 MHz (^{1}H) UnityInova (Varian,Inc.) NMR spectrometer (^{31}P = 121 MHz) and a 5 mm, three-channel, magic-angle-spinning NMR probe (Varian APEX design). CPMAS experiments of all samples were collected with a 1 s repetition rate, 3000 Hz spinning rate, and a contact time of 2000 μs with ^{1}H decoupling at an RF power level of 50 kHz. MAS experiments of all samples were collected with a 1 s repetition rate and 3000 Hz spinning rate. Samples were placed in a 5mm ceramic rotor with airtight top and bottom plugs. Drive and bearing gas were provided by dry compressed air. ^{31}P chemical shift data are referenced to an external standard of 85% phosphoric acid (0 ppm). Data acquisition and analysis were accomplished using VnmrJ 1.1D provided by Varian,Inc.

Solid-state ^{2}H NMR experiments were performed using a Chemagnetics NMR spectrometer (^{2}H = 46.206 MHz) and a 5 mm horizontal deuterium NMR probe (Chemagnetics design). Spectra were collected using a quadrupolar echo pulse sequence with a 1.45 μs pw90, a 40 μs τ, 128 acquisition scans, and a 10 s repetition rate. Samples were placed in a 5mm glass NMR tube (Wilmad

Glass), loaded into the probe, and frozen with the variable temperature (VT) air supply of the NMR probe. Samples were frozen for 1 hour prior to data collection.

For both ^{31}P and ^{2}H solid-state NMR experiments, variable temperature air was supplied with an FTS air drier and refrigeration unit, while probe temperature was maintained through NMR data acquisition software. A liquid nitrogen bath was used to cool the nitrogen VT gas for low temperature ^{31}P CPMAS experiments (below –50 ^{o}C).

Results and Discussion

The interactions between teichoic acids and their environment are unknown although we have observed changes to the teichoic acid structure after adsorption onto TiO_2.(*33*) The role of teichoic acid in the binding of metal ions led us to study the interactions of lipoteichoic acid with water and $MgCl_2$.(*34*) These interactions can be examined with solid-state NMR using experimental data (Δ_{CSA}, σ^{iso}, and $T_{1\rho}$) and theoretical analysis (simulated NMR spectra from energy-minimized model compounds). The presence of water requires low temperature solid-state NMR, which has been used to study the structure of amino acids(*35*) and peptides(*36-39*) in frozen aqueous glasses.

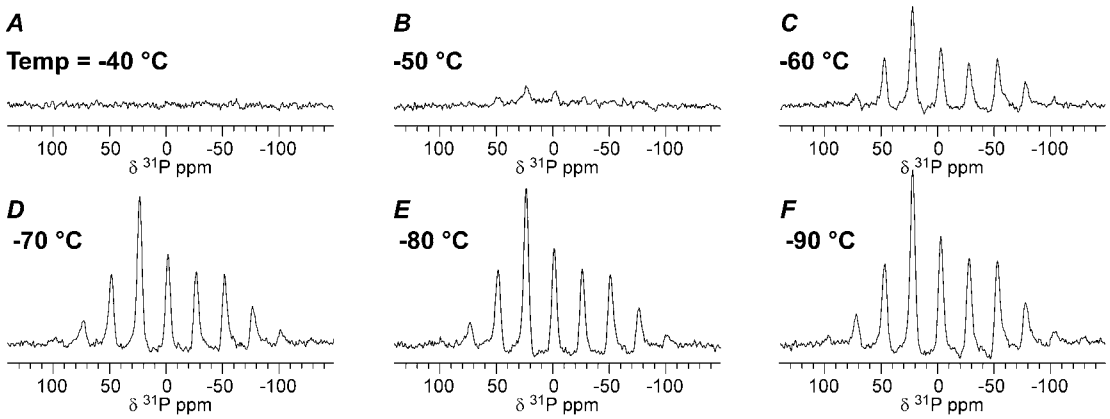

Figure 6.1. ^{31}P solid-state CPMAS spectra for lipoteichoic acid in frozen D_2O. Contact time = 2 ms, spinning rate = 3 kHz, 512 scans. The absence of a CPMAS signal at -40 °C indicates that sufficient molecular motion exists to remove the ^{1}H-^{31}P dipolar coupling that mediates cross polarization. As the temperature is lowered, the signal grows as the amount of liquid water is reduced, eventually reaching complete freezing (-70 °C) where strong CPMAS signals are observed.

^{31}P CPMAS NMR data for lipoteichoic acid in D_2O are shown in Figure 6.1. The ^{31}P CPMAS spectrum for LTA as a lyophilized powder is easily collected (Figure 5.1A in chapter 5), however frozen solutions require temperatures lower than -50 °C to see a signal. The absence of an NMR signal for temperature above -40 °C indicates that LTA has sufficient molecular motion to decouple the $^{1}H/^{31}P$ dipolar interaction that governs cross polarization. A direct polarization ^{31}P spectrum was collected at -40 °C with CW ^{1}H decoupling (data not shown). The ability to decouple the protons shows that the absence of a CPMAS signal arises from interference with cross polarization rather than T_2 relaxation during acquisition. The presence of D_2O does not affect the CPMAS experiment, as demonstrated by the ^{31}P CPMAS signal for phosphonomethylglycine frozen in D_2O at -40 °C (Figure 6.2). In fact, CPMAS in frozen aqueous solutions requires the use of D_2O as T_2 broadening is severe in

H_2O.(*35*) These data suggest that liquid water is present in teichoic acid solutions at low temperatures.

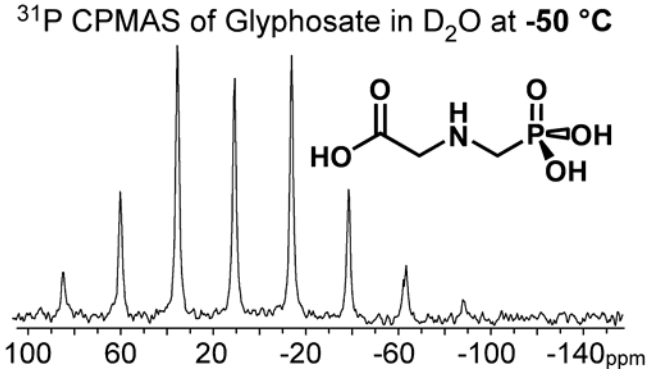

Figure 6.2. ^{31}P solid-state CPMAS spectra for glyphosate in frozen D_2O. Contact time = 2 ms, spinning rate = 3 kHz, 512 scans. The CPMAS signal indicates the ability to freeze the mixture and perform the CPMAS experiment.

The inability to collect a CPMAS NMR signal for LTA until -50 ºC suggest that there is a layer of liquid water around LTA. Deuterium wideline solid-state NMR is an excellent analytical tool for revealing the presence of liquid water. As a solid, the deuterium spectrum is dominated by a broad line, whose lineshape is used as a characteristic descriptor of molecular motion.(*40-42*) Molecular motion attenuates line broadening and changes the line shape, which can be modeled to understand the dynamics and the mode of motion. The extremes of motion for D_2O are ice, with a ^2H coupling constant of 140 kHz, and liquid water, with a coupling constant 1-2 kHz. The ^2H spectrum for water at room temperature is shown in Figure 6.3A. The narrow line (1.3 kHz) is a distinguishing feature of liquid water, which changes to the characteristic spectrum of frozen water at -25 °C (Figure 6.3B). When LTA is dissolved in D_2O at a concentration of 55 mg/ml, the ^2H spectrum shows the liquid water peak at room temperature (not shown).

Upon cooling to -25 °C, the spectrum becomes a mixture of broad and narrow components (Figure 6.3C). At -40 °C, the amount of the broad component increases and the narrow peak decreases, but is still detectable without the aid of deconvolution (Figure 6.3D). We assign the narrow peak to liquid water around LTA, as the line-width is smaller than the reported line-widths for the reorientation of water molecules.

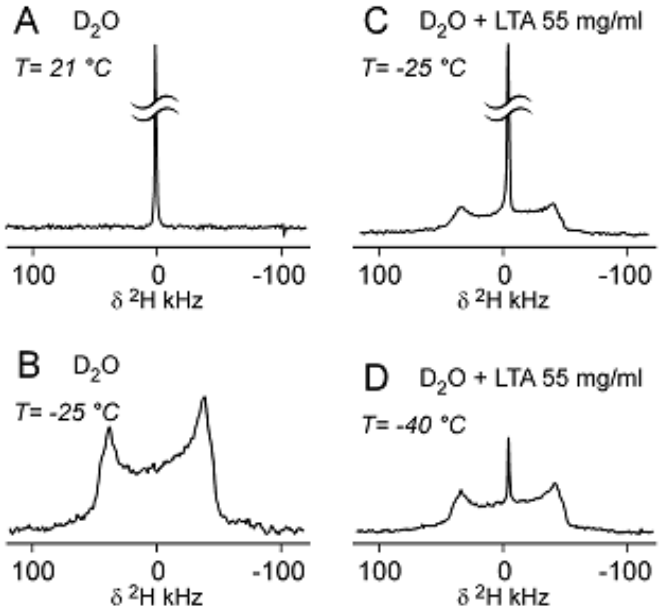

Figure 6.3. ^{2}H wideline solid-state NMR spectra of D_2O and LTA dissolved in D_2O. At room temperature, the ^{2}H spectrum reveals a narrow line for liquid water (A) whereas a broad line for frozen water is seen at -25 °C (B). When lipoteichoic acid is dissolved in D_2O, the low temperature ^{2}H spectrum at -25 °C shows both liquid water and ice (C). This clearly demonstrates the antifreeze properties of lipoteichoic acid. When the sample is cooled to -40 °C, the amount of liquid water is reduced with a corresponding increase in ice concentration (D). Spectra were collected using a quadrupolar echo pulse sequence with a 1.45 μs pw90, a 40 μs τ refocusing period, 128 acquisition scans, and a 10 s repetition rate.

Within a few degrees of the D_2O melting point (3.8 °C), water molecules flip between ice crystal sites yielding a narrow isotropic peak. Pines et al. used

variable temperature ^{1}H and ^{2}H NMR studies to examine the molecular dynamics of ice.(*43*) In the hexagonal form of ice, I_h, the central water molecule is bound to 2 neighboring H atoms via the oxygen and 2 neighboring oxygen atoms via the protons. These four bonds form a tetrahedron around the central water molecule. A narrow line is seen at -6 °C and attributed to isotropic reorientation within the ice lattice. At -24 °C, the narrow line is less intense due to a reduction in dynamics. In the LTA/D_2O data collected at -25 °C, the narrow peak is very strong and more intense than the water/ice spectra (-24 °C) reported by Pines et al. A mixture of mobile and solid water has been reported for hydrated minerals. At room temperature, the sodium-silicate Kanemite has 3 bound water molecules which move between tetrahedral binding sites within the mineral structure.(*44*) These dynamics are similar to those of frozen water, where reorientation occurs within the tetrahedral ice structure, yet the line-width is larger than that of our water sample. In addition, mesoporous materials also contain structured water. Water bound to the surface of aluminophosphate ($AlPO_4$-5) molecular sieves undergoes exchange with free water, yet the line-width is still 11 kHz.(*45*) Another aluminophosphate (VPI-5) has larger channels and faster exchange between bound and free water, and results in the line-width being reduced to 6 kHz. These water ^{2}H signals are much broader than that of liquid water and the liquid water ^{2}H signal of Figure 6.3C (1.3 kHz).

Lipids are present and it is possible that micelles form to impart the antifreeze properties via the lipid tails. Liquid water has been detected in phospholipid bilayers, although this water remains bound to the headgroups.

The ^{2}H NMR lineshape was dependent on temperature and the number of bound water molecules.(*46*) A DMPC bilayer bound water to the headgroup in addition to water in a clathrate structure around the headgroup. Additional data was collected with ^{2}H labels in lipids with methylene and trimethylammonium headgroups.(*47*) The resulting linewidth, lineshape, T_1 and T_2 relaxation rates verified that lipid dynamics was facilitated by the presence of liquid water. Yoon et al. showed that the addition of cryoprotectants reduced the lateral pressure in the phosphatidylcholine lamellae.(*48*) Reducing the mechanical stress aids in cryopreservation of intact membranes important for gram-negative bacteria. However, the role of micelle formation is subordinate to the hydrophilic teichoic acid groups. The lipids only contribute 10% of the mass to LTA with 40 - 50 phosphodiester repeat units. Nevertheless, liquid water must also be present around the teichoic acid phosphate groups as ^{31}P CPMAS experiments are not possible.

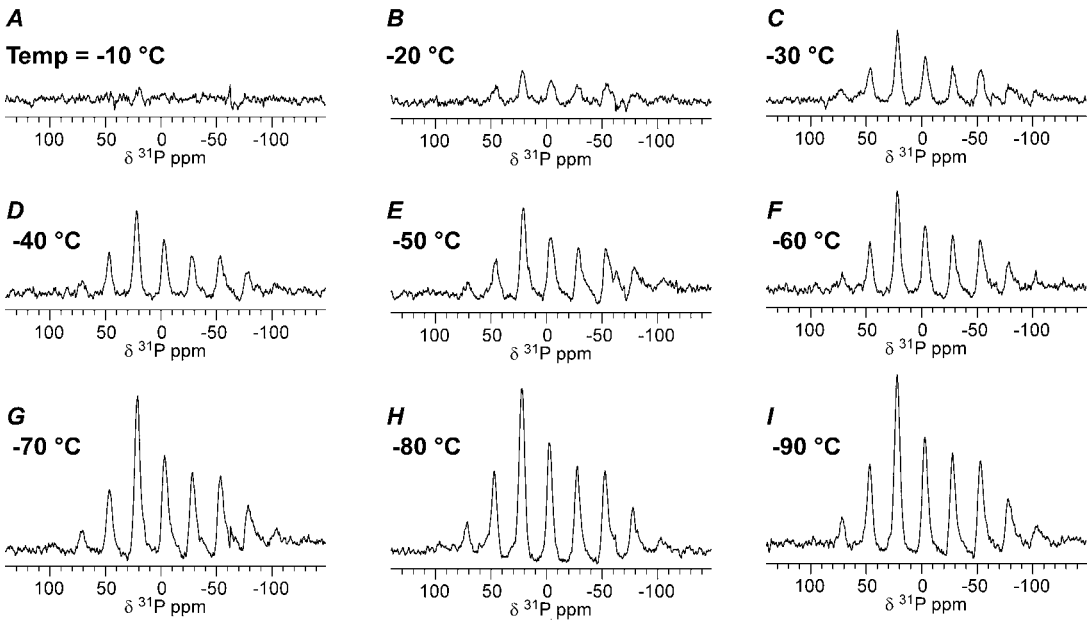

Figure 6.4. ^{31}P solid-state CPMAS spectra for wall teichoic acid, in peptidoglycan complex (cell wall), frozen in D_2O. Contact time = 2 ms, spinning rate = 3 kHz, 512 scans. Strong CPMAS signals are not seen until -30 °C. Thus, even in the cell wall, teichoic acid has antifreeze properties. The signals increase at -70 °C, which is interpreted as teichoic acid extending past the cell wall where its antifreeze behavior is similar to that of purified LTA.

Gram-positive bacteria also have teichoic acid bound to peptidoglycan (PGN) of the cell wall. $T_{1\rho}$ relaxation rate data show that teichoic acid interacts strongly with the PGN in the cell wall (table 1 in chapter 5). We speculate that WTA/PGN interactions may quench molecular motion and may interfere with antifreeze behavior in solution, which is verified by the absence of a ^{31}P CPMAS signal until -30 °C, rather than -60 °C with pure LTA. The ^{31}P CPMAS temperature array data for wall teichoic acid is shown in Figure 6.4. As with LTA, signals are not observed until temperatures significantly below freezing. Compared with the -90 °C spectrum (Figure 6.4I), about half of the teichoic acid phosphate groups are seen from -30 to -60 °C. We suspect that these phosphate groups are from teichoic acid within the cell wall framework where

their molecular motion is hindered by interactions with the surrounding peptidoglycan. These interactions permit freezing at a temperature higher than that of pure LTA. However, the WTA/PGN interaction is not strong enough to immobilize the teichoic acid from 0 to -20 °C as demonstrated by the weak (or absent) ^{31}P CPMAS signal. Thus, even within the peptidoglycan cell wall, teichoic acid is able to function as an antifreeze agent. This behavior is critical for nutrient exchange and the reduction of osmotic stress within the cell wall. The ^{31}P CPMAS signal increases below -60 °C and remains constant. These phosphate groups likely originate form teichoic acid outside of the cell wall, where their antifreeze properties would resemble that of lipoteichoic acid (Figure 6.1).

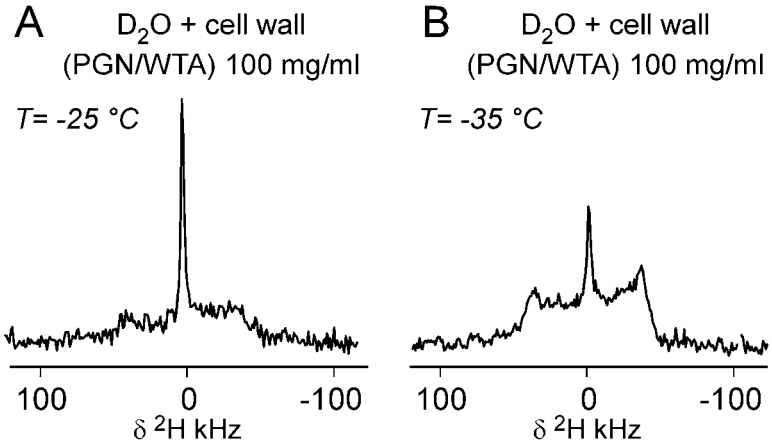

Figure 6.5. ^{2}H wideline solid-state NMR spectra of wall teichoic acid, in the peptidoglycan complex (cell wall), frozen in D_2O. Using samples of *B. subtilis* cell wall (WTA bound to PGN), the ^{2}H wideline solid-state NMR spectrum (A) shows the presence of liquid water at -25 °C, The signal-to-noise ratio is smaller than that of Figure 6.3 due the smaller sample size. As with purified LTA, cooling reduces the amount of liquid water and increases ice formation (B). Spectra were collected using a quadrupolar echo pulse sequence with a 1.45 μs pw90, a 40 μs τ refocusing period, 128 acquisition scans, and a 10 s repetition rate.

As before, ^{2}H wideline NMR spectroscopy verifies the presence of liquid water within the WTA/PGN sample (Figure 6.5). At -25 °C, a strong liquid water signal is seen with little ice formation. Cooling to -35 °C shows increased formation of ice. Compared with the data in Figure 6.3, the overall signal-to-noise ratio is lower due to the smaller size of the WTA/PGN/D_2O sample. To demonstrate that teichoic acid is responsible for antifreeze properties in the bacterial cell wall, we examined the antifreeze properties of cell wall peptidoglycan (*S. aureus*) without teichoic acid present. A ^{31}P CPMAS and MAS study confirms the absence of phosphate groups (not shown). When frozen in D_2O, the ^{2}H wideline spectrum at -25 °C does show some liquid water (Figure 6.6). The water signal is much smaller than that of pure LTA or WTA/PGN at the same temperature, and the small liquid D_2O peak decreases at -35 °C. These data are a clear indication that the repeating units of N-acetylglucosamine (GlcNAc), N-acetylmuramic acid (MurNAc), and the peptide cross-links do not impart dramatic antifreeze properties on the cell wall. Thus, the presence of teichoic acid is critical to prevent ice formation in and around the cell wall. The peptidoglycan cell wall of *S. aureus* and *B. subtilis* are identical and thus comparison between the purified cell wall and WTA/PGN samples is valid. As antifreeze properties are seen for teichoic acid originating from different species, our data suggest that other gram-positive bacteria may also benefit form cryoprotection through teichoic acids.

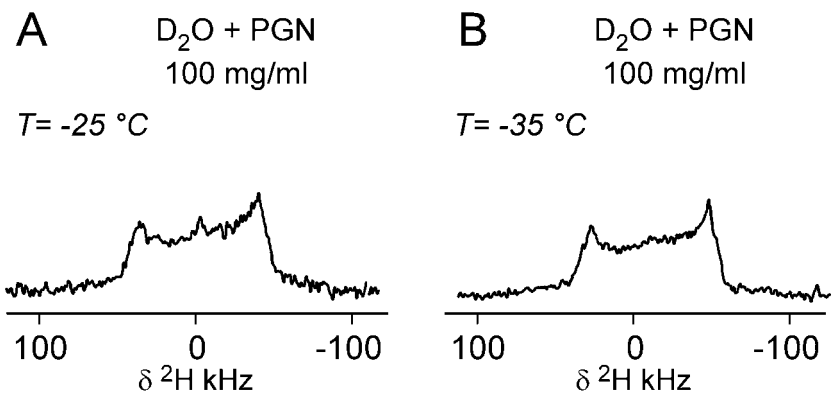

Figure 6.6. ^{2}H wideline solid-state NMR spectrum of *S. aureus* cell wall frozen in D_2O. This spectrum demonstrates that the cell wall of *S. aureus* does not show strong antifreeze characteristics. Spectra were collected using a quadrupolar echo pulse sequence with a 1.45 μs pw90, a 40 μs τ refocusing period, 128 acquisition scans, and a 10 s repetition rate.

Antifreeze proteins are found in two distinct chemical categories.(*1*) For AFP Types I, II, and III, the 37-66 residues contain large fractions of alanine residues. The α-helix secondary structure is ampiphilic with nonpolar alanines segregated from other polar residues, mainly threonine, asparginine and aspartate.(*5*) Alternatively, antifreeze glycoproteins (AFGPs) contain alanine with the disaccharide 3-*O*-(β-D-galactosyl)-D-*N*-acetylgalactosamine) extending from threonine residues. The antifreeze mechanism involves binding to ice crystals, hydrogen bonding, and van der Waals interactions.(*49, 50*) Not only do the disaccharide units provide additional opportunities for hydrogen bonding, but the sugars also disrupt the helical structure. The resulting disordered structure aids the antifreeze mechanism through entropic factors.

The chemical composition of teichoic acid is similar to known antifreeze agents of glycerols, AFPs, AFGPs, and saccharides. LTA and WTA contain glycerol (or ribitol), alanine branches, and N-acetylglucosamine branches, in

addition to phosphate groups. The branches are distributed in a random order; however, the alanine of TA is connected to the glycerol (or ribitol) backbone through the carboxyl group, leaving the non-polar methyl group and ionic amine exposed to solution. This is a very different chemical arrangement from Ala in the AFP backbone. Studies to elucidate the structural role of the alanine are underway, but it has been postulated that the cationic Ala-NH_3^+ forms an intramolecular ion pair with the anionic phosphate group.(*34*) Such a configuration would leave the N-acetylglucosamine groups available for hydrogen bonding with liquid water, or with the surface of an ice crystal. Carbon-13 CPMAS studies of AFPs verify ice crystal binding.(*49*) These studies were performed from -10 to -50 °C, where complete freezing must take place for the CPMAS experiment to succeed. AGFPs can also be studied with CPMAS at -20 °C,(*51*) where conformational states begin to "freeze" out of the D_2O solution.(*52*) Conformational changes occur as the temperature is lowered to -80 °C. Unlike AFPs, our data shows water/ice mixtures at -40 °C. The ^{31}P CPMAS spectra show that ice binding, if it occurs, is not strong enough to hinder lipoteichoic acid molecular motion, at least until -60 °C.

The peptidoglycan serves as a structural feature that provides a more robust cell envelope for gram-positive bacteria rather than the weak envelope of lipid bilayers for gram-negative bacteria. This may help explain the high cryosurvival rate for gram-positive bacteria. Without teichoic acids, the formation of ice within the cell wall would cause a volume expansion and may compromise the structural integrity of the peptidoglycan. Additional insight regarding the role

of teichoic acids in cryo-biochemistry could be obtained using mutants with teichoic acid deletions. These strains should exhibit increased freeze mortality. However, to our knowledge complete deletion of LTA has not been achieved limiting the amount of biological studies that can be preformed.

Conclusions

Many studies have used genetic mapping to determine if an organism has antifreeze proteins.(*9*) These studies show that only a few gram-positive bacteria have the genetic makeup to express antifreeze proteins. Gram-positive bacteria can use salts, nucleic acids and lipids as antifreeze agents in the cytoplasm and membrane bilayer. As teichoic acid is ubiquitous in Gram-positive bacteria, teichoic acid can be used to ensure survival of individual bacteria and biofilm communities. In the latter, teichoic acids are excreted and could have a symbiotic role as antifreeze agents.

References

1. Y. Yeh, R. E. Feeney, *Chem. Rev.* **96**, 601 (1996).
2. Z. Hubalek, *Cryobiology* **46**, 205 (2003).
3. P. B. Price, *FEMS Microbiol. Ecol.* **59**, 217 (2007).
4. B. Moffatt, V. Ewart, A. Eastman, *Physiol. Plant.* **126**, 5 (2006).
5. H. M. Chao *et al.*, *Biochemistry* **36**, 14652 (1997).
6. G. Feller, C. Gerday, *Nat. Rev. Microbiol.* **1**, 200 (2003).
7. S. L. Wilson, D. L. Kelley, V. K. Walker, *Environ. Microbiol.* **8**, 1816 (2006).
8. P. B. Price, T. Sowers, *Proc. Natl. Acad. Sci. U.S.A.* **101**, 4631 (2004).
9. S. D'Amico, T. Collins, J. C. Marx, G. Feller, C. Gerday, *EMBO Rep.* **7**, 385 (2006).
10. K. Junge, H. Eicken, J. W. Deming, *Appl. Environ. Microbiol.* **70**, 550 (2004).
11. K. Junge, H. Eicken, B. D. Swanson, J. W. Deming, *Cryobiology* **52**, 417 (2006).
12. T. Mock, D. N. Thomas, *Environ. Microbiol.* **7**, 605 (2005).
13. J. A. Gilbert, P. J. Hill, C. E. R. Dodd, J. Laybourn-Parry, *Microbiology* **150**, 171 (2004).
14. R. B. Haines, *Proc. R. Soc. B* **124**, 451 (1938).
15. M. D. Alur, N. Grecz, *Biochem. Biophys. Res. Comm.* **62**, 308 (1975).
16. P. H. Calcott, S. K. Lee, R. A. Macleod, *Can. J. Microbiol.* **22**, 106 (1976).
17. P. H. Calcott, R. A. Macleod, *Can. J. Microbiol.* **20**, 671 (1974).
18. P. H. Calcott, R. A. Macleod, *Can. J. Microbiol.* **20**, 683 (1974).
19. P. H. Calcott, R. A. Macleod, *Can. J. Microbiol.* **21**, 1960 (1975).

20. P. H. Calcott, R. A. Macleod, *Can. J. Microbiol.* **21**, 1724 (1975).

21. J. M. Panoff, B. Thammavongs, M. Gueguen, P. Boutibonnes, *Cryobiology* **36**, 75 (1998).

22. H. A. Ludlam, B. Nwachukwu, W. C. Noble, A. V. Swan, I. Phillips, *J. Appl. Bacteriol.* **67**, 417 (1989).

23. B. Steven *et al.*, *FEMS Microbiol. Ecol.* **59**, 513 (2007).

24. M. D. Wallenstein, S. McMahon, J. Schimel, *FEMS Microbiol. Ecol.* **59**, 428 (2007).

25. V. K. Walker, G. R. Palmer, G. Voordouw, *Appl. Environ. Microbiol.* **72**, 1784 (2006).

26. C. Krembs, A. Engel, *Mar. Biol.* **138**, 173 (2001).

27. J. A. Raymond, C. H. Fritsen, *Cryobiology* **43**, 63 (2001).

28. C. Krembs, H. Eicken, K. Junge, J. W. Deming, *Deep-Sea Res. Pt I* **49**, 2163 (2002).

29. J. W. Deming, *Curr. Opin. Microbiol.* **5**, 301 (2002).

30. A. Umeda, S. Yokoyama, T. Arizono, K. Amako, *J. Electron Microsc.* **41**, 46 (1992).

31. K. Amako, A. Umeda, K. Murata, *J. Bacteriol.* **150**, 844 (1982).

32. A. Umeda, Y. Ueki, K. Amako, *J. Bacteriol.* **169**, 2482 (1987).

33. C. V. Rice, J. R. Wickham, *J. Am. Chem. Soc.* **127**, 856 (2005).

34. F. Neuhaus, J. Baddiley, *Microbiol. Mol. Biol. Rev.* **67**, 686 (2003).

35. L. J. Smith, F. P. Boulineau, D. Raftery, A. Wei, *J. Am. Chem. Soc.* **125**, 14958 (2003).

36. M. S. Pometun, U. M. Gundusharma, J. F. Richardson, R. J. Wittebort, *J. Am. Chem. Soc.* **124**, 2345 (2002).

37. H. W. Long, R. Tycko, *J. Am. Chem. Soc.* **120**, 7039 (1998).

38. J. M. Gibson, J. M. Popham, V. Raghunathan, P. S. Stayton, G. P. Drobny, *J. Am. Chem. Soc.* **128**, 5364 (2006).

39. J. J. Balbach *et al.*, *J. Biomol. NMR* **16**, 313 (2000).

40. M. Duer, *Annual Reports on NMR Spectroscopy* **43**, 1 (2001).

41. M. J. Duer, Ed., *Solid-State NMR Spectroscopy: Principles and Applications* (Blackwell Science, Ltd, Oxford, UK, 2002), pp.

42. K. Schmidt-Rohr, H. W. Spiess, *Multidimensional Solid-State NMR and Polymers* (Academic Press, New York, 1994)

43. R. J. Wittebort, M. G. Usha, D. J. Ruben, D. E. Wemmer, A. Pines, *J. Am. Chem. Soc.* **110**, 5668 (1988).

44. A. J. Benesi, M. W. Grutzeck, B. O'Hare, J. W. Phair, *Langmuir* **21**, 527 (2005).

45. D. Goldfarb, H. X. Li, M. E. Davis, *J. Am. Chem. Soc.* **114**, 3690 (1992).

46. C. H. Hsieh, W. G. Wu, *Biophys. J.* **71**, 3278 (1996).

47. W. G. Wu, L. M. Chi, T. S. Yang, S. Y. Fang, *J. Biol. Chem.* **266**, 13602 (1991).

48. Y. H. Yoon, J. M. Pope, J. Wolfe, *Biophys. J* **74**, 1949 (1998).

49. Y. G. Mao, Y. Ba, *Biophys. J* **91**, 1059 (2006).

50. A. J. Scotter *et al.*, *Cryobiology* **53**, 229 (2006).

51. V. V. Krishnan *et al.*, *J.Chem. Phys.* **123** (2005).

52. N. M. Tsvetkova *et al.*, *Biophys. J* **82**, 464 (2002).

Appendix A

Publications

"Heterogeneous Binding of Lipoteichoic Acid to the Surface of Titanium Dioxide as Determined with 31P Solid-State NMR Spectroscopy." Rice, Charles V.; Wickham, Jason R. Journal of the American Chemical Society (2005), 127(3), 856-857.

"Lithium Environment in Dilute Poly(ethylene oxide)/Lithium Triflate Polymer Electrolyte from REDOR NMR Spectroscopy." Wickham, Jason R.; York, Shawna S.; Rocher, Nathalie M.; Rice, Charles V. Journal of Physical Chemistry B (2006), 110(10), 4538-4541.

"Solid-state NMR Studies of the Crystalline and Amorphous Domains Within PEO and PEO: LiTf Systems." Wickham, Jason R.; Mason, Rachel N.; Rice, Charles V.. Solid State Nuclear Magnetic Resonance (2007), 31(4), 184-192